ABSTRACT

Title of dissertation: SOFT ROBOTIC APPENDAGES USING PNEUMATIC ARTIFICIAL MUSCLES

Thomas E. Pillsbury
Doctor of Philosophy, 2018

Dissertation directed by: Professor Norman M. Wereley
Department of Aerospace Engineering

This dissertation focuses on advancing the state of the art in soft robotics using pneumatic artificial (PAM) actuators. Pneumatic artificial muscles are currently used in robotic and prosthetic applications due to their high power to weight ratio, controllable compliance, and simple design. Contractile PAMs are typically used in traditional hard robotics in place of heavy electric motors. As the field of soft robotics grows, extensile PAMs are beginning to have increased usage. The bladder of a PAM affects common actuator performance metrics, specifically: blocked force, free contraction, hysteresis, and dead-band pressure. This work investigates the effect that bladder thickness has on static actuation performance of small scale PAMs. Miniature PAMs were fabricated with a range of bladder thicknesses then experimentally characterized in quasi-static conditions, where results showed that increasing bladder wall thickness decreases blocked force and free contraction, while the dead-band pressure increases. A nonlinear model was then applied to determine the structure of the stress-strain relationship that enables accurate modeling and the minimum

number of terms. Contractile and extensile PAMs were experimentally fabricated and parametrically compared to demonstrate the advantages and disadvantages of each type of PAM and applications for which they are best suited. An additional PAM model was developed based on finite strain theory to address the lack of predictive models. The closed-form pneumatic artificial muscle quasi-static actuator force is obtained. The analysis was experimentally validated using actuation force versus contraction ratio test data at a series of discrete inflation pressures for four different pneumatic artificial muscles, two contractile and two extensile. This work investigates adding bio-inspired ossicle structures from brittle stars to pneumatic artificial muscle continuum arm sections. The ossicle structure increases the range of motion and load capability of the continuum arm section while reducing the pneumatic pressure requirements. In this work, a static model of the continuum arm section is developed assuming constant curvature in the section and finding the center of mass of the section and its end plate. This model is validated by comparing the pressure-angle relationship at various loading conditions.

SOFT ROBOTIC APPENDAGES USING PNEUMATIC ARTIFICIAL MUSCLES

by

Thomas Edward Pillsbury

Dissertation submitted to the Faculty of the Graduate School of the
University of Maryland, College Park in partial fulfillment
of the requirements for the degree of
Doctor of Philosophy
2018

Advisory Committee:
Professor Norman M. Wereley, Chair/Advisor
Dr. Craig Carignan
Professor Ross Miller
Professor Derek Paley
Professor Robert Sanner
Professor Elisabeth Smela

Acknowledgments

I would like to acknowledge the support of my advisor, Dr. Norman Wereley. Dr. Wereley has been my advisor for seven years starting with my undergraduate Aerospace Honors Research project.

I would also like to thank Dr. Carignan, Dr. Miller, Dr. Paley, Dr. Sanner, and Dr. Smela for their support as my doctoral committee members.

I must thank Ben Woods and Robbie Vocke for their patient guidance as I worked on morphing skin concepts as an undergraduate in the lab.

Kevin, thank you for fixing my computer problems so quickly between the week before my defense.

I would like to acknowledge the external funding that supported the majority of my graduate work. First I received the National Science Foundation Graduate Research Fellowship DGE 1322106. I was also supported as part of the Office of Naval Research Basic Research Challenge: SEASTAR project and the UMD Ann G. Wylie Dissertation Fellowship.

To everyone else in the lab, thanks for keeping me sane over the years. Special thanks to Jon, Steve, Andrew, Ryan, Sylvie, Gary, Caitlin, and Rebecca. Thanks to Dave and Andrew for motivating me to get to the gym on a consistent basis, at least for a while.

I would also like to acknowledge my family and friends. Dad, Mom, and Tim thank you for your support. Uncle Mike I appreciate the interest that you have shown in my work.

Molly, I couldn't have done this without you. I can't wait to start the next chapter of our life together.

Table of Contents

List of Tables

List of Figures

List of Abbreviations

DOF	Degrees of freedom
PAM	Pneumatic artificial muscle
$(A\Phi Z)$	Cylindrical coordinates defining PAM geometry
$(a\phi z)$	Cylindrical coordinates defining deformed PAM geometry
B	Length of a single fiber of the braid
C	Cauchy-Green Tensor
C_D	Damping matrix of the continuum arm
C_{01}, C_{10}	Mooney-Rivlin constants
D	Outer diameter of a PAM
D	Initial outer diameter of a PAM
E_i	"Modulus" of PAM bladder for strain of power i
E_{i_I}	Intercept of the "modulus" of PAM bladder for strain of power i with respect to PAM pressure
E_{i_S}	Slope of the "modulus" of PAM bladder for strain of power i with respect to PAM pressure
F	Force of a PAM
F_a, F_ϕ	Forces in the PAM bladder from Mooney-Rivlin derived stresses
F_D	Deformation gradient of the PAM
F_{B_k}	Predicted blocked force at the k^{th} test pressure
$F_k i$	Model force of a PAM at the k^{th} test pressure and $i^t h$ stroke at the pressure
$F_{AVG_k i}$	Average experimental force of a PAM at the $k^t h$ experimental pressure and $i^t h$ stroke at the pressure
$F_{\Delta L = x * F_C}$	Predicted force at a give contraction
$(F_{\Delta L = x * F_C})_{meas}$	Average experimental force at the given contraction
g	Acceleration due to gravity
G	Vector of force required in the PAMs due to potential energy, specifically gravity in this work
h_i	Length of the i^{th} bending section of a continuum arm assuming constant curvature
h_{i0}	Initial length of the i^{th} bending section of a continuum arm assuming constant curvature
H_{load}	Work of the PAM loading curve
H_{unload}	Work of the PAM unloading curve
$H_{\beta_{1_j}}$	Partial derivative of J_{β_i} with respect to the j^{th} PAM length
I_1, I_2, I_3	Strain invariants
J_{β_i}	Jacobian matrix relating the PAM velocities to the velocity of the center of mass of the i^{th} bending section
J_{M_i}	Jacobian matrix relating the PAM velocities to the velocity of the center of mass of the i^{th} section divider
l_{ij}	j^{th} PAM in the i^{th} bending section of a continuum arm

L	Length of the PAM
L_0	Initial length of the PAM
m_i	Mass of the i^{th} bending section of a continuum arm
M	Mass matrix of the continuum arm
M_i	Mass of the i^{th} section divider of a continuum arm
N	Number of turns the a single fiber of the braid makes about the diameter of the PAM
N_P	Number of PAM pressures experimentally tested and used to fit the bladder stresses
N_i	Number of force-stroke values modeled for the PAM pressure tested
p_s	Hydrostatic pressure in the PAM bladder
p_{CC_i}	Position assuming constant curvature in the i^{th} bending section of a continuum arm with respect to the beginning of that bending section
p_i	Position of the end of the end of the i^{th} section divider of a continuum arm with respect to base of the arm
p_{β_i}	Position of the center of gravity of the i^{th} bending section of a continuum arm with respect to the base of the arm
p_{M_i}	Position of the center of gravity of the i^{th} section divider of a continuum arm with respect to the base of the arm
$p_{M_{lcl_i}}$	Position of the end of the i^{th} section divider of a continuum arm with respect to the end of the i^{th} bending section
$\dot{p}_{\beta_i}$	Velocity of the center of gravity of i^{th} bending section of a continuum arm with respect to the base of the arm
$\dot{p}_{M_i}$	Velocity of the center of gravity of the i^{th} section divider of a continuum arm with respect to the base of the arm
P	Pressure applied to a PAM
P_0	Atmospheric pressure
P'	Corrected PAM pressure after accounting for dead-band pressure
P_{DB}	Dead-band pressure, pressure required to overcome the initial elasticity of the PAM bladder
r	Inner radius of a PAM
r	Initial inner radius of a PAM
r_i	Radius the PAM are attached at for the i^{th} bending section of a continuum arm
R	Outer radius of a PAM
R_0	Initial outer radius of a PAM
R_{CC_i}	Rotation matrix assuming constant curvature defining the orientation of the i^{th} bending section of a continuum arm
s	Distance along the i^{th} bending section of a continuum arm
t	Bladder wall thickness of a PAM
t_0	Initial bladder wall thickness of a PAM
T	Tension in the PAM braid
T_E	Kinetic energy of the continuum arm
V	Cylindrical volume enclosed of a PAM of diameter D

V_B	Volume of the bladder material of a PAM
V_{int}	Internal volume of the PAM
V_E	Potential energy of the continuum arm
W	Strain density function
W_{out}	Work of a PAM force-stroke curve for a constant pressure
β_i	Position of the center of gravity of the i^{th} bending section of a continuum arm with respect to the base of the bending section
Δ	Average force error at each pressure
Δ_{FB}	Average blocked force error of the PAM force model across all pressures
Δ_{FC}	Average free contraction error of the PAM force model across all pressures
Δ_{IC}	Average force error of the PAM force model at a given contraction level across all pressures
ΔL	Change in PAM length
ΔP	Change in PAM pressure
ΔV	Change in PAM volume
$\Delta L_{F=0_k}$	Predicted free contraction from the model at the k^{th} test pressure
ϵ	Strain in the PAM bladder
ϵ_c	Circumferential strain in the PAM bladder
ϵ_z	Axial strain in the PAM bladder
η	Hysteresis of a PAM force-stroke curve
η_c	Efficiency of a PAM force-stroke curve for a constant pressure
Γ_{ijk}	Christoffel symbols for calculation of the damping matrix
λ	Axial stretch ratio of a PAM
λ_a	Principal stretch in the a-direction
λ_ϕ	Principal stretch in the ϕ-direction
λ_z	Principal stretch in the z-direction
ϕ_i	Bending plane of the i^{th} bending section of a continuum arm assuming constant curvature
ϕ_{ij}	Angle of the attachment of the PAM with respect to the chosen $\phi_i = 0$
σ_c	Circumferential stress in the PAM bladder
$\sigma_a, \sigma_z, \sigma_\phi$	Stress in the PAM bladder
θ	Angle the braid of a PAM makes with respect to a line perpendicular to the length of the PAM
θ_0	Initial angle the braid of a PAM makes with respect to a line perpendicular to the length of the PAM
θ_i	Bending angle of the i^{th} bending section of a continuum arm assuming constant curvature

Chapter 1: Introduction

In this chapter, pneumatic artificial muscles are introduced for soft robots. Hyper-redundant and continuum robotic literature is introduced specifically medically devices and soft robots, and the modeling techniques that have been used to analyze these structures are detailed. Pneumatic artificial muscle development is explored to address how these actuators have previously been used modeled and used in soft robots and address the gaps in knowledge when using pneumatic artificial muscles in these devices. The goal of this research is to develop small-scale soft robotic manipulators built with pneumatic artificial muscles which increase load capability without sacrificing flexibility.

1.1 Problem Statement

Robotics to-date have been successful in highly structured environments such as industrial applications. There have been research efforts to increase allowable interaction with the robotic manipulator during operation by introducing compliant structures and actuation systems. These compliant mechanisms allow for some interaction, but there is a need to design robots to be used in unstructured dynamically varying environments. Hyper-redundant robots have been used to approach this goal

with traditional rigid robotics, but require a large number of joints and associated actuation elements increasing overall system weight. Continuum robots are an extension of hyper-redundant robots which possess a large number of degrees of freedom, but lack traditional rotary or prismatic joints. Continuum robots help solve the problems associated with the increased weight of a large number of actuators and joints, but are generally still constructed of metals and other hard materials.

Soft robotic manipulators attempt to overcome the drawbacks associated with an increased number of actuators and system weight by introducing increasingly flexible bodies and actuators to the manipulator. These lightweight bodies deform to interact with unstructured environments for tasks such as unplanned grasping of objects in unexpected orientations. In soft robotics, there are a number of inspirational biological examples ranging from terrestrial animals such as an elephant's trunk to aquatic animals such as sea-stars and octopuses. In potential aquatic and space applications, there is a reduced impact of self weight on the performance of the manipulator. To build a robot with a soft body requires a light-weight, soft actuator such as pneumatic artificial muscles.

Pneumatic artificial muscles (PAMs) will be investigated in this dissertation for use in soft robots and continuum manipulators. To investigate PAMs, this research will specifically study miniaturization and performance metrics of PAMs. The miniaturization and metrics will be used to compare extensile and contractile PAMs for use in a soft robotic manipulator. After comparing the two types of PAMs, one will be chosen and applied to a bio-inspired continuum manipulator to achieve high force to compliance. Reduced order modeling of the manipulator

will be formulated and quasi-statically validated with experiments on the fabricated manipulator.

The purpose of the research is to investigate the use of PAMs as actuators in robotic manipulators, specifically bio-inspired continuum manipulators. The major goals are to precisely model both contractile and extensile PAM behavior, and validate models of the continuum systems employing these actuators. More broadly, this dissertation aims to complement and improve upon the existing knowledge of PAM-based continuum robotics.

1.2 Continuum Robotics

Continuum robots are robots that have a high to near infinite number of degrees of freedom to work in cluttered environments where obstacle avoidance is necessary, and are extensions of hyper-redundant or "serpentine" robots [1]. One of the first hyper-redundant manipulators dates to the 1960s with the Tensor Arm of Anderson and Horn [2]. These manipulators are referred to as "serpentine" due to their ability to snake through pipes [3]. Larson and Davidson patented a flexible robot arm formed with a combination of cables, hydraulic, and pneumatic elements actuating a spinal-like structure to improve flexibility of industrial manipulators [4]. A number of trunk-like manipulators have been described in the literature with some attached to a robotic base [5] and others designed for congested environments like chemical plants [6]. Hyper-redundant medical devices have also been designed with similar functionality to continuum medical device such as a tendon actuated

hyper-redundant arthroscope steerable tip [7]. Wilson *et al.* studied the important biological features of elephant trunks and squid tentacles and incorporated them into pneumatic bellows manipulators and gripper for pick and place experiments [8].

Continuum robots are robots that do not contain rigid links and identifiable rotation joints. Depending on the actuation mechanism these robots have been grouped as intrinsic, extrinsic, or hybrid [9]. Intrinsically actuated continuum robots have actuators located as part of the section that is deforming, while extrinsic actuation occurs remotely, and hybrid actuation schemes employ some combination of intrinsic and extrinsic actuation. Continuum robot structure can vary from a metal backbone extrinsically actuated to produce motion to a soft manipulator consisting of an actuator which provides both the structure and actuation.

An example of the latter, Suzumori *et al.* designed a three chamber three degree of freedom pneumatic (or hydraulic) reinforced rubber actuators and applied this actuator both in serial and parallel arrangements [10]. The two section serial arrangement is an early soft robotic manipulator and the parallel mechanism is an early soft gripper. Another early soft robot developed was a hybrid continuum manipulator comprised of pneumatic bellows to control the length of the arm which was bent by tendons actuated at the base [11]. This arm, seen in Fig. 1.1, was used for vacuuming during nuclear decontamination and proposed for other applications including spray washing, materials handling, and robotic refueling.

An overview of hyper-redundant and continuum robots can be found in Webster and Jones' review of constant curvature robots [12]. Table 1 in that work, replicated in Fig. 1.2, provides a sample of the range of applications and design of both types

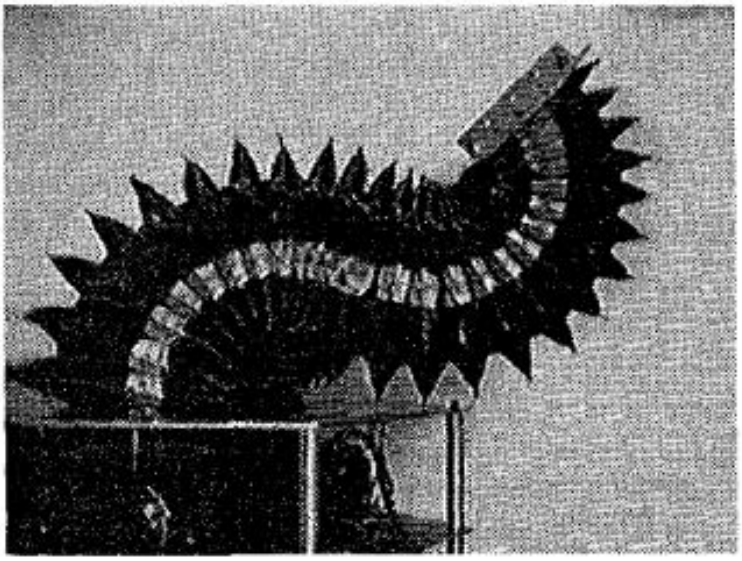

Figure 1.1: Kinetic Sciences Inc. tentacle manipulator [11].

of manipulators. As seen in this figure, 37% of the early continuum manipulators described in that work have medical device applications [12]. For an additional perspective, Walker reviewed continuous backbone robotics [13].

1.2.1 Medical Devices

There have been a number of continuum robots developed to aid in medical procedures by improving the ability to steer the instrument to the desired point of interest in the body. These structures tend to be constructed of shape memory alloy (SMA) structures and actuators. SMA medical applications include an active endoscope composed of sections of SMA spring actuators around a central coil spring [14] and active forceps composed of co-radial SMA tubes to allow surgeons greater range of operation during laparoscopic surgery [15]. Phee *et al.* reviewed the possibility of active colonoscopes for colonoscopy [16], considering actuators such

Table 1. A sampling of snake-like robot designs the shape of which has been or could be described using constant-curvature kinematics. Intended to be exemplary, not comprehensive. Inspired by the classifications of Simaan et al. (2004), Hirose (1993), and Robinson and Davies (1999).

	Classification criteria								
Literature	Continuous/ discrete	Extensible	Number of sections	Actuators/ section	DOF/ section	Actuator spacing	Actuation	Multi-section coupling**	Application
Tensor arm (Anderson and Horn 1967, 1970)	D		4	4	2	90°	Tendon	Co-radial	Underwater manipulation
OCRobotics (Buckingham 2002; Robotics 2008)	D		5	3	2	120°	Tendon	Distributed	Reactor repair
Elephant trunk (Hannan and Walker 2003)	D		4	4	2	90°	Tendon/spring	Co-radial	Bioinspired manipulation
Elephant trunk (Cieślak and Morecki 1999)	C		3	2	2	90°	Tendon/spring	Co-radial	Liquid transportation
EMMA (Bostelman et al. 1997) (see also http://www.templeallen.com/)	D		3	3	2	120°	Tendon/spring	Co-radial	Sanding, nuclear
Backbone (Gravagne et al. 2003)	C		1	1	1	180°	Tendon/rod	N/A	General purpose
Tentacle robot (Li and Rahn 2002)	C		2	4	2	90°	Tendon/rod	Co-radial	General purpose
Arthroscope (Dario et al. 2000)	D	○	1	1	2	180°	Tendon/rods	N/A	Arthroscopy
Catheter (Camarillo et al. 2008, 2009a)	C	○	2	2	3	90°	Tendon/sleeve	Distributed	Cardiac surgery
Colobot (Chen et al. 2004, 2005, 2006)	C	○	1	3	3	120°	Pneumatic	N/A	Colonoscopy
OctArm (Jones and Walker 2006a,b)	C	○	3	3	3	120°	Pneumatic	Individual	General purpose
Slim Slime 1 (Ohno and Hirose 2000, 2001)	C	○	6	3	3	120°	Pneumatic	Individual	Search and rescue
Slim Slime 2 (Aoki et al. 2002, 2004)	C	○	2	3	3	120°	Tendon/pneumatic	Co-radial	Search and rescue
Air-OCTOR (Jones and Walker 2006b)	C	○	2	3	3	120°	Tendon/pneumatic	Distributed	General purpose
KSI (Immega 1994; Immega and Antonelli 1995; Immega et al. 1995)	C	○	2	3	2	120°	Tendon/pneumatic	Distributed	Nuclear decontamination
Active catheter (Bailly and Amirat 2005)	C	○	3	3	2	120°	Hydraulic	Individual	Cardiac surgery
DDU (Simaan et al. 2004; Xu and Simaan 2008)	C		3	3	2	120°	Multibackbone	Co-located	Laryngeal surgery
Active cannula (Dupont, et al. 2010; Webster et al. 2009)	C	○	$2n$	1	2	–	n curved tubes	*	Surgical dexterity
Beveled needle (Webster et al. 2006a)	C	○	∞	0	3	–	Tip/tissue	Individual	Surgical dexterity

*Could be considered co-located or continuously distributed: see Section 3.2.3.
**See Section 4.

Figure 1.2: Applications of Continuum Robots reproduced from Webster and Jones [12].

as the SMAs used in the active endoscope [14], and the three chamber pneumatic actuators described previously [10], as well as other techniques involving pneumatic bellows with vacuum clamping.

Medical tooling has continued to be developed for additional surgical applications. Peirs *et al.* designed a tool guiding tip for minimally invasive surgery consisting of four tendons around a super-elastic nickel titanium (NiTi) core [17]. Degani *et al.* developed a follow-the-leader manipulator for minimally invasive robotic surgery with a steerable outer segment around a inner segment which provides structure as the outer segment extends into the body [18]. Revisions of this concept developed into the CardioArm with focus on heart related surgeries [19]. Harada developed a laser manipulator with a central fiber controlled by four radially located tendons for *in utero* procedures and demonstrated the feasibility *in vitro* and *in vivo* [20]. Steerable catheters have been developed with SMA actuators [21] and tendon actuation [22]. As mentioned previously, the other large research area for continuum robotics is soft robotics.

1.2.2 Soft Robotics

Soft robotics is a field of robotics which has rapidly expanded in the last decade. Potential applications of soft robotics include health care, exploration, wearable robotics, and human assistance. Soft robots contain little to no rigid material which allows them to deform to their environment while causing minimal damage to themselves or those they interact with. Due to the emerging nature of

soft robotics there is the need to re-examine both the materials used to construct them and the mechanisms used to design soft robots [23]. As part of an emerging field, the order of stiffness allowable to still be considered a soft robot is an open question, but there are examples of soft robots working alongside hard robots and designs of robots with hard and soft features to provide additional functionality.

For example a soft combustion powered jumping robot [24] can have similar jumping behavior to a jumping robot designed with a gradient of rigidity to protect the robot during landing [25]. A robotic system was demonstrated that used a robotic platform to transport and carry the hardware for the soft robotic manipulator which deployed from the platform to perform a task such as retrieving an object [26]. If the hardware is not carried on a companion robot, the ultimate goal is untethered operation.

The method to provide working fluid to the actuators for untethered operations is another area of active research. Chemical reactions have been studied as one method to generate pressure without a pump for untethered operations [27]. Wehner *et al.* consider the trade-offs of using battery operated micro-compressors or cylinders of high-pressure gas for untethering soft robots [28]. They also consider the possibility of combustion or chemical decomposition which both require future research for soft robot system integration. Options such as micro-compressors provide pressures and flow rates ranging from 0.2-0.55 MPa and 1.7-10.7 SLM, with a run time limited by the energy consumption of the compressor and size of the chosen batter, while cylinders provide high pressure and flow rates ranging from 5.6-30 MPa with 18-650 SLM, but operating cycles limited by cylinder volume. Pressure generation has been

an area of focus due to pneumatic actuators being commonly used.

For soft robotic applications, common actuation schemes rely on pneumatics [29], shape memory alloys [30], externally actuated tendons [31], and electroactive polymers (EAP) [32]. Pneumatic actuation schemes include pneumatic bellows, pneumatic artificial muscles, and multi-chamber actuators where shape change is achieved through pressurization of a chamber. Wakimoto *et al.* developed miniature pneumatic bellows using a micro-machined mold and placed them as part of the three-fingered hand, the scale of a tip of a finger, to demonstrate the grasping of a fish egg. [33]. Laschi *et al.* proposed an EAP actuated octopus-inspired arm which contains both transverse and longitudinal muscles inspired by the muscular hydrostat structure of octopus [34]. The properties of silicone elastomers were studied to build and validate a cable actuated mock-up of the EAP design. EAPs tend to have low actuation stress, 0.3 MPa, while SMAs tend to have low strains, 0.1, when compared to pneumatic actuators, 16 MPa and strains of 0.4 [9].

Examples of hybrid soft robots include a tapered pneumatic bladder deformed by twelve externally actuated tendons [35], and AirOct, a section of flexible air ducting which can be pneumatically lengthened and mechanically bent by tendons running the outside of the section [36].

There are numerous soft crawling robots drawing inspiration from worms or other flexible creatures. Arena et al. created an EAP actauted inch-worm robot which could crawl in a straight line across the table-top [37]. The Meshworm is a nickel titanium coil spring actuated peristalic crawler [38]. Yuk *et al* designed a twelve section planar SMA spring actuated crawling robot [39]. Umedachi *et al.*

built a SMA or motor tendon actuated crawling robots, Softworms [40]. Mao *et al.* made a simple five arm five actuator SMA tethered starfish which could crawl over pebbles and small rocks [30]. Both SMAs and EAPs have been applied to crawling robots.

There is interest in taking existing actuators and externally augmenting their structure to provide a new desired behavior. Galloway *et al.* added an exterior sleeve to the bending fiber-reinforced actuators to control and limit the bending to a subset of shapes, which can approach joint-like structures with certain sleeve designs. These actuators were incorporated into a gripper that could more securely grasp desired shapes such as boxes, Fig. 1.3 [41]. Deimel and Brock present a tapered pneumatic fiber-reinforced actuator, PneuFlex, used on a soft hand which can complete a variety of different grasps with five finger and two palm actuators [42]. Galloway *et al.* used two soft fiber-reinforced hydraulic actuators and applied these to grippers for deep sea sampling [43]. The first is an actuator that couples bending and twisting by incorporating a single fiber reinforcement to wrap around an object, and the second takes the PneuNet bellows actuators and incorporates fiber reinforcements to increase the pressure capability from 60 kpa [44] to 160 kpa [43].

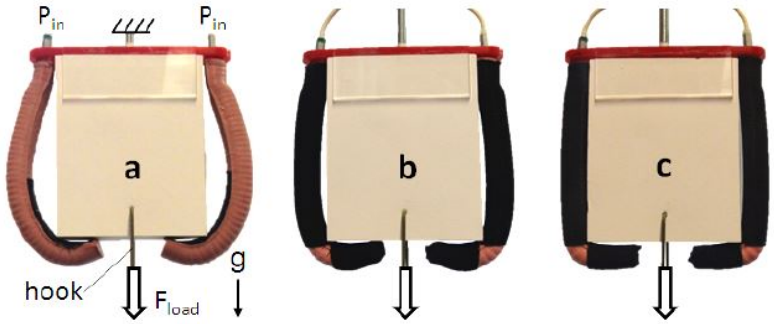

Figure 1.3: Pneumatic bellows with added sleeves to localize bending [41].

In addition to the pneumatic bellows, there are a number of soft robots actuated by pneumatic artificial muscles. Walker *et al.* details the cephalopod inspiration and initial design of the OCTARM, a four section, twelve extensile PAM manipulator [45]. The OCTARM has been mounted on a treaded vehicle to move and place it in grasping distance of obstacles such as a traffic cone and basketball [29]. Trivedi *et al.* refined the OCTARM with a three-section design [46]. Giri and Walker studied grasping various objects with the OCTARM such as a toy car and carton of eggs, Fig. 1.4 [47]. These arms were grasping relatively lightweight objects of approximately 5 lbs. or less.

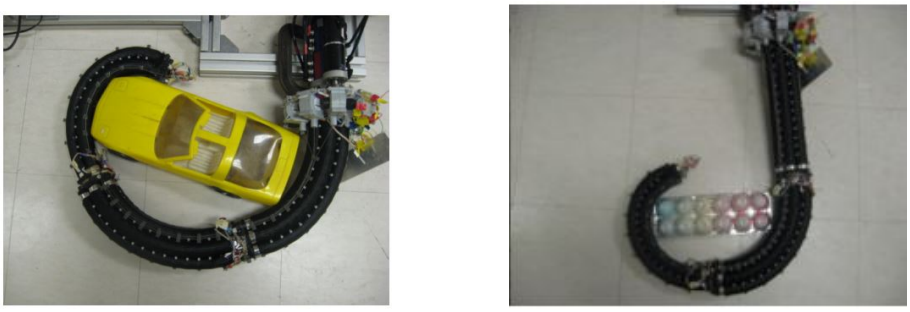

(a) Car (b) Eggs

Figure 1.4: OCTARM grasping different objects [47]

Bartow *et al.* details a large contractile arm that hooks onto smaller objects such as headphones, Fig. 1.5 [48].

Kang *et al.* constructed a six section, 24 PAM arm to mimic functionality found in octopus such a traveling bend point during reaching and whole arm grasping [49]. Kang *et al.* further refined and tested a four section, twelve PAM extending manipulator, and related the model to Euler Angles [50]. Kim *et al.* designed a three section arm with a simple motion tracking system [51]. Additional perspectives on

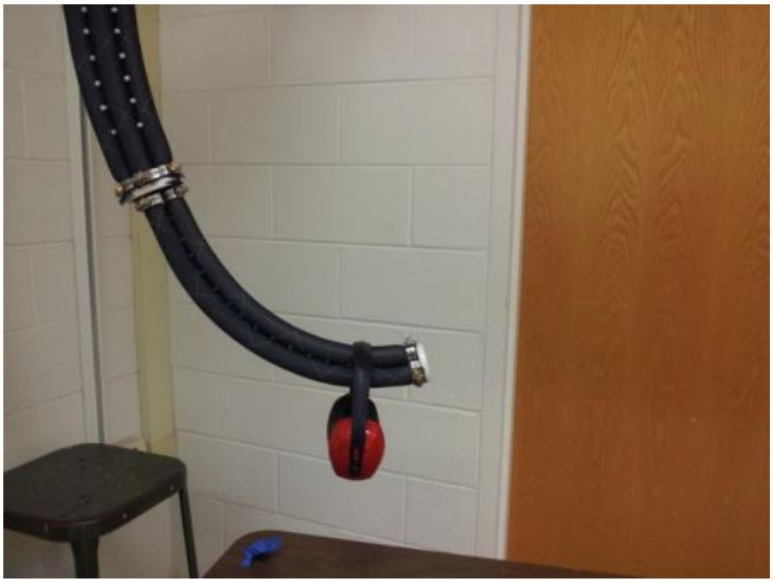

Figure 1.5: Contractile PAM Manipulator [48].

the field of soft robotics can be found in the review by Rus and Tolley [52], and the review of types of deformations and actuation in the review of "soft matter robotics" by Wang and Iida [53]. After constructing a manipulator there is a need to model its movement for the purposes of design improvements, simulation, and control.

1.2.3 Continuum Robotics Modeling

Chrikjian and Burdick developed the modeling framework to approximate hyper-redundant manipulators as a continuum described by a backbone curve using an integral formulation [54]. Continuum robot modeling uses a continuous model of the manipulator such a beam or rod to describe the motion of this backbone curve or introduces simplifying assumptions, like constant section curvature, to reduce the continuum equations.

Figure 1.6: Extensile PAM Manipulator grasping ball [49].

1.2.3.1 Continuum Models

Continuum models of continuum robots are models which consider the distributed force, actuation, and material properties along the length of the manipulator. These methods usually model the manipulator as an Euler-Bernoulli beam or Cosserat rod to predict the behavior along the length. The use of beam/rod models makes these techniques particularly useful for manipulators with an elastic backbone. Gravange *et al.* modeled a planar spring steel backbone manipulator by first calculating the energy to deform the beam and then using Hamilton's principle to formulate the large deflection dynamics of a the manipulator. This worked showed support for the constant curvature model when the model was evaluated while neglecting temporal effects [55]. Trivedi *et al.* develop a geometrically exact modeling approach using a Cosserat rod model for each section of the manipulator to account for the effects of gravitational loading [56, 57]. They noted the large error associated with the constant curvature model, 50-100% the length of the arm, when compared to the full-order rod model, 5% the length of the arm, but were comparing a purely kinematic application of the constant curvature model, i.e. neglecting gravity and other loads, to the static equilibrium of the rod model. In his review, Walker notes "the deviation from constant curvature in free space is typically not large", when considering gravity effects and not only the purely kinematic equations as was done by Trivedi *et al.* [13, 57].

Geometrically exact models using Cosserat rod theory for a cable driven continuum arm were validated using 3D video reconstruction to determine the

shape and loading during deformation resulting in a tip position error of less than 6% of the arm length [58]. Mahvash *et al.* used a special Cosserat rod model to implement a stiffness controller for a concentric tube robot [59]. A planar three-section manipulator was modeled as a one-dimensional Cosserat rod in each section, ignoring shear and extensibility. This model showed less then 1% error in tip position for the five experimental mass added to a three section NiTi backbone manipulator [60]. Giorellia *et al.* developed Jacobian and neural network based inverse static methods for a tendon actuated soft arm model as an Euler-Bernoulli beam [61]. Rod modeling has also been used at the actuator level to describe the single degree of freedom bending of a pneu-net actuator. [62]. Continuum models can be accurate, ¿5% (of the manipulator length) error in tip position, based on Cosserat rods when the motion being modeled is well understood like with a concentric tube robot or when video reconstruction can be used to identify the deformation along the whole manipulator.

1.2.3.2 Constant Curvature Models

To eliminate the necessity of continuum models a common assumption is that each section of the manipulator follows a circular arc. This allows the kinematic expressions to be written in a closed form as shown by Webster *et al.* for the planar kinematics of a steerable needle [63]. Additionally, the closed-form relationship allowed the investigation of the effects of actuator length limits on motion and the calculation of tangling and untangling of tendons passing through multiple sections

for real time kinematic applications [64].

Tatlicioglu *et al.* calculated the planar dynamic model using the constant curvature assumption for a three-section PAM manipulator like the one in Fig 1.4 [65]. The model developed includes gravitational energy as well as the energy to extend and bend a segment. The energies were integrated over each section of the arm to find the total energy and calculate the Lagrangian dynamics. These dynamics were used to conduct simulation on the behavior of the arm in both open and closed-loop operation assuming the control inputs were the force to extend the section and torque to bend the section .

Constant curvature methods are calculated in terms of state variables of section curvature, bending plane, and length, but for a three actuator intrinsic manipulator, there is control of the actuator lengths which lead to changes in all three variables. To develop models in terms of the control lengths and forces of the muscles, Godage *et al.* introduced shape functions based on the polynomial relationships between the length of the actuators for a PAM actuated continuum robot [66]. The expansions used in that work allow the mathematically singularity associated with a straight arm configuration to be avoided. These equations were further simplified by considering the center of gravity of the section assuming uniform weight distribution. This center of gravity formulation was compared to the total energy of both the integral and discretized formulations of a single section. While the authors expected the potential energy should be exact and only small differences in the kinetic energy are expected, a mass correction factor of $1/0.57$ was required for the center of gravity method [67].

Constant curvature kinematic analysis was applied to the Festo Biological Handling Assistant (BHA), a multi-chamber pneumatic bellow manipulator, and validated the kinematic relationships comparing Vicon motion capture data to cable length measurements [68]. The BHA was also used to study the effect of the bio-mimetic tapered shape of the BHA and develop a variable constant curvature approximation which breaks down each gross section into a number of subsections of approximately constant radius, requiring a knowledge of how many points in the sections are deforming [69].

He *et al.* developed dynamic expressions for a manipulator consisting of a elastic NiTi backbone robot actuated by three NiTi wires [70]. First they developed an energy formulation for each component, and then calculated and applied correction factors for each of the wires and backbone which are polynomial functions of the bending. In this work, the manipulator is dominated by elastic energy when compared to gravitational energy. Constant curvature planar kinematic modeling was also applied to a long thin NiTi backbone manipulator with length change due to the addition of compression springs [71]. Constant curvature was used in developing the dynamics of an elastic backbone manipulator using virtual power or Kane's method. Static and dynamic steady-state analysis agree with FEA in equilibrium when considering the effects of actuator and gravitational loading on the manipulator in a planar case. The manipulator was calculated as ten unit sections due to the ten discs placed along the arm to guide the tendons and promote bending [72]. Rone and Ben-Tzvi applied this model to enhance state estimation for two section manipulator using passive cables to measure section shape change [73].

Constant curvature has been used for 2D planar tracking control of a multi-section manipulator actuated by antagonistic PneuNet actuator pairs [74]. Webster and Jones review constant curvature model formulations and place them in a common notation to show the equivalence of different notation choices and formalisms [12]. Constant curvature is a useful when working with the motion of the rigid section divisions common in intrinsically actuated soft robots.

1.2.3.3 Additional Models

Additional modeling techniques have been tested including modeling as mass spring systems, neural networks, and model free systems. There was a study of octopus arm motions, specifically the propagating bend point, which modeled the arm as a planar arrangement of masses and springs to study this reaching motion [75]. Another combination of linear and rotary springs was also used to model the planar bending of a NiTi spine surgical manipulator with additional linear springs modeling the tendon actuator behavior [22].

Forward and inverse kinematics were calculated using neural networks for a path tracking kinematic controller [76]. A neural network was also used for the inverse static model of BHA which was determined from large number of equilibrium positions using a Constrained Extreme Learning Machine [77].

Vikas *et al.* posed crawling with a three limb NiTi crawler as an optimization problem on directed graphs for model free locomotion strategies [78]. Zhang *et al.* considered static equilibrium at the end disc of a PAM actuated arm section resulting

in large errors at the tip [79]. This work considered a section actuated by three contractile muscles with central extensile PAM. The actuator modeling only used the Gaylord force model which is known to grossly over-predict PAM force-stroke behavior.

1.3 Pneumatic Artificial Muscles

Pneumatic artificial muscles have been used in numerous soft robots as well as in many traditional robotic applications.

1.3.1 Background and Motivation

Pneumatic artificial muscles are soft actuators which generate an axial force and motion when pressurized. PAMs were created by Gaylord [80] and popularized by McKibben for orthotic applications, and as such are known as McKibben actuators. Additional names for PAMs include pneumatic muscle actuators, Rubbertuators, pneumatic rubber actuators, and air muscles. PAMs are a part of a larger class of fiber-reinforced pneumatic actuators, specifically fiber-reinforced actuators with symmetric pair of fibers [81].

The compliant nature of PAMs and the ability to use a number of working fluids make them a natural choice for soft robotic applications. Additionally, PAMs have been tested to over 120 million cycles without failure, with no degradation of performance observed [82]. The increased efficiency of hydraulic actuation, 40-60%, has been reported when compared to pneumatic actuation, 25%, up to 30 MPa [83].

This efficiency was calculated as the work the PAM does through one cycle related to the fluid input energy to compress and pressurize the working fluid. For soft robotics, the ability to use both air and water allows the robot to be adapted to the environment where the robot is operating. To successfully use PAMs in robotic applications requires an accurate model of the muscle force-stroke behavior.

1.3.2 PAM Literature Review

1.3.2.1 Modeling of Pneumatic Artificial Muscles

Along with creating PAMs, Gaylord produced a geometric model for the PAM force, F, which ignored effects of the bladder, hysteresis, and non-cyclindrical shape of the actuator

$$F = \frac{P\pi D^2}{2}\left(3\cos^2\theta - 1\right) = \frac{P}{4\pi N^2}\left(3L^2 - B^2\right) \tag{1.1}$$

where P is the pressure in the PAM, D is the actuator diameter, N is the number of turns a braid around the actuator, θ is the angle of the braid as measured from a line perpendicular to the length, L is the current length of the muscle, and B is the length of the braid. D, θ, and L all vary as the PAM contracts and can be related geometrically through the fixed length of the braid and the number of turns the the braid makes about the bladder. Subsequent research used more detailed modeling techniques to include the effects of the bladder and PAM shape not included in the Gaylord model.

Schulte introduced a modified form of the Gaylord equation which included terms to model the bladder elasticity, braid to braid friction, and braid to bladder friction. Schulte noted these terms were probably non-linear and difficult to determine experimentally [84].

Chou and Hannaford considered a principle of virtual work approach to avoid the geometric complexity of the PAM [85]. The first equation developed mirrored the work of Schulte . The bladder thickness was also incorporated to further improve the model used. Klute and Hannaford introduced the energy to deform the bladder to the virtual work model assuming a Mooney-Rivlin material model [86]. Kothera *et al.* further improved the energy balance model by considering the effect of non-constant bladder thickness, followed by corrections for the braid energy, and non-cylindrical tip shapes [87].

As a alternative method, Ferraresi *et al.* developed a force balance model based on an isotropic tube with linear elastic material properties [88]. Kothera *et al.* refined the force balance model in similar fashion to their virtual work improvements. First, a non-constant thickness effect was added, then the non-cylindrical tip shape effect was added [87]. In that work, force balance was shown to better model PAM behavior (less error at blocked force and free contraction) before and after applying corrections to the model. Further improvements were made to the force-balance model with the introduction of non-linear polynomial stress-strain bladder models and non-zero dead-band pressure corrections which were independently fit for each test pressure [89]. Robinson *et al.* extended the quasi-static force balance model to capture the effect of antagonistic stretching of a PAM [90].

Table 1.1: PAM Model Comparison

Model	Type	Bladder Model	Additions and Corrections	Parameters
Gaylord [80]	Virtual work	N/A		
Schulte [84]	Virtual work	N/A		
Chou and Hannaford [85]	Virtual work	N/A	Non-constant thickness	
Chou and Hannaford [85]	Variable Stiffness Element	N/A		6 parameter fit
Klute and Hannaford [86]	Virtual work	Mooney-Rivlin		2
Kothera et al. [87]	Virtual work	Mooney-Rivlin	Braid elasticity	2
Ferraresi et al. [88]	Force balance	Linear elastic		2
Kothera et al. [87]	Force balance	Linear elastic	Non-constant thickness and tip effects	2
Hocking and Wereley [89]	Force balance	4^{th} order polynomial	Non-constant thickness dead-band pressure, and tip effects	4 per pressure
Robinson et al. [90]	Force balance	4^{th} order polynomial	Non-constant thickness and elliptic tip effects	4 per pressure
Chapter 2	Force balance	Linear and cubic polynomial	Non-constant thickness and dead-band pressure	4
Chapter 4	Force balance	Mooney-Rivlin	Non-constant thickness	2

Tondu provides an overview of PAM modeling techniques [91]. Recent work has studied the dynamics for two PAM systems under a constant load considering friction and the air handling system. These models were fit to a single test case for each system, by varying the braid bladder interaction friction coefficient [92]. Liu and Rahn develop a detailed membrane model which is able to capture the actuator lengths and radius changes at low non-dimensional pressures [93].

1.3.2.2 Miniature PAMS

Miniature PAMs or PAMs with outer diameters on the order of millimeters have received interest for more compact applications and the use of bundles of smaller muscles in place of one larger muscle, similar in function to human muscle fibers. Devolder *et al.* fabricated miniature PAMs with diameters on the order of 1.5 mm and qualitatively compares a modified Gaylord model to experimentally obtained force-pressure relationships [94]. Solano and Rotinat-Libersa tested miniature hydraulic McKibben muscles and attempted to predict performance by relating the hydraulic cylinder displacement to the PAM motion [95]. Chakravarthy *et al.* also fabricated and characterized miniature PAMs with diameters of 1.2 mm for application to surgical tooling [96].

Vashisth *et al.* studied morphing applications using a series of 2 mm diameter miniature fluidic flexible matrix composites, which are essentially PAMs with the fibers embedded in the bladder [97]. Hocking and Wereley studied MiniPAM fabrication and testing, noting the degraded contraction performance, 8% actuator length,

when compared to full-size PAMs, 30-40% actuator length. They also identified the need to cycling the PAM prior to testing to eliminate the Mullins effect [98], a property of rubbers where the stress-strain profile changes when the material is subjected to a higher strain than previously experienced by the material [89].

1.3.2.3 Robotics Applications

The soft robotic applications of PAMs have been discussed previously, but there exists a much larger body of work of PAMs as actuation devices in traditional robotic applications. Pneumatic artificial muscles have been applied to robot arms, hands, and legs due to their desirable actuation properties.

PAM actuated arms include the Anthroform Arm designed Hannaford *et al.* to study models of the central nervous system [99]. Boblan *et al.* created a human-like arm and hand actuated by Festo Actuators [100]. Tondu *et al.* constructed a 7 degree-of-freedom (DOF) PAM robot arm and demonstrated its ability to complete tele-operated pick and place activities, Fig. 1.7a [101]. Robinson *et al.* designed a planar heavy lift robot arm, Fig 1.7b, capable of lifting over 200 lb with a maximum of 200 psi for casualty extraction, which was used to test control schemes including adaptive sliding mode and radial basis function neural network adaptive controllers [102].

Vermeulen *et al.* created the planar walking robot, Lucy, Fig. 1.8, using Pleated PAMs, pneumatic muscles which use a pleated instead of braided restraint layer [103]. These pleated muscles generate higher forces, but require more volume

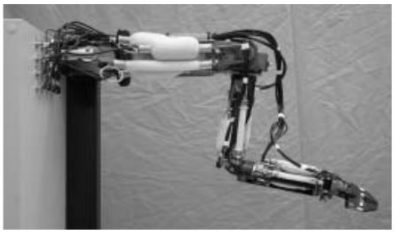

(a) 7 DOF arm [101]

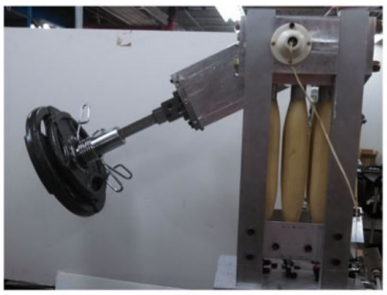

(b) 1 DOF arm [102]

Figure 1.7: PAM actuated arms

for the larger radial expansion. Colbrunn *et al.* designed and tested a walking PAM actuated leg with Shadow Air Muscles [104].

Lee and Shimoyama designed a skeletal hand actuated by miniature PAMs [105]. Rothling *et al.* studied grasping with a 9 DOF hydraulic hand and 20 DOF Shadow Hand, Fig 1.9, and after grasp optimization the hands were able to grasp nearly all 20 object excluding a ring of keys (both hands) and pencil (9 DOF hand) [106].

For additional uses of PAMs, Woods *et al.* combined a PAM design with a pneumatic cylinder to create the PushPAM. The PushPAM converts the contraction of the PAM to an extending motion like a pneumatic cylinder while retaining the high force output of a PAM [107]. Vocke *et al.* packaged two antagonistic PAMs in a compact package as an alternative to an electric servo motor for MAV control surface applications. The PAM actuation package demonstrated similar displacement performance up to 20 Hz with a very large DC torque that motors lack [108].

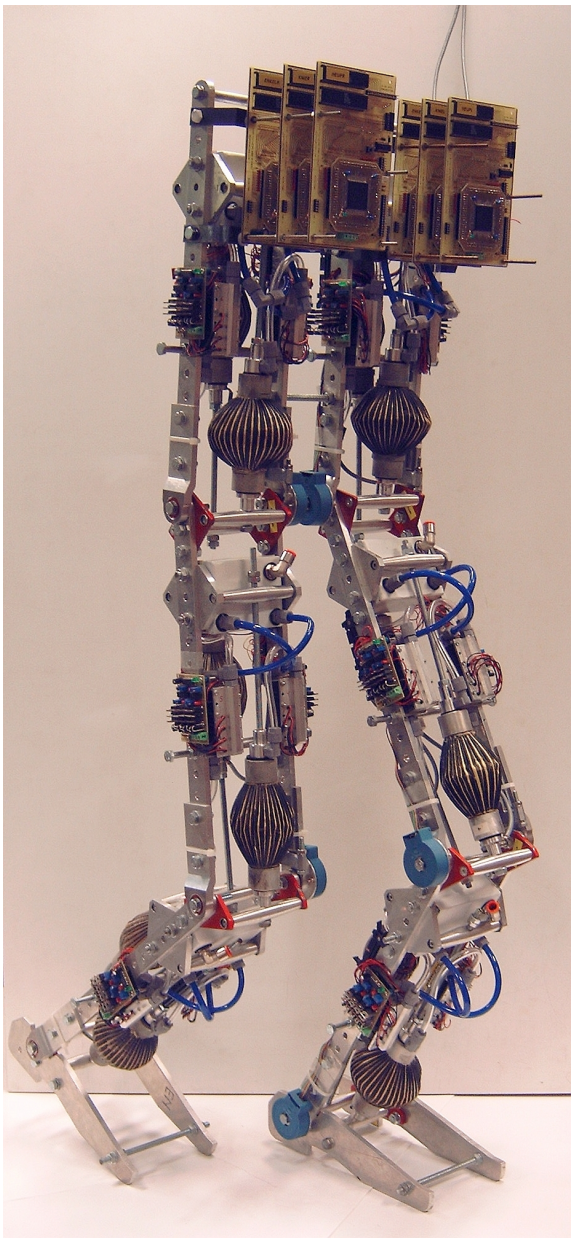

Figure 1.8: Bipedal walking robot [103].

Figure 1.9: Shadow Dexterous Hand used to study grasping [106].

1.3.2.4 Other PAM Applications

PAMs were originally designed for orthotic applications, and there have been additional applications in rehabilitation and aerospace engineering. For example, Park *et al.* used PAMs placed on the lower leg for ankle rehabilitation [109]. Tadano *et al.* produced a grip amplified glove powered by PAMs which responded to EMG signals [110].

In aerospace applications, PAMs have been used to actuate both traditional control surfaces as well as morphing aircraft concepts. PAMs were used to actuated a helicopter blade traveling edge flap [111]. A morphing trailer edge spoiler was tested using contracting and extending PAMs embedded in polyurethane to maintain an aerodynamic surface during deformation [112]. Morphing aileron with two sets of contracting PAMs were designed to match conventional aileron performance [113]. Chen *et al.* tested arrays of PAMs embedded in a soft skin for the ability to deform as a morphing skin and support surface pressures, such as aerodynamic loading [114]. Zhu et al analytically studied the effect of embedding PAMs in a matrix [115].

1.4 Contribution of Dissertation

The contributions of this research are in the areas of pneumatic artificial muscles testing, modeling, and characterization and application of PAMs to soft robotics. This work showed the effect of increased bladder thickness on decreasing the free contraction and blocked force of a PAM while also increasing the dead-band pressure. The data from this study of bladder effect on miniature PAMs was used to

contribute to PAM modeling literature by generalizing polynomial bladder models across the range of test pressure, reducing the number of parameter needed to fit the data. A second PAM model applied Mooney-Rivlin solid mechanics to the bladder model to bring PAM modeling closer to predictive force-stroke modeling.

This work contributed the first force-extension curves to PAM literature and provided a testing procedure to allow other researches to investigate the full force-stroke profiles of extensile PAMs. With this new data, contractile PAM modeling techniques could be applied and validated for extensile PAMs. This model application allowed contractile and extensile PAMs to be parametrically studied developing performance metrics comparing the two types of actuators.

The research into PAM applications for soft robots led to the introduction of structures inspired by the ossicles of brittle stars. This work demonstrated the impact of these bio-inspired structures for both a single soft robotic arm section and a multi-section arm. A dynamic model of a multi-section arm was developed considering not only the continuously bending sections, but also the rigid PAM attachment sections. A static version of this model was experimentally validated for both the single and multi-section arm by comparing the actual test pressure to the pressure determined from the model.

1.5 Overview of Dissertation

Chapter 2: Effect of Bladder Wall Thickness on Miniature Pneumatic Artificial Muscle Performance. Investigate the degraded performance of miniature PAMs

by creating custom silicone bladders. The in-house molded silicone bladder demonstrated that the previously noted degrade performance was a material availability issue and not a scale issue. With this molding process, a set of PAMs with custom bladder sizes are then used to conduct a study of the effect of bladder thickness on PAM blocked force, free contraction, dead-band pressure, and hysteresis.

Chapter 3: Comparison of Contractile and Extensile Pneumatic Artificial Muscles. Contractile and extensile PAMs were constructed at two sizes to compare the force, work, and stroke of the two types of PAMs to facilitate the choice of type of actuator to use in a soft robotic manipulator. Experimental process for testing was developed to report the first experimental force-stroke curves for extensile PAMs. Contractile PAMs force models were validated for extensile PAMs, and these models were used to conduct a parametric study of varying braid angle and diameter at both scales. From this research contractile PAMs were chosen to construct the soft robotic manipulator tested in Chapter 5.

Chapter 4: Non-linear Quasi-static Modeling of Contractile and Extensile Pneumatic Artificial Muscles. PAM modeling such as the model developed in Chapter rely on parameter estimation to reconstruct the experimental measurements and is useful for engineering analysis, but can not be used for predictive PAM force contraction prediction. This work uses finite strain theory to apply a Mooney-Rivlin model of the bladder stresses to the force balance model, which has been shown to have better agreement with experimental data. As in the previous chapter this model is developed for contractile PAMs and then extended to extensile PAMs.

Chapter 5: Single-section modeling of PAM soft robot with distinct section

breaks. Develops the mathematical model of the single-section manipulator. Studies the effect of the addition of ossicles to a single section of the manipulator, and shows the benefit of adding ossicles to a section. Validates the quasi-static model pressure to experimental pressure and angle data for loads up to 5 lbs.

Chapter 6: Multi-section modeling of PAM soft robot with distinct section breaks. Extends the single section mathematical model to the multi-section manipulator. Studies the effect of the addition of ossicles to the multiple section manipulator, and shows the benefit of adding ossicles. Validates the quasi-static model pressure to experimental pressure and angle data.

Chapter 7: Conclusions and contributions of this research as well as directions of future work. Future work for the continued and expanded use of ossicle inspired structures in PAM soft robots and control of PAM soft robots.

Chapter 2: Effect of Bladder Wall Thickness on Miniature Pneumatic Artificial Muscle Performance[1]

2.1 Introduction

Pneumatic Artificial Muscles (PAMs) are actuators that are effective in a range of applications due to their light weight, high power to weight ratio, and high fatigue life [82]. PAMs were invented in the 1950s by J.L. McKibben for orthopedic use, and then commercialized by Bridgestone as the Rubbertuator in the 1980s [91]. PAMs have more recently been studied for aerospace applications including trailing edge flaps [111], morphing trailing edges [112], and morphing ailerons [113]. For robotics applications they exhibit controllable compliance, a low operating pressure and excellent static performance, making PAMs a safe actuator for human interaction. Robotic research has considered PAMs as actuators for arms [99, 101, 116], legs [103], and hands [100, 105, 106]. The controllable compliance makes PAMs a natural candidate for prosthetic systems which are likely to utilize arrays of pneumatics muscles [109, 117]. Full-scale PAMs, i.e., PAMs with diameters on the order of tens of millimeters, have been well studied in research with a variety of modeling techniques

[1]Pillsbury, T.E., Kothera, C.S. and Wereley, N.M., 2015. Effect of bladder wall thickness on miniature pneumatic artificial muscle performance. Bioinspiration & biomimetics, 10(5), p.055006.

to draw upon. PAMs have been modeled with both energy balance and force balance approaches [87, 91]. Additionally, hyperelastic bladder models have been developed to better model the elastic energy effect on PAM force [118]. Applying these models to control has been shown to produce accurate responses in PAM systems [119, 120].

Small scale, or miniature, PAMs, which denote those having diameters on the order of millimeters, have the same benefits of full scale PAMs, such as a lightweight design and high power to weight ratio, as well as a greatly reduced actuator volume compared to full scale PAMs. This volume reduction is ideal for small robotic applications, such as robotic hands or prostheses, where large number of actuators are needed for actuation of multiple degrees of freedom in compact spaces. However, reducing PAM size to small diameters increases fabrication and modeling difficulties. Low force and contraction outputs have been reported for miniature PAMs [97, 110]. At small scales, commercially available material choice is greatly limited, leading to PAMs with lower contractions than those reported for full scale PAMs. Hocking and Wereley tested miniature PAMs with a silicone bladder which was found to stiffen with increasing contraction, limiting the obtainable free contractions to 8% at 0.55 MPa [89]. Small scale hydraulic actuators have been shown to achieve higher free contraction ratios, 20%, but required much higher actuation pressures, 1.5 MPa [95], which may be dangerous for close interactions with humans. Improving miniature PAM performance will benefit small scale robotics [121, 122] and keyhole surgery [94]. Other aerospace applications of miniature PAMs include micro-air vehicle servo packages [108] and morphing structures [114].

In this work, a series of miniature PAMs was fabricated to study the effect that

different bladder materials and thicknesses have on PAM actuation characteristics. The effects of varied bladder materials and thicknesses have been considered for full scale PAMs previously, wherein Meller et al. identified similar trends that stiffer and thicker bladder materials cause decreased force and contraction [83]. In another study on the effects of variations in PAM parameters, this same trend was identified for two different bladder thicknesses considered to improve modeling using a Mooney-Rivlin hyper-elastic material model [123]. Focusing on the importance of the bladder material, a miniature PAM (diameter of 4.2 mm) was created with contraction ratios comparable (∼30%) to those found for full scale PAMs (diameter of 31.8 mm [111]). Based on this initial study, additional PAMs were constructed of the same outer diameter with varying inner diameters, to characterize the effect of bladder thickness on PAM performance. The PAMs were characterized under quasi-static loading to determine the force-contraction profiles of the PAMs. The measured data was used to parameterize force balance models that incorporate a nonlinear stress-strain relationship to gain a better understanding of the model structure required to best capture the experimentally observed behavior, in addition to exploring design trends.

2.2 Characterization of Miniature Pneumatic Artificial Muscles

2.2.1 Performance Metrics

A PAM consists of a braided sleeve surrounding an elastomeric bladder, both of which are joined with a fitting at each end. When pressurized, the bladder expansion is constrained by the braided sleeve, causing the PAM to axially contract

while radially expanding, which produces an axial tension force. Similar to human muscle behavior, PAM force decreases with increasing contraction [85]. Three important performance characteristics of the force-contraction profile are blocked force, free contraction, and dead-band pressure. The blocked force is the force produced by a PAM when it is constrained to its resting length and pressurized. Free contraction is the maximum contraction achievable for a given pressure, and is the point at which the PAM no longer generates any force. A PAM in the blocked force and free contraction conditions is shown in Fig. 2.1a and Fig. 2.1b, respectively. The dead-band pressure is the pressure necessary to initiate PAM actuation, that is, the pressure to overcome the resting stiffness of the bladder. At pressures below the dead-band pressure, the PAM produces zero force and contraction. A PAM with high blocked force and free contraction is desirable, as is a PAM with minimal dead-band pressure.

2.2.2 Experimental Characterization

A set of miniature pneumatic artificial muscles was fabricated from two commercially available bladder materials and a Bluestar Bluesil (V-330) silicone rubber bladder molded in-house [124]. The commercially available bladders were a latex surgical tubing with an outer diameter of 3.175 mm (0.125 in) and a thickness of 0.794 mm (0.031 in), and silicone tubing with an outer diameter of 3 mm (0.118 in) and a thickness of 0.5 mm (0.02 in). For these miniature PAMs, polyethylene terephthalate (PET) braids with a nominal diameter of 6.35 mm (0.25 in) were used.

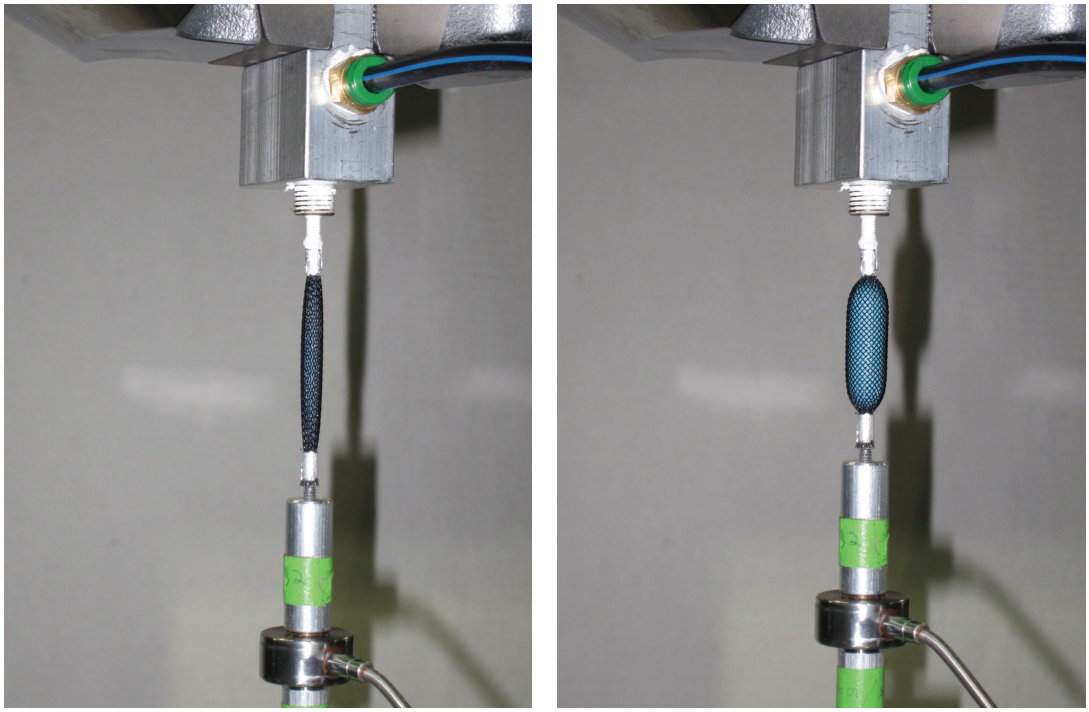

(a) Blocked Force (zero contraction). (b) Free Contraction (zero force).

Figure 2.1: V-330 Bladder PAM Testing at an Inflation Pressure of 483 kPa

Table 2.1 summarizes the bladder and braid properties of these PAMs. Different bladder materials were considered since there are few commercial options at this scale and hardness of the commercial silicone tubing was not available. The braid angle is defined as the angle between the braid and a plane perpendicular to the length axis of the PAM. The PAMs were tested in a Material Testing Systems (MTS) machine to measure the force-contraction actuation curves. The silicone tubing bladder PAM was tested from 207 kPa to 552 kPa (30 psi to 80 psi). The latex bladder PAM had a higher dead-band pressure, so it was tested from 276 kPa to 621 kpa (40 psi to 90 psi). Sample characterization data is shown in Fig. 2.2. The silicone PAM, Fig. 2.2a, stiffened with increasing contraction. This stiffening can be visualized through the increasing negative slope of the force-contraction curve as contraction

increases. The latex miniature PAM, Fig. 2.2b, generated a lower blocked force than the silicone PAM, due to the higher dead-band pressure, but achieved larger free contractions. The latex PAM also exhibited a larger hysteresis effect, the direction of the loading curves is indicated for the highest pressure of each PAM. The high dead-band pressure of the commercial latex bladder, which requires higher actuation pressures to achieve similar force levels with softer bladders, and the stiffening of the commercial silicone bladder both decreased performance of their respective PAM actuators.

The properties of these bladder materials were detrimental to PAM performance and motivated the present study on bladder thickness, highlighting the impact that choice of bladder material has on PAM performance. For improved performance a thin-walled, low stiffness bladder was developed. To achieve this performance improvement, the bladder was molded with a two-part silicone rubber. The bladder was fabricated to have an outer diameter of 3.2 mm (0.13 in) with a wall thickness of 0.4 mm (0.016 in). The liquid silicone was injected using a syringe into the mold, Fig. 2.3, consisting of two outer halves, a mandrel, and centering features. The outer halves contained a semi-circular groove defining the desired outer diameter for the bladder. The mandrel, a dowel pin, matched the desired inner diameter. The V-330 silicone was injected into the mold under vacuum to assist it flowing through the mold and to ensure that the bladder material was fully degassed.

Fig. 2.4 shows the measured force-contraction data for the PET V-330 miniature PAM. The PET V-330 PAM has a comparably negligible dead-band pressure and exhibited higher blocked forces and larger free contractions than the

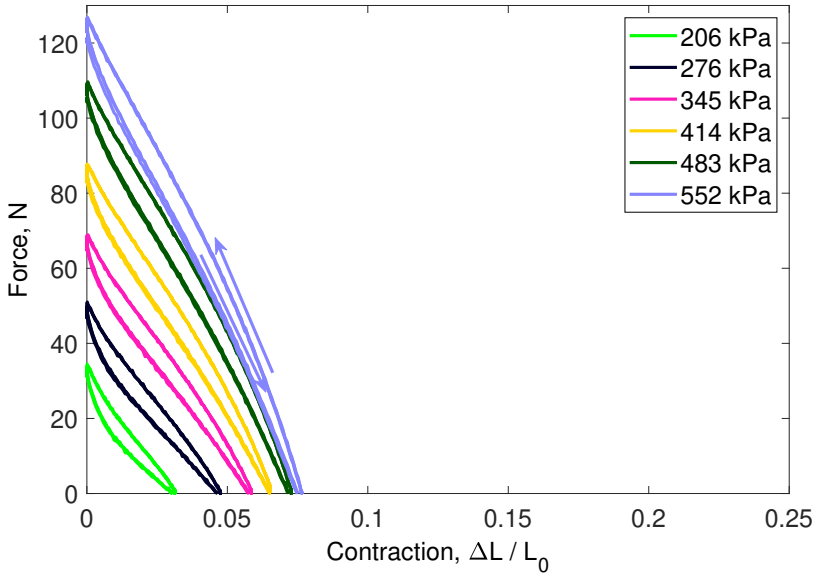

(a) PET Silicone Miniature PAM.

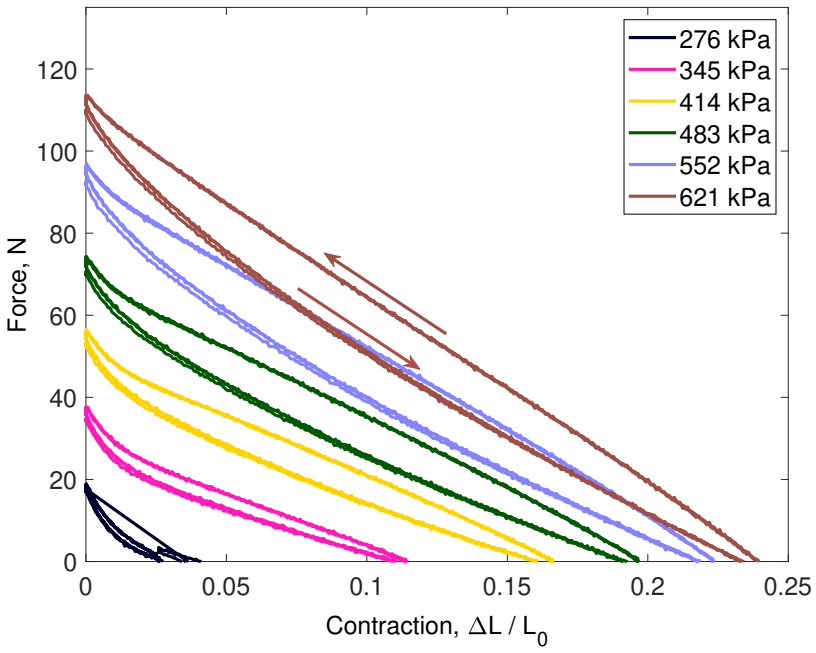

(b) PET Latex Miniature PAM.

Figure 2.2: Force vs. Contraction Test Data for Silicone and Latex Bladder

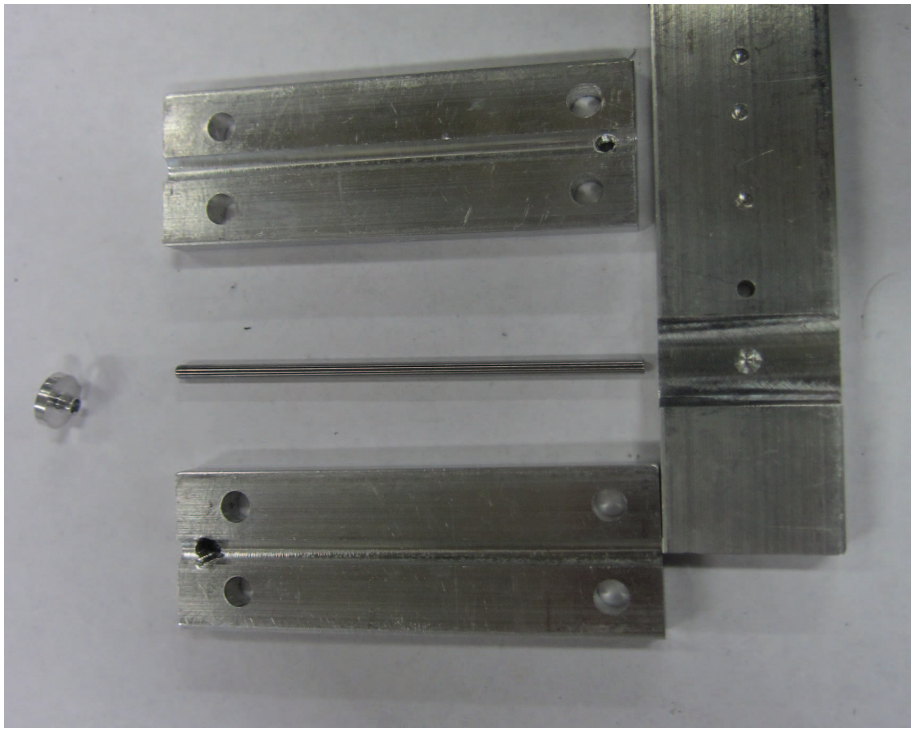

Figure 2.3: Bladder Mold

previously tested miniature PAMs from Fig 2.2. Fig. 2.5 compares the blocked force and free contraction of the three PAMs tested in the initial study. The blocked force plot, Fig. 2.5a, shows similar force outputs for each PAM, but the commercial latex and silicone PAMs do not begin producing force until higher pressures due to the higher dead-band pressure. Comparing free contraction, Fig. 2.5b, the V-330 PAM out-performs the two commercial bladder PAMs, while also requiring lower pressure. For each free contraction curve, a point on the x-axis at the dead-band pressure has been added to more clearly illustrate the pressure at which contraction begins for each PAM. As an example of the improvement, the V-330 miniature PAM exceeded the maximum free contraction of the latex miniature PAM at a pressure below the dead-band pressure of the latex PAM. The greatly improved performance of the low stiffness V-330 silicone bladder motivated a more comprehensive study on the effect

of bladder thickness on performance metrics of miniature PAM actuators, isolating the effect from the diameter and material stiffness changes present in the current study.

Table 2.1: PAM Properties for Initial Study

Bladder Material	Length	Diameter	Thickness	Shore Hardness	Braid Angle
Silicone	41 mm	3.0 mm	0.5 mm	–	75°
Latex	45 mm	3.2 mm	0.8 mm	A35	76°
V-330	40 mm	3.2 mm	0.4 mm	A25	72°

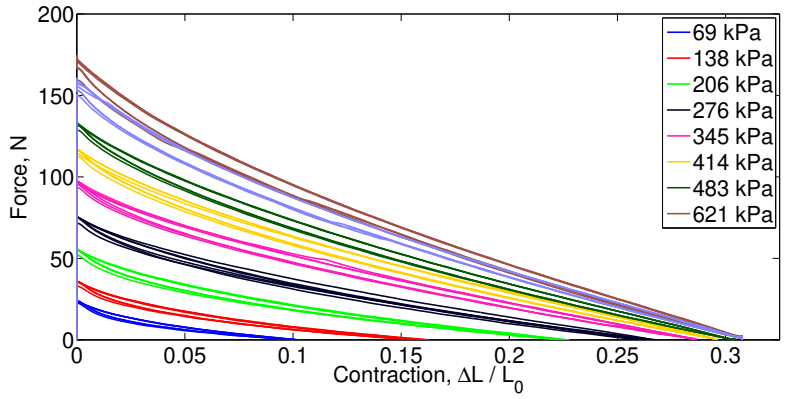

Figure 2.4: Force vs. Contraction PET V-330 PAM

2.3 Experimental Characterization to Study Thickness Effects

Using the same method as described above, a series of V-330 bladders was fabricated to study the effect that bladder wall thickness has on quasi-static PAM performance metrics at the small scale. For consistency with overall size and braid angle, the outer diameter was held constant for all PAMs analyzed in this study by using the same mold. The variation in bladder thickness was introduced by varying the diameter of the steel rod mandrel, which defines the inner diameter of the bladder. Several V-330 PAMs were fabricated and tested with a range of bladder thicknesses

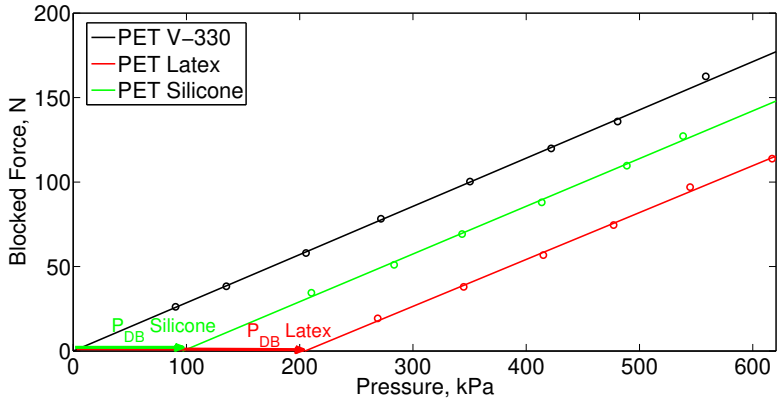

(a) Blocked Force Comparion.

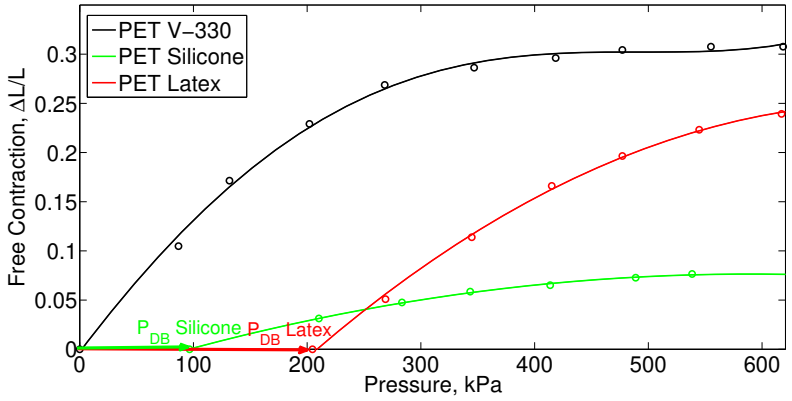

(b) Free Contraction Comparison.

Figure 2.5: Comparison of PAM Performance Metrics from Motivating Study

that varied between 0.4 mm (thin-walled PAM in the initial study) and 0.8 mm (thickness of the latex PAM in the initial study). Experimental measurements of the series of miniature silicone PAMs were compared with the ratio of bladder volume to PAM volume, V_B/V. This volume ratio is directly related to the ratio of bladder wall thickness to outer radius, t/R, by the equation

$$\frac{V_B}{V} = \frac{t}{R}(2 - \frac{t}{R}) \tag{2.1}$$

Table 2.2 lists the active length, bladder thickness, thickness ratio, and volume ratio for the tested miniature PAMs with custom-made silicone bladders. Note that all of the miniature PAMs evaluated have an outer diameter of 3.175 mm. The slight variations in PAM length were due to differences introduced during manufacturing the PAMs, such as the positioning of the bladder on the end fitting and the braid shifting as the end fitting tube was slid into place.

Table 2.2: PAM Properties for Bladder Thickness Study

PAM	Length (mm)	Bladder Thickness (mm)	t/R	V_B/V
a	45.2	0.80	0.500	0.750
b	45.2	0.71	0.448	0.695
c	46.5	0.64	0.400	0.640
d	46.6	0.56	0.352	0.580
e	39.5	0.40	0.250	0.438

Each miniature PAM was tested in the MTS load frame at test pressures ranging from 69 kpa (10 psi) to 621 kPa (90 psi) in increments of 69 kpa (10 psi). Prior to testing, the PAMs were cycled 25 times each at 655 kPa (95 psi) to eliminate the stress-softening behavior, known as the Mullins effect, that is present initially

in the bladder. The stress-softening only increases when the rubber is stretched to new extremes requiring the actuators to be cycled once at a pressure higher than the test pressures [89]. Each test collected force and contraction data during three cycles between blocked force and free contraction. The force-contraction profiles of the tested PAMs are shown in Fig. 2.6. In Fig. 2.6 the steady-state, final, cycle of each test is plotted. To highlight again the importance of bladder material, the force-contraction profiles in Fig. 2.2b and Fig. 2.6a are compared. These PAMs had the same volume ratios, but the former used a latex bladder and the latter a V-330 silicone bladder. In comparing the data, it can be observed that the hysteresis in the V-330 PAM was 50% of the latex PAM. All the V-330 PAMs tested also had lower hysteresis and greater free contractions than the miniature PAMs made from either of the commercially available bladders, 2.3. The hysteresis was computed as

$$\eta = \frac{H_{load} - H_{unload}}{H_{load}} \tag{2.2}$$

where H_{load} is the area under the contraction curve and H_{unload} is the area under the extension curve. The average hysteresis for the bladder thickness study was calculated over the range of 206 kPa to 621 kPa, to cover the test ranges of the two commercial PAMs. The commercial silicone hysteresis was calculated for the pressure range of 206 kPa to 552 kPa, and the latex PAM hysteresis was calculated over the range 276 kPa to 621 kpa. Table 3 summarizes the results of the hysteresis calculations.

To study the effect of bladder thickness, the performance metrics of blocked

Table 2.3: Average Hysteresis

V_B/V	0.750	0.695	0.64	0.580	0.438	Silicone	Latex
η	-0.141	-0.131	-0.108	-0.126	-0.146	-0.238	-0.271

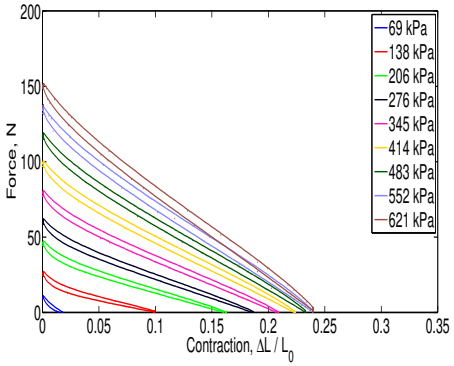

(a) $V_B/V = 0.75$.

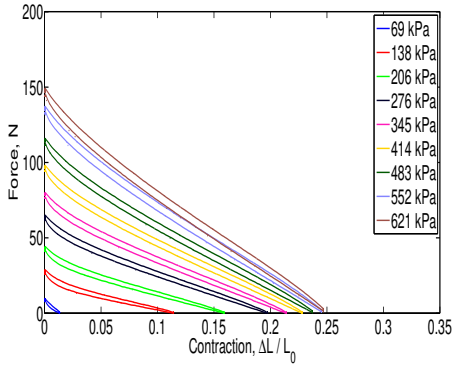

(b) $V_B/V = 0.695$.

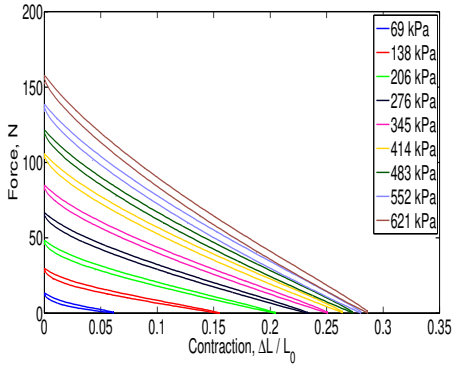

(c) $V_B/V = 0.64$.

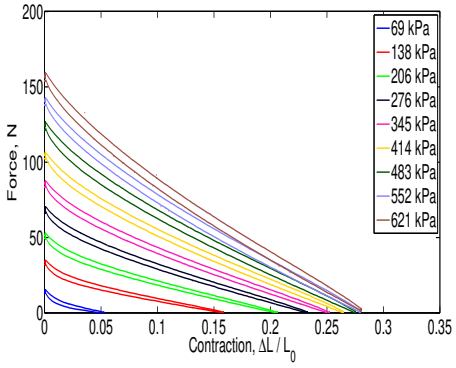

(d) $V_B/V = 0.58$.

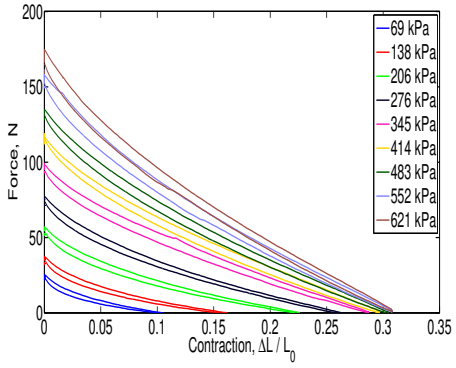

(e) $V_B/V = 0.438$.

Figure 2.6: Force vs. Contraction Test Data for a Number of Discrete Values of Bladder to PAM Volume Ratio

force, free contraction, and dead-band pressure were considered. The PAMs were all similar in length, and it has been shown that active length differences do not affect blocked force, F_B, or contraction, $\Delta L/L$ [87]. Fig. 2.7 shows the blocked force change as a function of corrected pressure

$$P' = P - P_{DB} \tag{2.3}$$

where P is the applied pressure and P_{DB} is the dead-band pressure. Fig. 2.8 shows the free contraction change as a function of pressure for the set of PAMs. Since there are multiple factors affecting the variation of blocked force and free contraction of the PAMs, including braid angle and bladder thickness, the effect of bladder thickness cannot be determined from a set of PAMs that also have braid angle variation. To eliminate the effect of braid angle, a nonlinear stress-strain model was applied and then a parametric study was conducted to compare all the PAMs with the same braid angle. The dead-band pressure, Fig. 2.9, increased with increasing V_B/V, and at lower V_B/V the dead-band pressure was effectively 0 kPa. The solid line represents a linear fit of the measured dead-band pressures with negative dead-band pressures set to zero, highlighting the dead-band pressure becoming a negligible value. The increase in dead-band pressure with increased wall thickness was expected since thicker bladders require higher forces to overcome the bladder elasticity to deform the bladder during the force-contraction cycle. Fig. 2.9 indicates that there are diminishing returns to improvements in dead-band pressure when choosing bladders below a certain volume ratio.

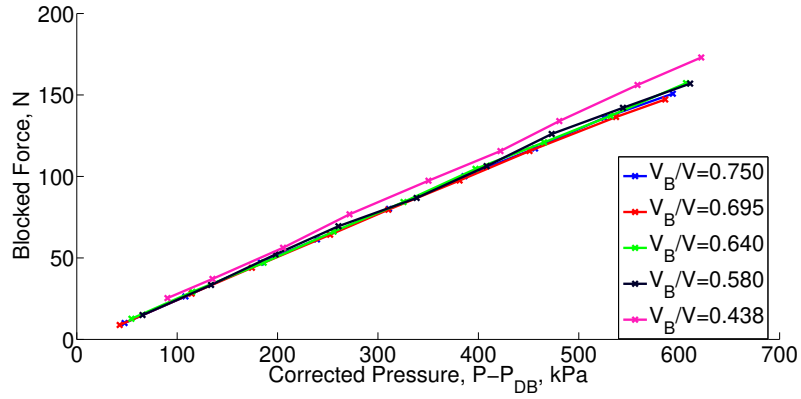

Figure 2.7: Blocked Force Comparison for as built PAMs

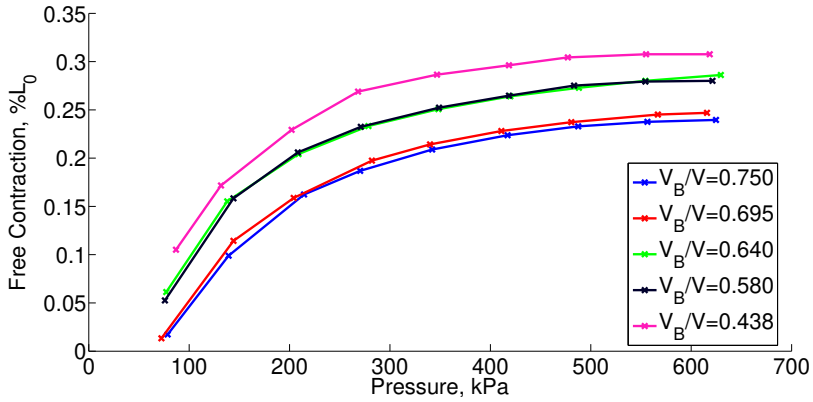

Figure 2.8: Free Contraction Comparison for as built PAMs

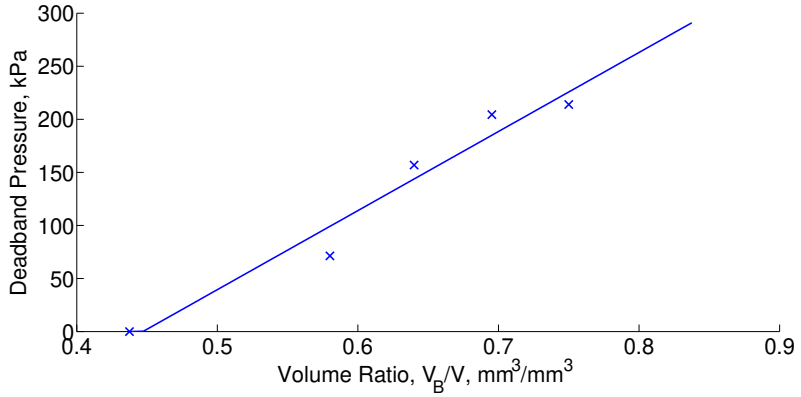

Figure 2.9: Dead-band Pressure Variation vs. Bladder to PAM Volume Ratio

2.4 Modeling

The actuator model used in this study was based on a force balance approach [87] with a nonlinear stress-strain relationship [89]. The nonlinear stress-strain relationship was extended to include a linear variation in pressure. Additionally non-linear stress-strain relationships which included higher polynomials without the lower order polynomials were considered to determine the polynomial terms required for modeling. In this model, the force is calculated as

$$F = \frac{P'}{4\pi N^2}\left(3L^2 - B^2\right) + P'\left(\frac{V_B}{L} - \frac{tL^2}{2\pi RN^2}\right) + \sigma_z\frac{V_B}{L} - \sigma_c\frac{tL^2}{2\pi RN^2} \tag{2.4}$$

where V_B is bladder volume, σ_z is axial stress, and σ_c is circumferential stress. The first term of the force balance model, Eq. 2.4, is the Gaylord force. The second pressure term models the effect of non-constant thickness. In the blocked force condition, it is assumed that $\sigma_c = 0$ and $\sigma_z = 0$, so that Eq. 2.4 simplifies to

$$F = \frac{P'}{4\pi N^2}\left(3L_0^2 - B^2\right) + P'\left(\frac{V_B}{L_0} - \frac{t_0L_0^2}{2\pi R_0N^2}\right) \tag{2.5}$$

which is a linear function of pressure where L_0, R_0, and t_0 are the actuator length, actuator radius, and bladder thickness at the resting length. Using the well-known

triangle relationship for B,L, and N [86], we have

$$\begin{aligned} L &= Bsin(\theta) \\ N &= \frac{Bcos(\theta)}{2\pi R} \end{aligned} \tag{2.6}$$

where θ is the braid angle, and bladder volume is

$$V_B = \pi L(R^2 - (R-t)^2) \tag{2.7}$$

The blocked force can then be found as

$$F = P' \left[\pi R_0^2(2tan^2(\theta_0) - 1) + \pi(2R_0t_0 - t_0^2) - 2\pi t_0 R_0 tan^2(\theta_0)\right] \tag{2.8}$$

where θ_0 is the braid angle at resting length.

For the circumferential and axial stresses in the force balance model, the nonlinear stress-strain relationship

$$\sigma = \sum_{i=1}^{n} E_i(P)\epsilon^i \tag{2.9}$$

was chosen with model order given by n. In Eq. 2.9, σ represents either σ_z or σ_c depending on whether the axial or circumferential stress is being calculated. Similarly ϵ represents the corresponding axial or circumferential strain defined as

$$\epsilon_z = \frac{L}{L_0} - 1 \tag{2.10}$$

$$\epsilon_c = \frac{R - \frac{t}{2}}{R_0 - \frac{t_0}{2}} - 1 \tag{2.11}$$

Further, this nonlinear relationship was constrained such that the polynomial coefficients, E_i, were a linear function of pressure. A nearly linear E_i variation with pressure has been shown in previous research [89], so this noted linear variation was added here in the present work as an constraint to improve interpolation ability of the model to untested operating pressures. The linear pressure variation applied to the nonlinear stress-strain relationship is

$$\sigma = \sum_{i=1}^{n} (E_{i_I} + E_{i_S} P)\epsilon^i \tag{2.12}$$

where E_{i_I} is the intercept and E_{i_S} is the slope of the function $E_i(P)$. The slope and intercept terms were constrained such that

$$\begin{aligned} E_{i_S} &\geq 0 \\ E_{i_I} &\geq 0 \end{aligned} \tag{2.13}$$

ensuring the stress is positive for all positive strains and pressures. A curve fitting analysis was applied using braid angle and linear through fifth-order polynomial terms in the stress-strain relationship to predict the force response such that the model error

$$\Delta = \frac{1}{N_P} \sum_{k} \sqrt{\frac{1}{N_i} \sum_{i} \left[(F)_{ki} - (F_{AVG})_{ki} \right]^2} \tag{2.14}$$

was minimized. The error, Δ, is the average of the error at each pressure, which is the

sum of the difference between the predicted force, F, and the average force from the measured data, F_{AVG}, where N_i is the number of points at which the model and data are compared at a given pressure and N_P is the number of test pressures. The braid angle was included in the analysis due to the difficulty of accurately determining the braid angle of a manually fabricated PAM. The model structure was also modified to varied to study the effect of reducing the number of terms by setting certain $E_i = 0$. For example a stress-strain relationship containing only E_1, E_2 and E_5 becomes

$$\sigma = (E_{1_I} + E_{1_S}P)\epsilon^1 + (E_{2_I} + E_{2_S}P)\epsilon^2 + (E_{5_I} + E_{5_S}P)\epsilon^5 \tag{2.15}$$

The total error between the predicted and measured force was summed across the set of PAMs for all combinations of linear through quintic terms. Stress-strain relationships without the linear term are excluded from this analysis due to the large model error. The average error produced by the models was compared to determine which stress-strain relationships produce accurate models without the extra complexity of an increased number of terms. Fig. 2.10 shows that increasing from a linear relationship to a two-term nonlinear relationship provides a significant decrease in average error, but additional nonlinear terms have a lesser effect on the error. Normalized blocked force error

$$\Delta_{F_B} = \frac{1}{N_P} \sum_k \sqrt{\frac{\left[(F_B)_k - max(F_{AVG})_k\right]^2}{max(F_{AVG})_k^2}} \tag{2.16}$$

and free contraction error

$$\Delta_{F_C} = \frac{1}{N_P} \sum_k \sqrt{\frac{\left[(\Delta L_{F=0})_k - max(\Delta L_{meas})_k\right]^2}{max(\Delta L_{meas})_k^2}} \tag{2.17}$$

where F_{B_k} is the predicted block force, $max(F_{AVG})_k$ is the measured blocked force, $\Delta L_{F=0}$ is the predicted free contraction, and $max(\Delta L_{meas})_k$ is the measured free contraction, are also considered for model selection. Using Figs. 2.10, models with a low number of terms and low force, blocked force, and free contraction errors are chosen for further comparison.

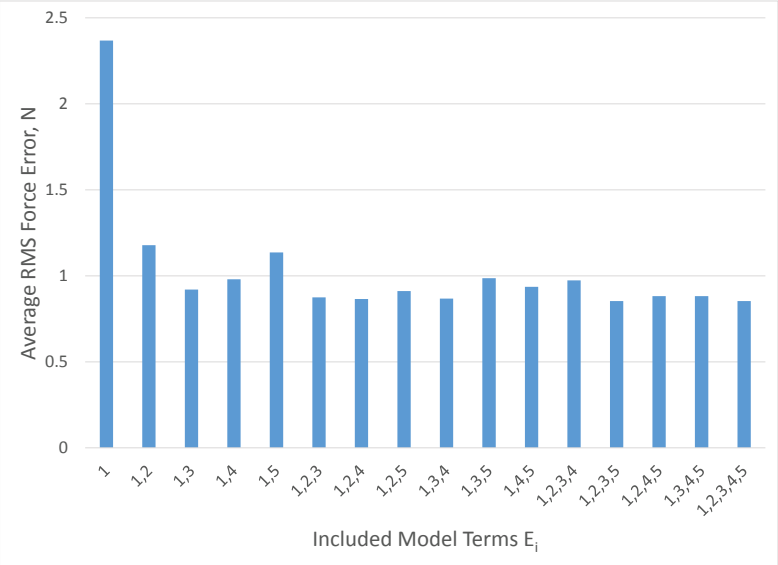

Figure 2.10: Average Force Error

For the E_1&E_3 and E_1&E_4 models, the stress-strain relationships are

$$\sigma = (E_{1_S} P + E_{1_I})\epsilon + (E_{3_S} P + E_{3_I})\epsilon^3 \tag{2.18}$$

$$\sigma = (E_{1_S}P + E_{1_I})\epsilon + (E_{4_S}P + E_{4_I})\epsilon^4 \tag{2.19}$$

These models were compared at each pressure for each PAM in the blocked force, free contraction, and three intermediate contraction conditions. The three intermediate contractions were chosen to represent potential operating contractions at $25\%, 50\%$, and 75% of free contraction. The error at intermediate contractions is

$$\Delta_{IC} = \frac{1}{N_P}\sum_k \sqrt{\frac{\left[(F_{\Delta L=x*F_C})_k - (F_{\Delta L=x*F_C})_{meas})_k\right]^2}{((F_{\Delta L=x*F_C})_{meas})_k^2}} \tag{2.20}$$

where x is the percent of free contraction at which the error is being calculated, in this case either $25\%, 50\%$, or 75%, $F_{\Delta L=x*F_C}$ is the predicted force and $(F_{\Delta L=x*F_C})_{meas}$ is the measured force at the given contraction. The two models provide similar estimates of blocked force, but the second model, $E_1\&E_4$, better predicts free contraction. At the intermediate contractions there are again similar errors in each model. Table 2.4 compares the two models at each of the five conditions, both including the 69 kPa case and excluding it. When excluding the 69 kPa, case the average errors tend to be slightly lower for the first model when considering force errors, but still higher for free contraction. The comparisons of average blocked force and free contraction data, as well as tables of errors for blocked force, free contraction and intermediate contractions can be found in the appendix.

Both models have low error and match well with experimental data. Fig. 2.11 shows the modeling results from the first model. The results from both models

Table 2.4: Average Percent Error

	Model	F_B	25% F_C	50% F_C	75% F_C	F_C
With 69 kPa	E_1 & E_3	2.93	2.93	4.85	9.60	6.60
	E_1 & E_4	2.94	3.02	4.41	9.30	5.54
Without 69 kPa	E_1 & E_3	1.89	1.45	2.43	4.33	3.03
	E_1 & E_4	1.91	1.55	2.38	4.93	2.20

for the slope and intercept of the included E_i and θ_0 are shown in Figure 2.12. Fig. 2.12b shows E_3 and E_4 have a slight increase in intercept with increasing V_B/V . Fig. 2.12c shows E_3 and E_4 have a nearly constant pressure dependence or slope. For E_1 the pressure dependence has a minimal variation with increasing bladder thickness, while the intercept decreases with bladder thickness. For both models the trends are similar with the E_1 intercept being nearly identical. The higher slope and intercept of E_3 compared to E_4 results from the weaker nature of ϵ^3 instead of ϵ^4. Comparing the stress-strain relationship at two pressures in Fig. 2.13 shows the stress for both models is very similar, as is expected due to the small difference in average errors.

2.4.1 Results of Parametric Study

The nonlinear stress-strain modeling results were used to evaluate the model with a common braid angle and length for all PAMs. A braid angle of 72.8° was chosen since it is near the mean of the braid angles determined by the model. This allows the resulting blocked force and free contraction information to be used to evaluate the effect of bladder thickness on the remaining performance metrics. The results in Fig. 2.14 show that blocked force decreases with increasing volume ratio. Eq. 2.8 shows the blocked force is a linear function of pressure with a slope

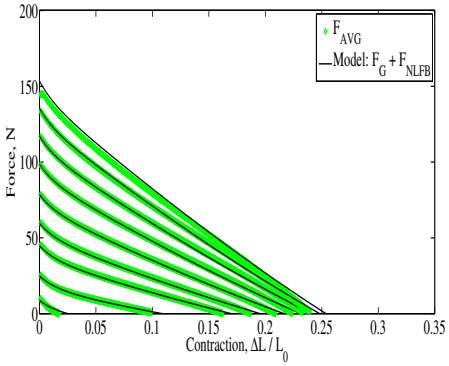

(a) $V_B/V = 0.75$.

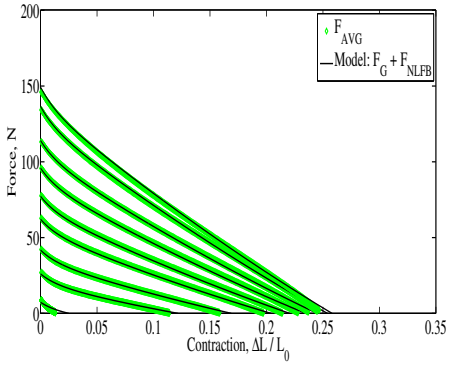

(b) $V_B/V = 0.695$.

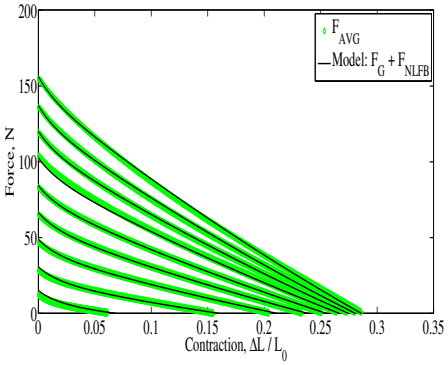

(c) $V_B/V = 0.64$.

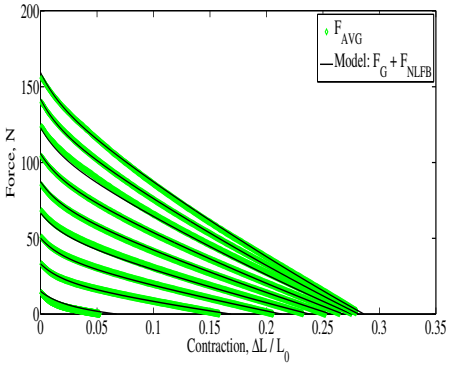

(d) $V_B/V = 0.58$.

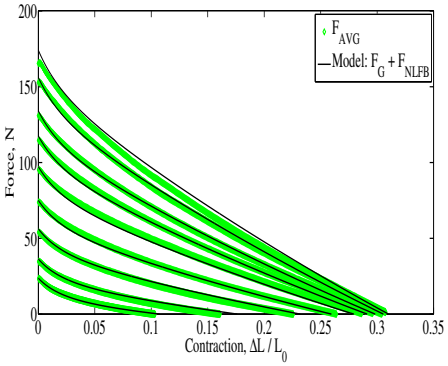

(e) $V_B/V = 0.438$.

Figure 2.11: PAM Polynomial Modeling Results for a Number of Discrete Values of Bladder to PAM Volume Ratio

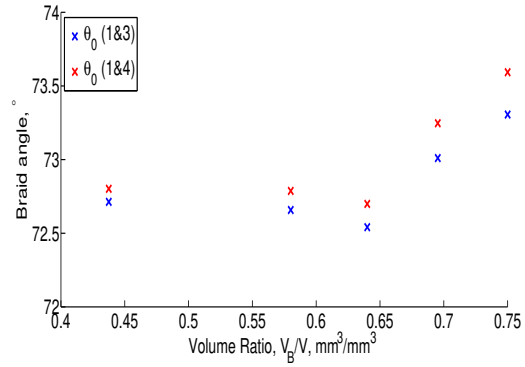

(a) Braid Angle Variation

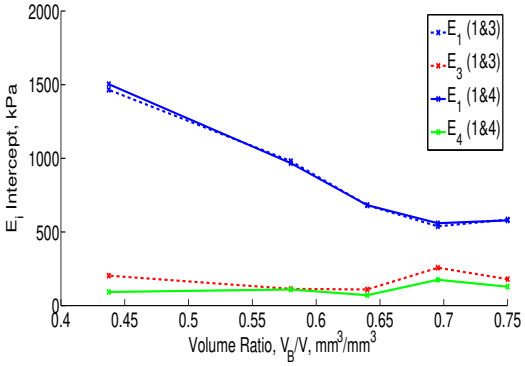

(b) Intercept Variation

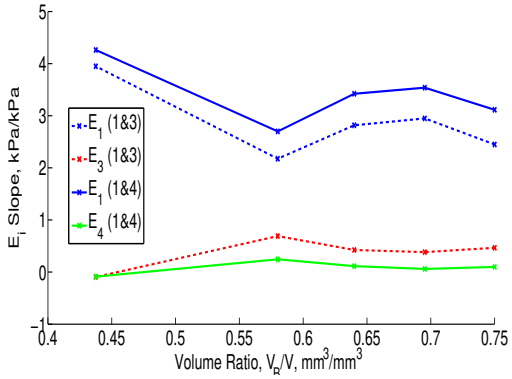

(c) Slope Variation

Figure 2.12: Dependence of Identified Model Parameters on Bladder to PAM Volume Ratio

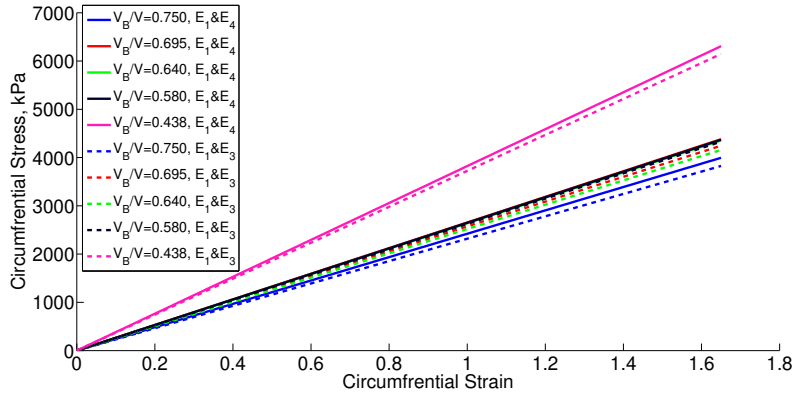

(a) 531 kPa.

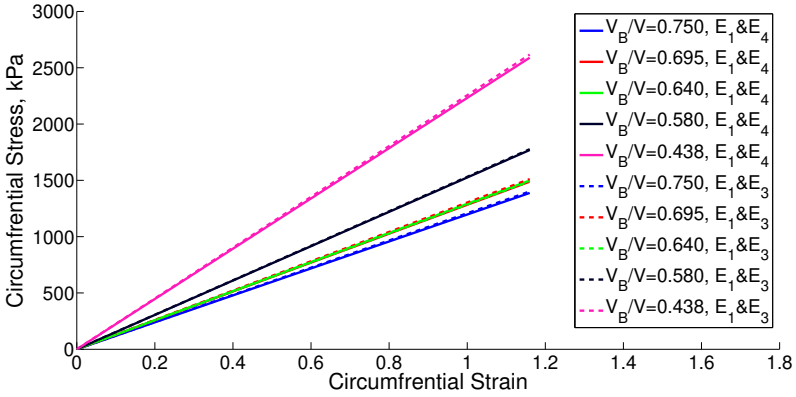

(b) 152 kPa.

Figure 2.13: Stress-Strain Relationship at Various Pressures

determined by the actuator radius, bladder thickness, and braid angle as shown in Fig. 2.14. The same trend is shown in model Fig. 2.15 for free contraction.

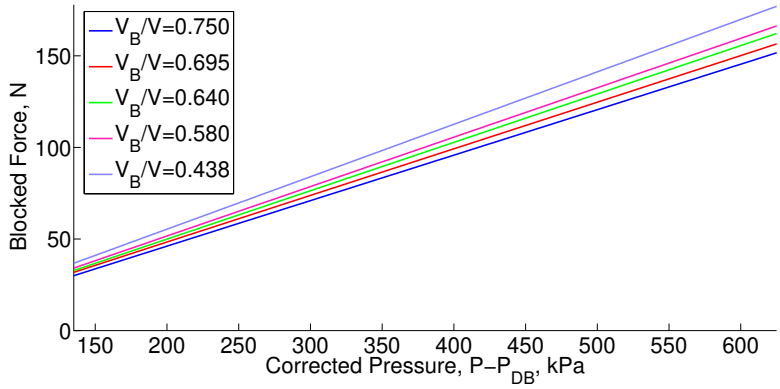

Figure 2.14: Bladder Thickness Effect on Blocked Force with 72.8° braid angle

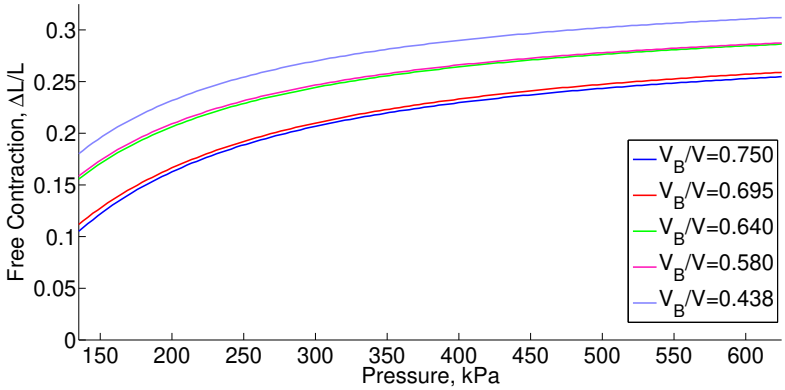

Figure 2.15: Bladder Thickness Effect on Free Contraction with 72.8° braid angle

2.5 Conclusions

Miniature PAMs with different bladder materials and thicknesses were constructed and experimentally characterized. Commercially available bladders at this scale did not produce PAMs with the desired performance, so customized V-330 bladders were fabricated in-house. These customized silicone bladders were devised

with low stiffness and the resulting PAMs were shown to produce comparable blocked forces while achieving greater free contraction ratios at lower pressures. Because of this observed dependence of PAM performance on bladder material, the effect of varying bladder thickness for a given outer diameter was studied. With increasing bladder volume, the dead-band pressure increased. The PAMs were modeled using the force balance approach with a nonlinear stress-strain relationship, with a newly added constraint that the terms vary linearly with pressure to improve interpolation ability. A study was conducted on the number and order of polynomial terms required in the model to match the measured stress-strain relationship, and it was determined that a linear term was necessary, in addition to a single nonlinear term (third or fourth order). The model parameters, including the variation with pressure, were calculated via optimization for the two different nonlinear stress-strain relationships. Using the models, a parametric study was conducted correcting for variations in braid angle between the constructed PAMs. This study verified analytically that blocked force and free contraction both decrease with increasing bladder thickness. For designing miniature PAMs, the highest free contraction and lowest dead-band pressure are obtained with the thinnest bladders. In practical applications the thickness will be limited by manufacturing repeatability and bladder endurance.

Chapter 3: Comparison of Contractile and Extensile Pneumatic Artificial Muscles[1]

3.1 Introduction

Contractile pneumatic artificial muscles (PAMs) are known for the high power to weight ratio, controllable compliance, and simple design. Contractile PAMs have been studied for prosthetic and robotic applications since the 1960's [84]. Applications of contractile PAMs include robotic arms [99,101,120] and legs [103,125]. Contractile PAMs have higher force outputs than comparably sized pneumatic cylinders, so that contractile PAMs have been modified into a Push-PAM configuration, which is a PAM and pneumatic cylinder hybrid, allowing a contractile PAM to generate extension [107]. The resting braid angle of the PAM determines the direction of motion when pressurized. When the braid angle is measured from a plane perpendicular to the length axis of the PAMs, PAMs contract for braid angles above 35.26° and extend for braid angles below 35.26° [57]. In addition to contraction and extension, a non-symmetric family of braid angles can generate various motions [81], including coupled contraction-torsion [126].

[1]Pillsbury, T.E., Wereley, N.M. and Guan, Q., 2017. Comparison of contractile and extensile pneumatic artificial muscles. Smart Materials and Structures, 26(9), p.095034.

Extensile PAMs are being utilized in the field of continuum robotics [29, 51]. The large stroke of extensile PAMs allows for large orientation changes in continuum robots. Maximum extension exceeding 80% at test pressures have been reported in literature [49, 93].

There are a number of modeling techniques used to capture the force-stroke behavior of contractile PAMs [86, 87, 91]. To improve these models, modifications to the bladder model, such as hyperelastic material models [118] and non-linear stress strain models [89], have been used. Extensile PAMs have been modeled to reproduce the maximum extension curve and estimate actuation force [49, 56]. With the recent interest in continuum robotics, both extensile, [29, 51], and contractile PAMs, [48], are being used in similar capacities. As this area continues to gain interest, the choice of when to use extensile or contractile muscles will need to be assessed based on required force and stroke, as well as applicability in a range of applications in a manipulator or robot.

In this work contractile and extensile PAMs are fabricated, tested, modeled, and compared. An existing semi-empirical force balance model [127] for contractile PAMs is extended to extensile PAMs. The results from this semi-empirical model is used to conduct a parametric study to compare extensile and contractile PAMs across a representative range of pressures and range of braid angles. Comparisons include blocked force, stroke, cycle work and efficiency, work and stroke under known loads at a representative braid angle for a range of pressures, as well as blocked force, stroke, cycle work and efficiency at a representative pressure for a range of braid angles.

3.2 Experimental Characterization of Pneumatic Artificial Muscles

Two extensile PAMs and two contractile PAMs were fabricated and quasi-statically tested to model and compare their properties. Both types of PAMs consist of an elastomeric bladder constrained by a braided sleeve and connected by end fittings. When pressurized the bladder expands, but the expansion is constrained by the braided sleeve. For contractile PAMs the constrained bladder radially expands generating an axial shortening and compressive force, while for extensile PAMs the constrained bladder radially contracts generating an axial elongation and tensile force. All PAMs were built with latex bladders and polyethylene terephthalate (PET) braids. The larger extensile PAM and the larger contractile PAM both have an outer diameter of 2.5 cm (1 in). All the PAMs were tested quasi-statically between blocked force and free stroke. Blocked force is the force the PAM produces when constrained to its initial length, and free stroke is the point where the PAM no longer produces force at a given pressure. The small contractile PAM is shown pressurized at its initial length, blocked force, in Fig. 3.1a and free stroke in Fig. 3.1b.

The small contractile PAM was sized using the Gaylord force model, Eq. 3.1,

$$F_B = \frac{P\pi D_0^2}{4\cos^2\theta_0}\left(3\sin^2\theta_0 - 1\right) \tag{3.1}$$

where F_B is the blocked force, P is the pressure, D_0 is the resting PAM outer diameter, and θ_0 is the resting braid angle. The blocked force of a PAM is highly dependent on braid angle for contractile PAMs as shown in Fig. 3.2 which shows the effect of braid

(a) Block Force (Zero contraction).

(b) Free Contraction (Zero force).

Figure 3.1: MTS Testing of Miniature Contractile PAM

angle on the force output for a given pressure and diameter. The Gaylord model was developed for contractile PAMs, so positive forces indicate compression and negative indicates tension. This model will over predict free contraction, but is useful for determining the blocked force of a potential PAM. The smaller contractile PAM was chosen to have an outer diameter, 1 cm (0.4 in), and braid angle which attempted to match the blocked force of the large extensile PAM. The smaller extensile PAM was chosen to use the same bladder as the small contractile PAM. To achieve the braid angle necessary for an extensile PAM excess braid was pushed on during fabrication creating a gap between the bladder and braid at rest. Due to the limited PET braid and latex tubing availability, these two PAMs used a 0.64 cm (0.25 in) diameter bladder. For the model described in the next section, the bladder thickness of these two PAMs is adjusted to account for the inflation of the bladder due to the initial

difference between the bladder outer diameter and PAM outer diameter. The four fabricated muscles are pictured in Fig. 3.3 and the properties are listed in Table 3.1. The PAMs have differing lengths, but length changes have been shown to not affect blocked force or free contraction percent [87].

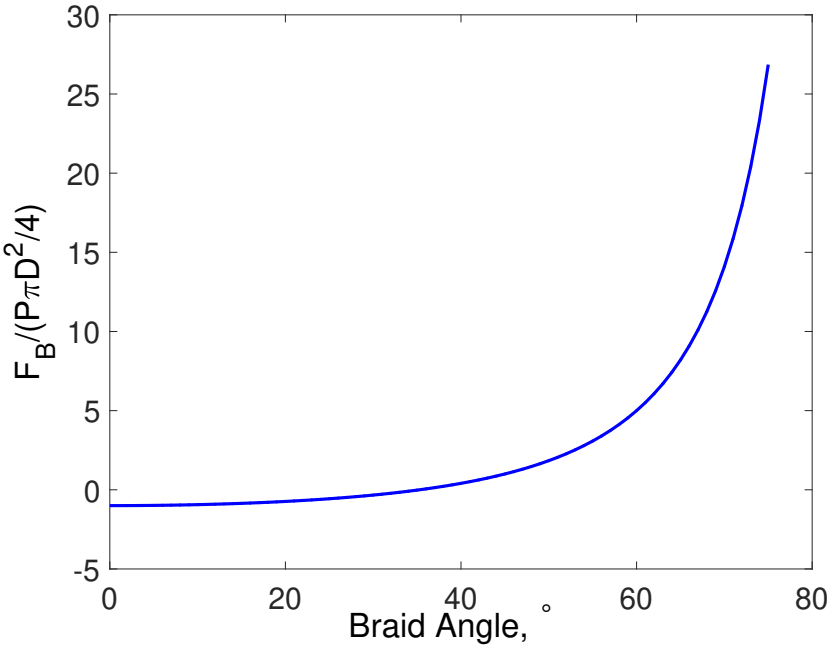

Figure 3.2: Effect of resting braid angle on blocked force output.

Table 3.1: PAM Material Properties

PAM	Diameter	Bladder thickness	Braid angle	Length
Small Extensile	0.85 cm	0.16 cm (0.10 cm*)	25.0°	20 cm
Large Contractile	2.5 cm	0.32 cm	67°	20 cm
Large Extensile	2.5 cm	0.32 cm	13.5°	19 cm
Small Contractile	1 cm	0.16 cm (0.081 cm*)	67°	27 cm

*thickness after initial bladder expansion

The PAM testing was conducted on a MTS machine between 552 kPa (80 psi) and 206 kPa (30 psi) in increments of 69 kPa (10 psi). Each test consisted of three cycles starting from the blocked force condition reaching free stroke then

Figure 3.3: Pneumatic Artificial Muscles. Left to Right: Small Extensile, Large Extensile, Large Contractile, Small Contractile

Figure 3.4: MTS Testing of Extensile PAM

returning to the blocked force condition. Due to the tendency of extensile PAMs to buckle, the PAM was placed inside of a telescopic clear plastic tube to constrain the out of plane deflections during testing, Fig. 3.4. The force-stroke curves recorded during the quasi-static testing are presented in Fig. 3.5. The fabricated contractile PAMs both achieved approximately 24% free stroke, slightly more than half that of the large extensile PAM. The large contractile PAM produced nearly an order of magnitude higher blocked force when compared to the large extensile PAM. The small contractile PAM produced up to 50 N blocked force more than the extensile PAMs after overcoming its higher dead-band pressure. The higher braid angle of the small extensile PAM (close to the limit of 35.26°) results in length changes, 20% initial length, more similar to the contractile PAMs.

3.3 Modeling of Pneumatic Artificial Muscles

The modeling of contractile PAMs has been well covered in literature with both force balance and energy methods [91]. Refinements of these models have utilized hyperelastic, Mooney-Rivlin, bladder model [118] and non-linear stress-strain bladder models [89]. Other modeled effects are non-constant bladder thickness, non cylindrical tip shape, and friction [87]. For this work a linear-cubic stress-strain relationship is used to model the latex bladders [127]. From Kothera *et al.*, the force balance model is

$$F = \frac{P'}{4\pi N^2}\left(3L^2 - B^2\right) + \sigma_z \frac{V_B}{L} - \sigma_c \frac{tL^2}{2\pi R N^2} \tag{3.2}$$

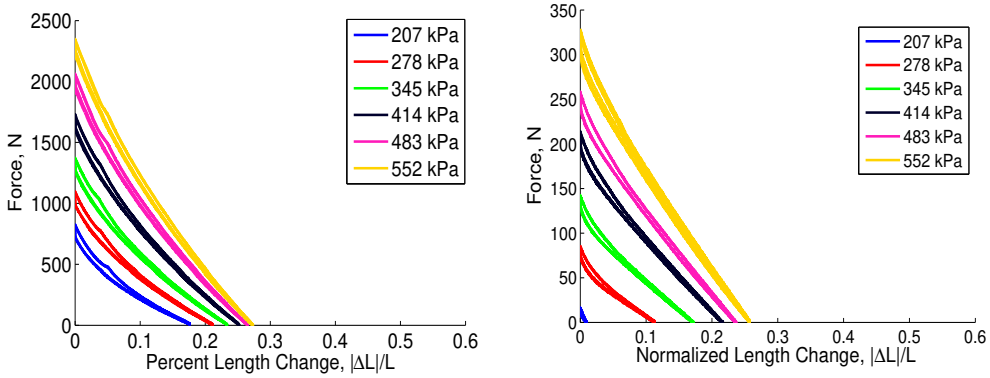

(a) Contractile PAM 2.5 cm

(b) Contractile PAM 1 cm

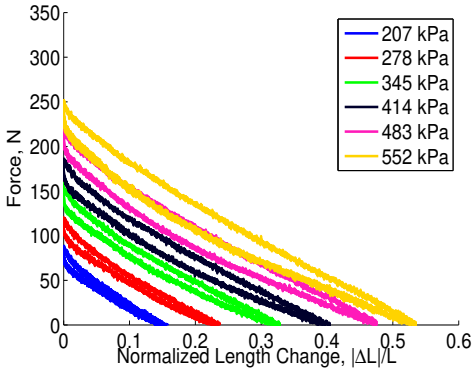

(c) Extensile PAM 2.5 cm

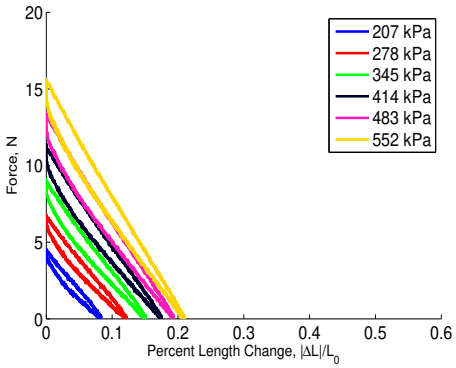

(d) Extensile PAM 0.85 cm

Figure 3.5: PAM MTS Testing Data. Note the difference in scale between extensile and contractile PAMs at each size.

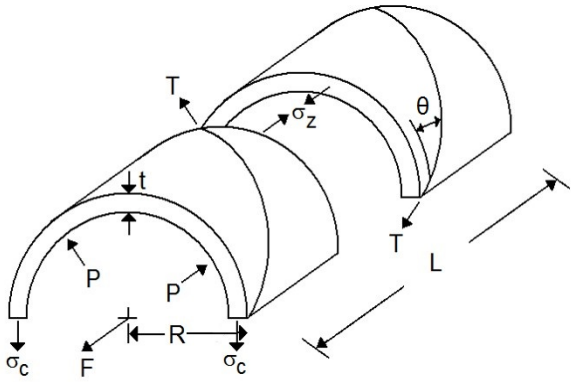

Figure 3.6: PAM parameters and forces. Adapted from [128]

where V_B is bladder volume, σ_z is axial stress, σ_c is circumferential stress, N is the number of turns the braid makes, and B is the braid length [87]. P' is the corrected pressure which accounts for the resting stiffness of the bladder [89]. The first term of the force balance model, Eq. 2.4, is the Gaylord force, Eq. 3.1. The PAM parameters and forces in the model are shown in Fig. 3.6.

The stress-strain relationship used is

$$\sigma = E_1(P)\epsilon + E_3(P)\epsilon^3 \tag{3.3}$$

where E_1 and E_3 are linear functions of pressure that relate strain, ϵ, to stress, σ. This relationship applies to both the circumferential, ϵ_c, and axial, ϵ_z, strains. For a PAM the resulting strains are

$$\epsilon_z = \frac{L}{L_0} - 1 \tag{3.4}$$

$$\epsilon_c = \frac{R - \frac{t}{2}}{R_0 - \frac{t_0}{2}} - 1 \tag{3.5}$$

where L is the length of the PAM, R is the PAM radius, t is the bladder thickness, and the subscript 0 represents the initial values. The circumferential strain is defined from the centerline of the bladder. As described in the previous section and detailed in Table 3.1, the initial bladder thickness, t_0, of the smaller PAMs was adjusted to account for initial inflation prior to the bladder contacting the braid. The slope and intercept values of $E_1(P)$ and $E_3(P)$ are then determined using an fmincon optimization to minimize the difference between the average force error of

all pressures for the quasi-static test data of a PAM. Error was calculated as the difference between F_{avg} and the modeled force as detailed in Pillsbury, Kothera, and Wereley [127].

The force balance model used for contractile PAMs makes no assumption of the PAM motion, and therefore is applied for extensile PAMs. As in Fig. 3.2, the force balance model outputs negative forces when used to model extensile PAMs indicating motion and force opposite that of contractile PAMs. The modeling results are shown in Fig. 3.7.

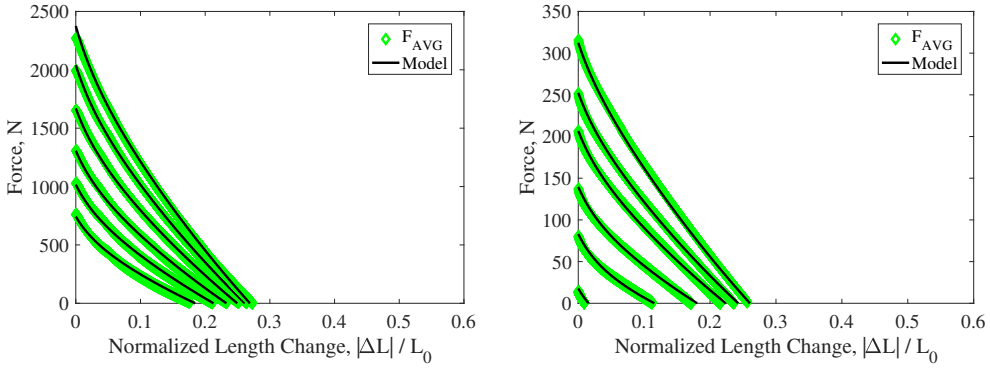

(a) Contractile PAM 2.5 cm

(b) Contractile PAM 1 cm

(c) Extensile PAM 2.5 cm

(d) Extensile PAM 0.85 cm

Figure 3.7: PAM Force Balance Models. Note the difference in scales for extensile and contractile PAMs at each size.

The modeling matches the experimental well and produces small normalized

errors, Table 3.2. The average error at each pressure was normalized by the blocked force at that pressure. The error excluding 207 kPa test case is included due to the large effect normalizing the near zero force levels of the small contractile PAM has on the average error. Table 3.2 also includes the values of the slope and intercept, E_{iS} and E_{iI}, determined from the optimization of each PAM.

Table 3.2: Modeling Results: Error and Bladder Properties

PAM	Extensile 0.85 cm	Extensile 2.5 cm	Contractile 2.5 cm	Contractile 1 cm
$Error, \%$	1.93* (3.12)	2.43 (2.10*)	1.00 (0.80*)	1.51* (6.32)
$E_{1S}, kPa/kPa$	0.607	0.0054	1.46	0.0097
E_{1I}, kPa	1310	2190	485	1305
$E_{3S}, kPa/kPa$	0.780	0.0062	0.0076	1.12
E_{3I}, kPa	326	2.61	408	602

*excluding 207 kPa due to low force level in small PAMs

3.4 Parametric Comparisons of Contractile and Extensile Pneumatic Artificial Muscles

The following section is divided into two parametric studies. The first study, in Section 3.4.1, accounts for the physical differences obtained in the experimental study and motivates the comparisons used in Section 3.4.3. The second study considers the effect of different initial braid angle on PAM performance.

3.4.1 Parametric Study on the Set of Four PAMs

Due to material selection and fabrication the small contractile PAM had a higher blocked force than the extensile PAM. Using the model in Eq. 2.4 the braid

angle of the small contractile PAM was modified to match the blocked force of the extensile PAM. This was achieved by matching the slope of the blocked force as a function of pressure for the small contractile PAM with the slope of the extensile PAM. This braid angle, 61.15°, was then also assigned to the large contractile PAM. The large extensile PAM braid angle was kept at 13.5° and the small extensile PAM was also set to this angle. The results of this blocked force matching are shown in Fig. 3.8. The blocked force is plotted against the corrected pressure, which takes into account the dead-band pressure, or the pressure necessary to overcome the resting stiffness of the bladder. The differences in the lengths of the blocked force versus corrected pressure curves are due to the different dead-band pressures of each PAM. To remove the effect of dead-band pressure on the following results, the dead-band pressure of all PAMs was set to that of the 2.5 cm contractile PAM, 75.85 kpa (11 psi).

Using this set of PAMs with the above braid properties, the bladder properties found during the modeling, and the initial lengths of 19 cm (7.5 in), the differences between the contractile and extensile PAM cycle work, maximum internal volume, cycle work density, and cycle efficiency were considered. The PAM work was calculated as the area under the force-stroke curve at a constant pressure. The cycle work is presented in Fig. 3.9. The 2.5 cm contractile PAM provides the most work due to the large blocked force, nearly 1400 N at 556 kpa, while the large extensile PAM produces more work than the miniature contractile PAM since they have the same blocked forces, as detailed above in the set up, while the larger extensile PAM has a greater free stroke. Having the lowest blocked force, 30 N, the small extensile

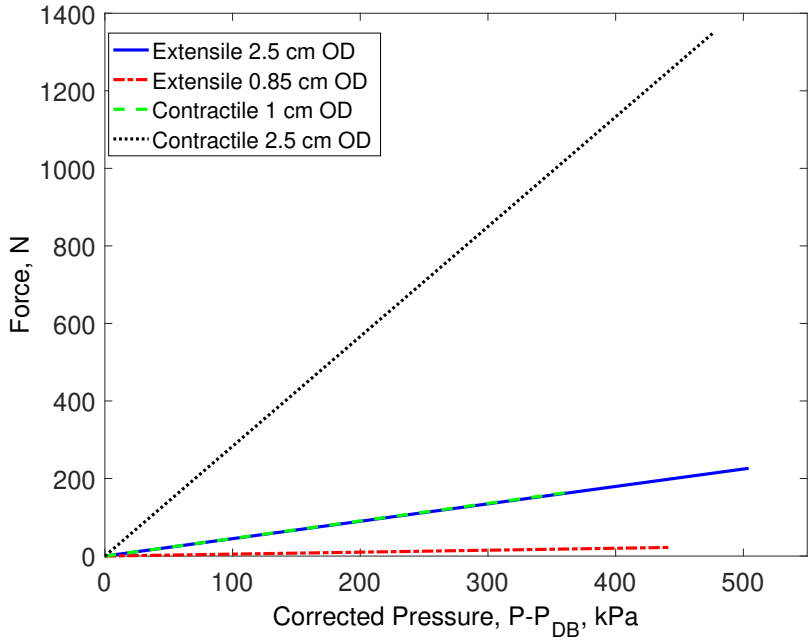

Figure 3.8: Contractile PAM braid angle selection based on blocked force of extensile PAM

PAM produces the least work. Using the relationship between the braid length, PAM length, PAM radius, and bladder thickness Eqs. 3.6-3.10, the internal volume of the PAMs can be calculated.

$$L = B\sin\theta \tag{3.6}$$

$$N = \frac{B\cos\theta}{\pi D} \tag{3.7}$$

$$R = \frac{\sqrt{B^2 - L^2}}{2\pi N} \tag{3.8}$$

$$t = R - \sqrt{R^2 - \frac{V_b}{\pi L}} \tag{3.9}$$

$$V_{int} = L\pi(R-t)^2 \tag{3.10}$$

where B is the braid length, N is the number of turns of the braid, and V_b is the

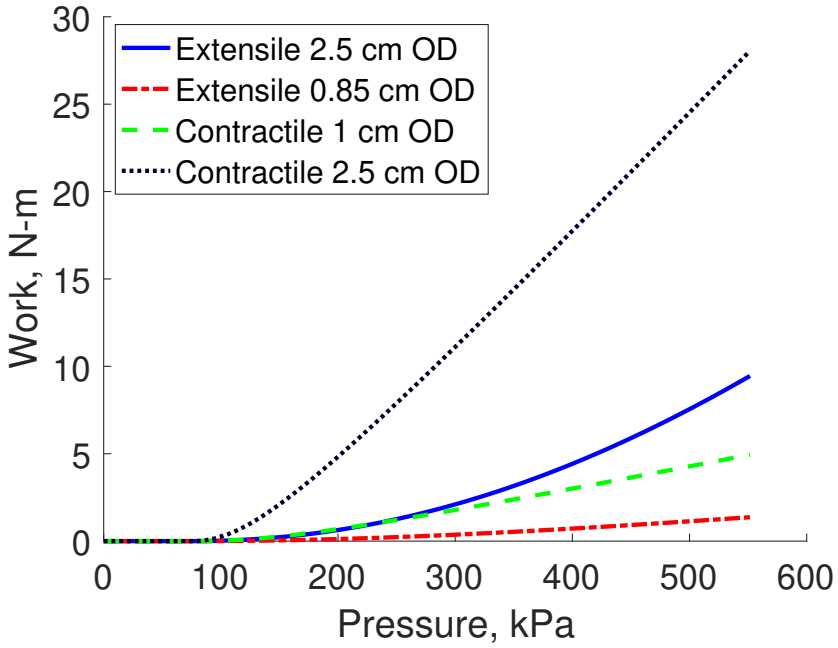

Figure 3.9: Isobaric Actuation Cycle Work.

volume of the bladder. The maximum internal PAM volume is shown in Fig. 3.10. The difference in initial volumes of the two smaller PAMs is due to the different loosenesses of the braid over the bladder.

The efficiency of the actuation cycle and work density can be determined for the set of PAMs. The cycle efficiency is calculated as

$$\eta_c = \frac{W_{out}}{\Delta V P_0 + V_0 \Delta P + \Delta V \Delta P} \tag{3.11}$$

where V_0 is the initial internal PAM volume, ΔV is the change in PAM volume during the full stroke, P_0 is the atmospheric pressure, and ΔP is the test pressure.

The modeled actuation cycle efficiency is presented in Fig. 3.11. The contractile PAMs are more efficient than the extensile PAMs. PAMs of the same type, contractile or extensile, share similar efficiency properties.

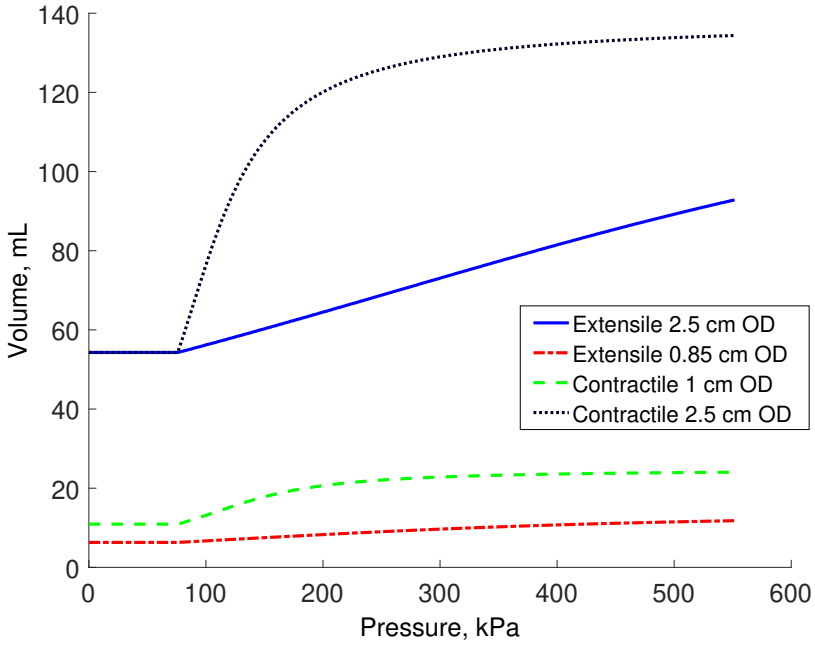

Figure 3.10: Bladder Maximum Internal Volume.

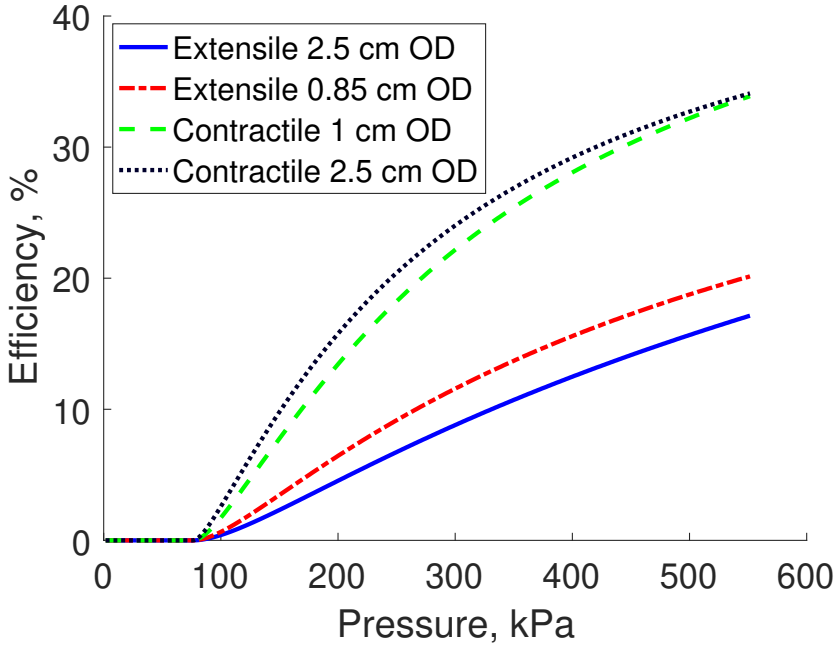

Figure 3.11: Isobaric Actuation Cycle Efficiency

Similar trends are shown for work density Fig. 3.12. The work density is defined as the work, Fig. 3.9, divided by the max volume of the cycle, Fig. 3.10. Contractile PAMs with the same braid angle have nearly identical work densities, and contractile PAMs have a greater work density than extensile PAMs

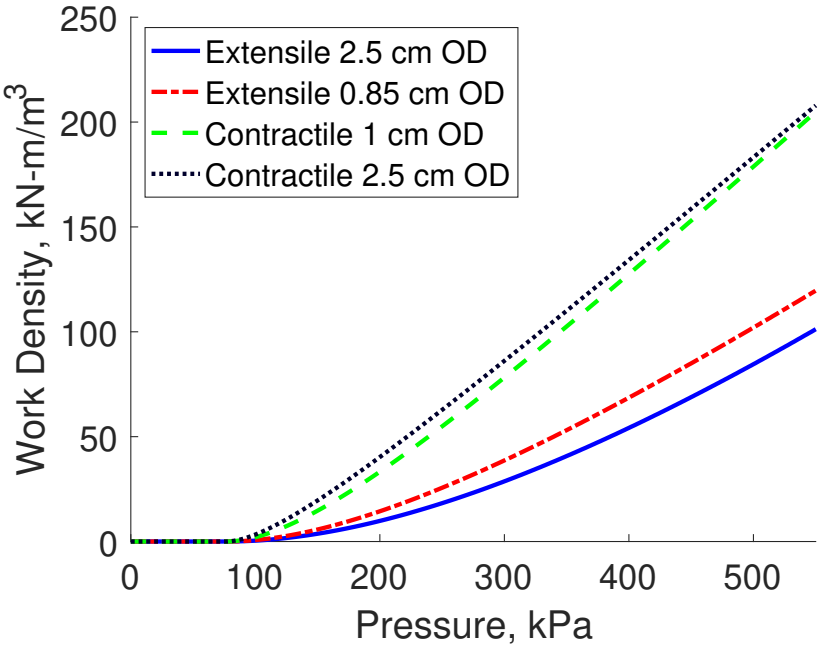

Figure 3.12: Isobaric Actuation Cycle Work Density

To compare the ability of the set of PAMs to move a load, the work and displacement under a known static load are determined. The work under a known load for each PAM is given in Fig. 3.13 and the displacement is given in Fig. 3.14. As with the force-stroke plots, for comparison all values of displacement are positive. The results are as expected with the large contractile PAM producing the most work and the extensile PAMs producing the highest stroke for low loads and high pressures. Note that the large contractile PAM and small extensile PAM, Fig. 3.13, have a different scale for the work contours. The work density results, Fig. 3.15, are similar

to the actuation cycle plot, Fig. 3.12, with the two contractile achieving similar work densities and the extensile PAMs achieving about half of that value. The conclusions drawn from the known load plots, Fig 3.13-3.15, reinforces the results of Fig. 3.13-3.12, therefore the isobaric comparisons will be used in the following parametric studies of diameter and braid angle.

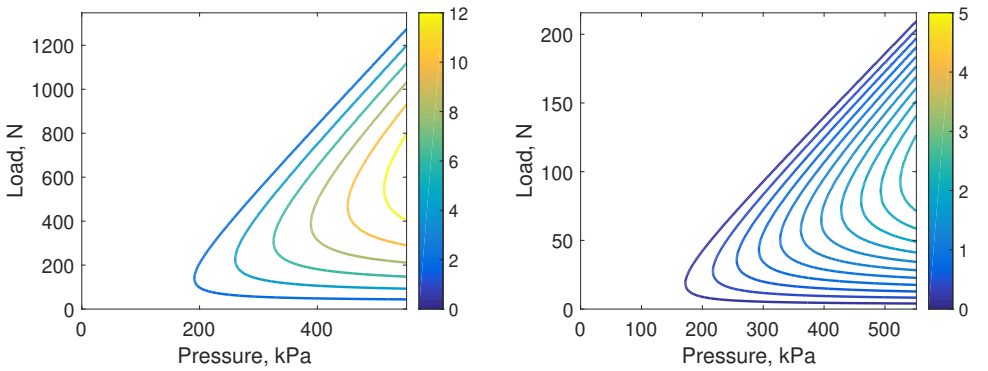

(a) Contractile PAM 2.5 cm

(b) Contractile PAM 1 cm

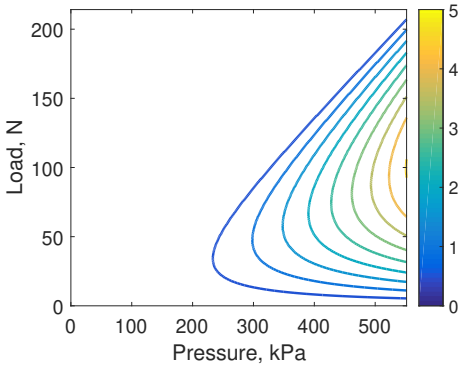

(c) Extensile PAM 2.5 cm

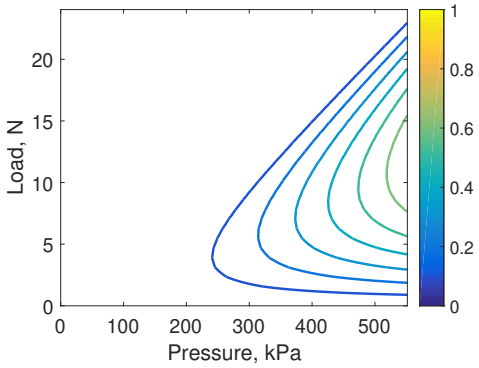

(d) Extensile PAM 0.85 cm

Figure 3.13: PAM work, N-m, for a range of loads and pressures

3.4.2 Parametric study on the effect of diameter

A parametric study of diameter was also considered. For a given PAM diameter, the thickness of the bladder has an effect on PAM properties [127]. Due to

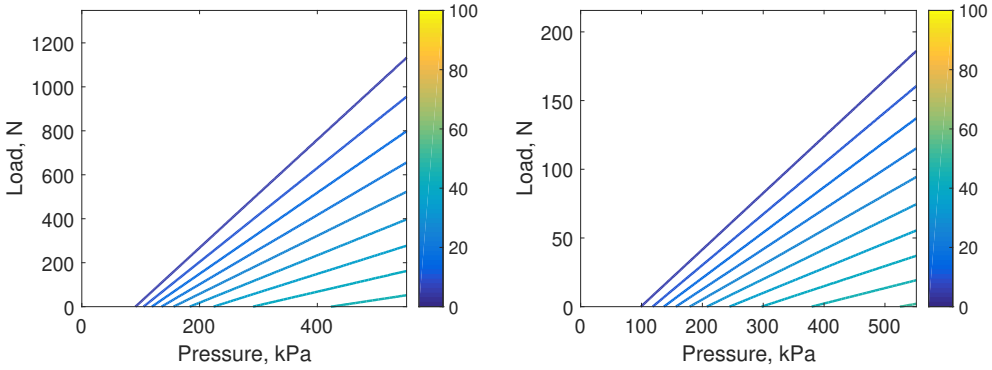

(a) Contractile PAM 2.5 cm

(b) Contractile PAM 1 cm

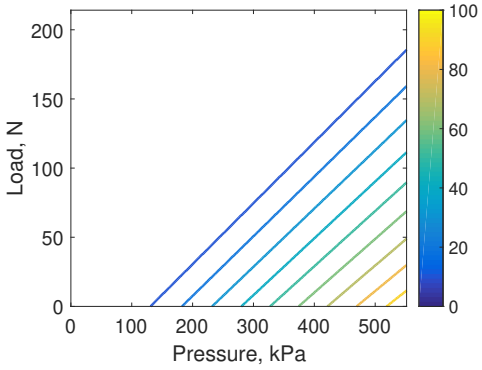

(c) Extensile PAM 2.5 cm

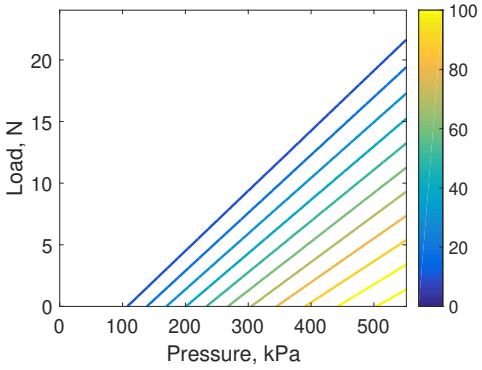

(d) Extensile PAM 0.85 cm

Figure 3.14: PAM stroke, mm, for a range of loads and pressures

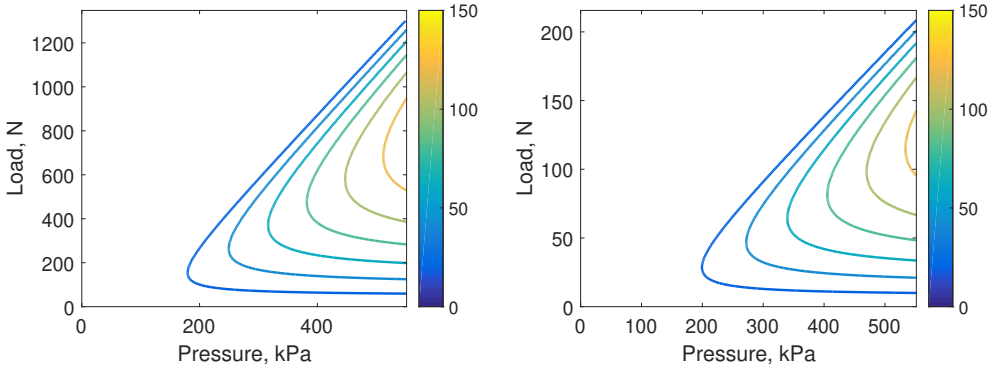

(a) Contractile PAM 2.5 cm

(b) Contractile PAM 1 cm

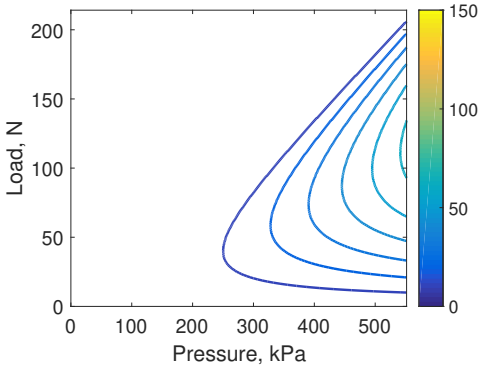

(c) Extensile PAM 2.5 cm

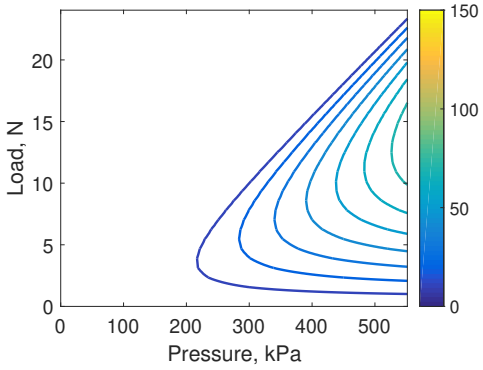

(d) Extensile PAM 0.85 cm

Figure 3.15: PAM work density, kN-m/m^3, for a range of loads and pressures

these thickness effects when varying diameter, the ratio of initial thickness to initial radius, $\frac{t_0}{R_0}$, should be kept constant. It will be shown that this parameter variation causes force to increase proportionally to R_0^2, with no change in free stroke. This relationship is shown in Eqs. 3.12-3.17.

$$R = R_0 \frac{\cos\theta}{\cos\theta_0} \tag{3.12}$$

Equation 3.13 is the equation for bladder volume with R replaced with the relationship in Eq. 3.12.

$$V_B = R_0^2 \left[\frac{\cos^2\theta}{\cos^2\theta_0} \left(L\pi \left(2\frac{t}{R} - \left(\frac{t}{R} \right)^2 \right) \right) \right] \tag{3.13}$$

The force equation with initial diameter effect, Eq. 3.14 was obtained by substituting R (Eq. 3.12), L (Eq. 3.6), N (Eq. 3.7), and V_B (Eq. 3.13) into Eq. 2.4 and separating the R_0^2 term. The terms remaining in brackets in Eq. 3.14 only vary with pressure, L_0, θ_0, $\frac{t_0}{R_0}$, the bladder model, and the current PAM length. Using Eq. 3.6 the current braid angle is a function of the current PAM length.

$$F = R_0^2 \left[\frac{\cos^2\theta}{\cos^2\theta_0} \left(\frac{P'\pi}{\cos^2\theta} \left(3\sin^2\theta - 1 \right) + \sigma_z \pi \left(2\frac{t}{R} - \left(\frac{t}{R} \right)^2 \right) + \sigma_c 2\pi \tan^2\theta \frac{t}{R} \right) \right] \tag{3.14}$$

The above stated dependency is shown for ϵ_c and $\frac{t}{R}$ in Eqs. 3.15 and 3.16. Equation 3.15 is obtained from substituting Eq. 3.6, Eq. 3.12, and Eq. 3.13 into Eq.

3.9.

$$\frac{t}{R} = \left(1 - \sqrt{1 - \frac{\sin\theta_0}{\sin\theta}\frac{\cos^2\theta_0}{\cos^2\theta}\left(2\frac{t_0}{R_0} - \left(\frac{t_0}{R_0}\right)^2\right)}\right) \tag{3.15}$$

Eq. 3.16 is obtained from substituting Eq. 3.12 into Eq. 3.5.

$$\epsilon_c = \frac{\cos^2\theta}{\cos^2\theta_0}\frac{\left(1 - \frac{1}{2}\frac{t}{R}\right)}{\left(1 - \frac{1}{2}\frac{t_0}{R_0}\right)} - 1 \tag{3.16}$$

The internal volume, V_{int}, used for the both the efficiency and work density calculations can be shown to also be dependent on only R_0, θ_0, $\frac{t_0}{R_0}$, and L, by substituting Eq. 3.12 into Eq. 3.10.

$$V_{int} = R_0^2\left[\frac{\cos^2\theta}{\cos^2\theta_0}\left(L\pi\left(1 - \frac{t}{R}\right)^2\right)\right] \tag{3.17}$$

Since both force and volume depend on R_0^2, the other initial PAM properties and bladder model are held constant, and the stroke is controlled and independent of R_0, the efficiency and work density for a PAM with chosen PAM properties, bladder model, and constant $\frac{t_0}{R_0}$, remain constant with variations in R_0.

Custom bladder fabrication would be required to conduct the diameter study. The braid angles achievable from a set of commercial off the shelf components is limited, so to experimentally explore this space a braid winding machine would also be necessary, since the assembled braid angle for a given braid is a function of the PAM diameter. This machine would also be necessary to experimentally validate the parametric braid angle study.

3.4.3 Parametric study on the effect of braid angle

To further compare the difference between extensile and contractile PAMs, the empirically determined bladder model was used to study a range of braid angles. Braid angle was chosen to vary since both braid angle and diameter have both been shown to have a large impact on force or contraction.

The braid angle study takes the single point of the models above and extends these models through a range of braid angles. This analysis is not validated experimentally because precise braid angle variations would require use of a braid winding machine as discussed in 3.4.2.

Blocked force, free stroke, work, and volume all increase from the critical braid angle at 35.25°, Figs. 3.16-3.19. As expected from the blocked force shown in Fig. 3.2, the blocked force of the contractile PAMs greatly increases as the braid angle increases and the blocked force of the extensile PAMs reaches a limit as the angle approaches zero, Fig. 3.16. For free stroke the inverse is true, Fig. 3.17. There is a limit to the stroke of a contractile PAM and an extensile PAM can achieve very large strokes at small braid angles. The work of the contractile PAMs increases with braid angle as the force continues to increase, while the work of the extensile PAMs reaches a limit, Fig. 3.18. The trends for efficiency and work density are similar with similar values near the critical braid angle for both types of PAMs, but with the contractile PAMs reaching higher values as the braid angles become more extreme, Figs. 3.20 and 3.21.

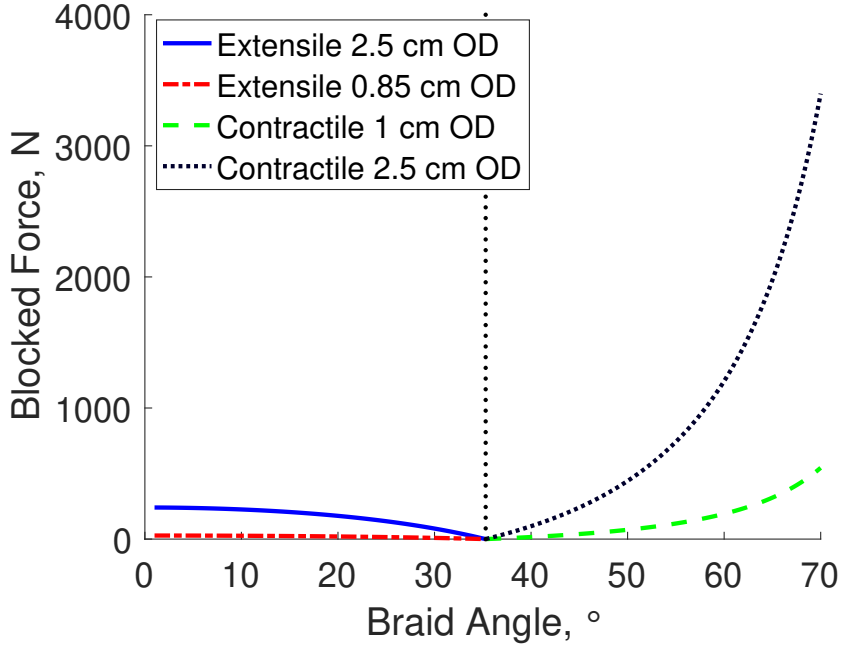

Figure 3.16: Blocked Force.

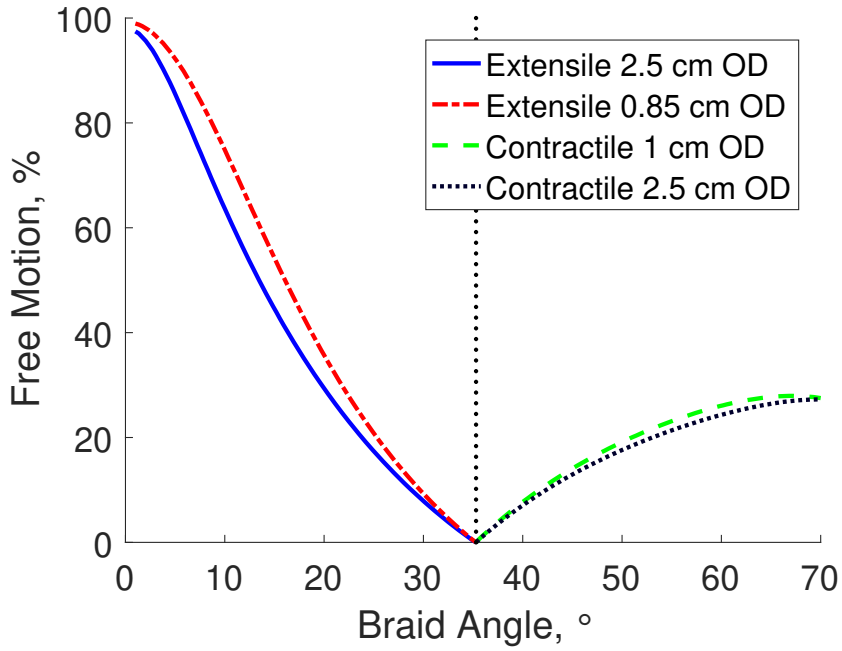

Figure 3.17: Free Stroke.

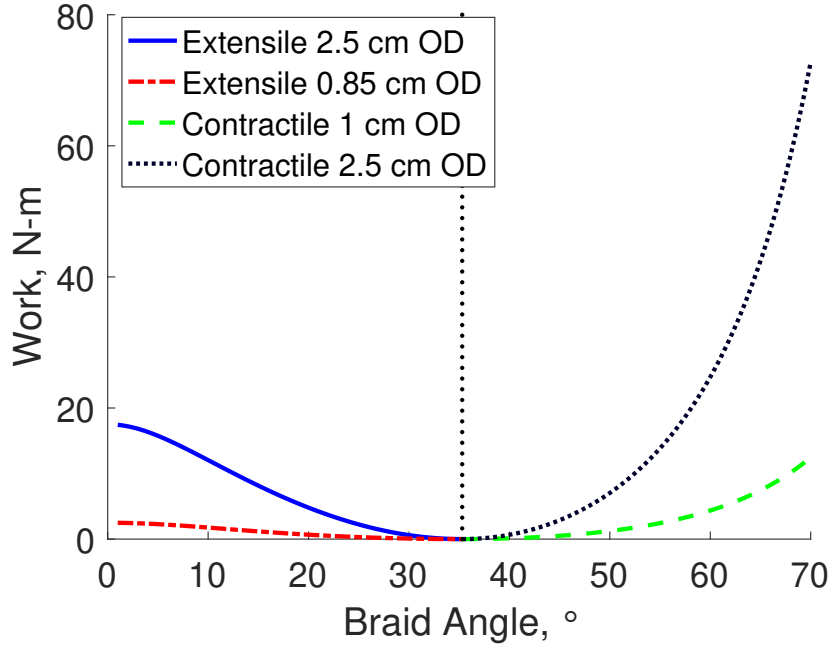

Figure 3.18: Isobaric Actuation Cycle Work.

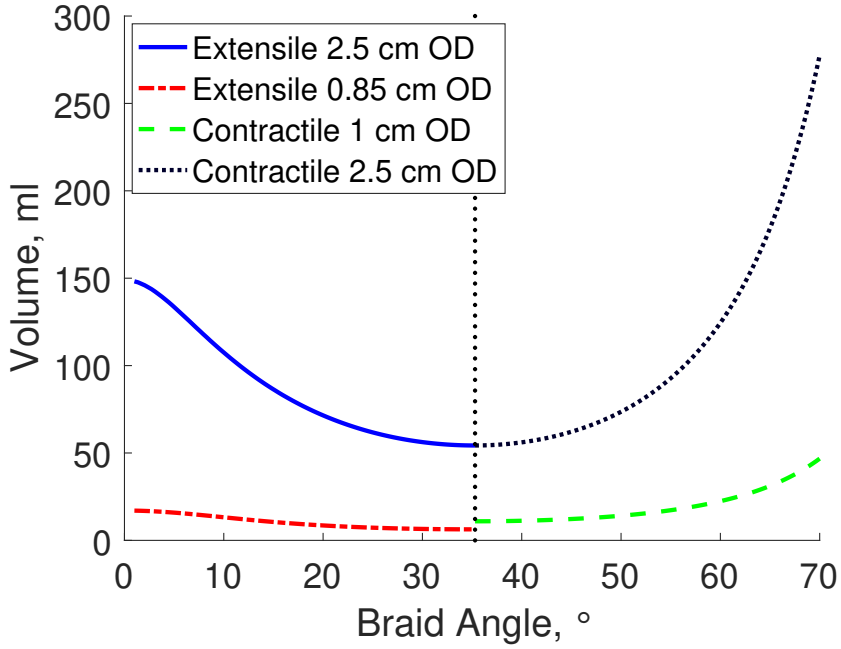

Figure 3.19: Bladder Maximum Internal Volume.

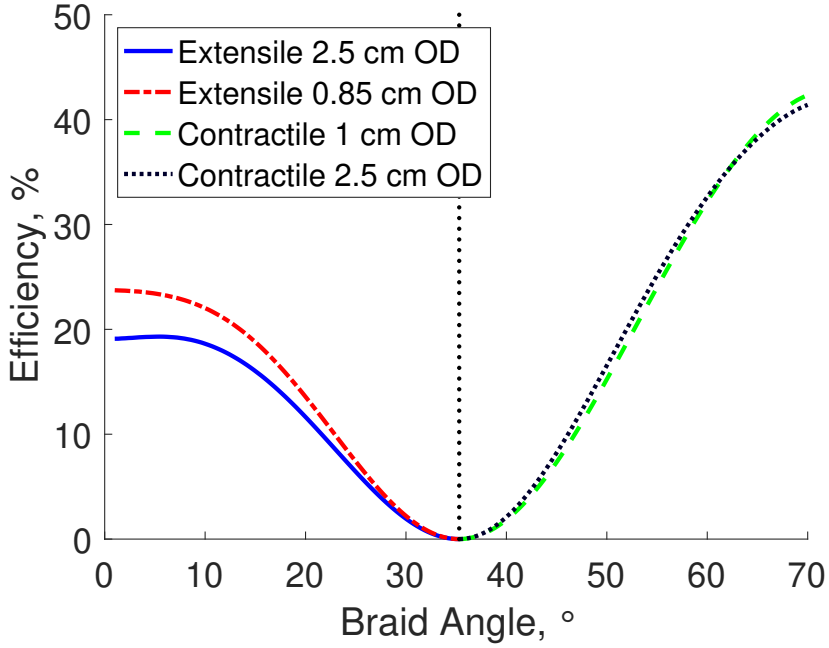

Figure 3.20: Isobaric Actuation Cycle Efficiency

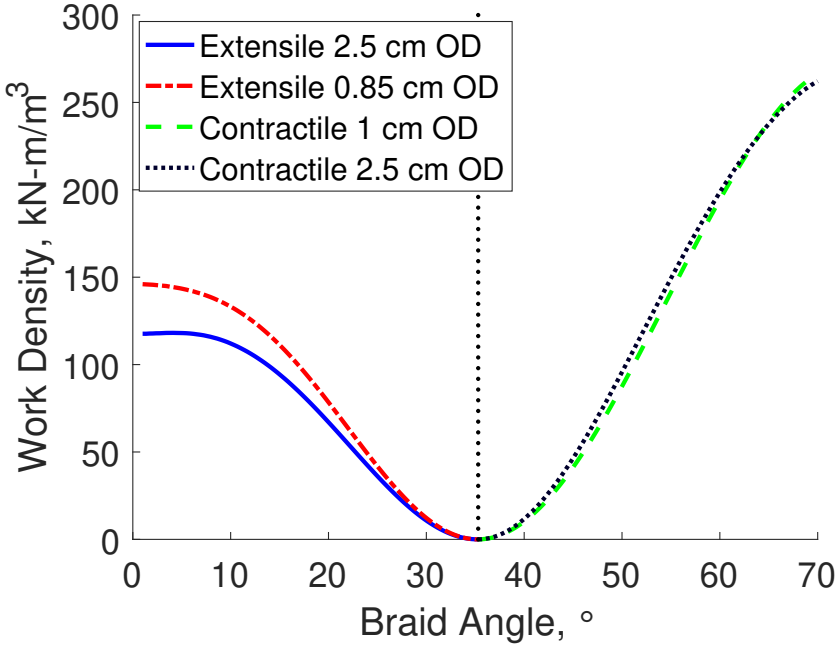

Figure 3.21: Isobaric Actuation Cycle Work Density

3.5 Conclusions

Extensile and contractile PAMs were quasi-statically characterized to evaluate the differences in the force-stroke profiles and to apply PAM force modeling techniques. Current contractile PAM models were shown to be valid for extensile PAM modeling. The PAMs were modeled using a force balance method with a non-linear stress-strain relationship for the bladder model. The unified model can be beneficial to extensile PAMs for situations such as model based control implementation as well as facilitating the design of a continuum robot arm with a combination of extensile and contractile muscles. The resulting non-linear bladder models were then used to parameterize and compare the PAMs. Contractile PAMs with the same initial outer diameter produce more work and are more efficient, but have less stroke than the same size extensile PAMs. The high work output of contractile PAMs make them good candidates in traditional rigid robotics applications. For applications where large strokes, $> 30\%$, are needed extensile PAMs are a good choices provided PAM buckling is avoided. Although, for linear extension a Push-PAM may be a better choice [107], but it could not replace an extensile PAM in continuum robotics applications. When considering work density, contractile PAMs of different scales with the same braid angles and similar materials achieve the same work density, and produce up to twice that of extensile PAMs. The same is true of extensile PAMs at different scales. These results were also demonstrated for PAMs of varying diameters and braid angles. As future work the results of the parametric study on braid angle will be experimentally validated using PAMs fabricated using a braid

winding machine. With a braid winding machine a parametric study on diameter can also be conducted.

Chapter 4: Non-linear quasi-static model of pneumatic artificial muscle actuators[1,2]

4.1 Introduction

The pneumatic artificial muscle (PAM) or McKibben muscle was invented by Joseph L. McKibben and utilized in many current applications [91]. This device originally was intended to motorize an orthotic arm for McKibben's poliomyelitic daughter [84]. A PAM is comprised of an elastomeric bladder, a braided mesh sleeve, and two end fittings. Upon inflation of the bladder by a working fluid (air in this case), the bladder and braid of an contractile PAM expand radially and a contraction force is generated in the axial direction. Daerden and Lefeber conducted a comprehensive review of various types of pneumatic muscles [129].

In order to apply these PAMs to engineering applications, the first step is to characterize their actuation force versus contraction ratio as a function of the inflation pressure. Two main approaches were used such as energy modeling [80,84,85] and the force profile of the surface pressure by determining contractile and radial forces based

[1]Revised version of Wang, G., Wereley, N.M. and Pillsbury, T., 2015. Non-linear quasi-static model of pneumatic artificial muscle actuators. Journal of Intelligent Material Systems and Structures, 26(5), pp.541-553.

[2]The author would like to thank Dr. Gang Wang for developing the analysis of contractile PAMs using a hyperelastic modeling perspective.

on the energy conservation due to applied pressure [130]. Although these methods were conceptually different, a similar force formulation was reached, referred to as the Gaylord model. Although the Gaylord model accurately predicts block force, the Gaylord model fails to completely capture the force-stroke behavior of the PAMs resulting in errors between model predictions and experimental data. To reduce this error Klute and Hannaford included the storage energy of the inner bladder [86] and modeled it as an incompressible Mooney-Rivlin material [131, 132].

Ferraresi *et al.* proposed a force balance approach to determine the axial actuation force [88]. In this approach, the internal stress components of the bladder were calculated based on the thin-walled theory under the assumption of linear elasticity. The axial actuation force can be determined from the force equilibrium. Predicted contraction ratios showed good agreement when the load was low, but the model agreement degraded as load increased.

Kothera *et al.* studied models based on energy conservation and force balance approaches to accurately predict the force-stroke curve for a given pressure. Energy conservation was modified to account for bladder elasticity, braid elasticity, and non-cylindrical bladder tip shapes. In addition, the force balance model was refined to account for non-constant bladder thickness and non-cylindrical bladder tip shapes. These refinements greatly improve model predictions, and the force balance approach more accurately predicts experimental force-stroke measurements. These correction terms improve the model to different degrees for different actuators. However, these correction terms are developed based on the ad hoc approach to account for the contributions from the bladder, braid, and tip shape [87].

Tondu conducted a comprehensive review on existing models of PAMs [91]. Tondu points out in his review that the non-linear relationship between stress and strain in the bladder and the behavior of the braid are key issues to fully understand how the PAM behaves. As concluded, a physical, reasonably simple model for the PAM is expected. Hocking and Wereley introduced a non-linear stress-strain function (fourth-order polynomial) to account for the bladder material non-linearities in the force balance model [89]. This treatment is convenient for engineering analysis; however, the associated material constants are dependent on applied pressure and must be identified using experimental data. Therefore, this class of model does not provide a predictive analysis that accurately predicts actuator performance in advance of testing.

A key goal of this study is to develop an analysis that predicts actuator behavior using only characteristics of the PAM such as bladder and braid geometry and bladder material properties. Typically, finite strain theory must be used to model hyperelastic materials such as those used in rubber or elastomeric bladders. In this work finite strain theory is used to develop the bladder stress-strain relationships to be applied to the force balance model. The developed model is then validated on both contractile and extensile PAMs.

4.2 Nonlinear Quasi-static Modeling of Pneumatic Artificial Muscles

A PAM is composed of an elastomeric bladder, braided mesh sleeve, and two end fittings. In order to develop the non-linear quasi-static model, the following

assumptions are used the bladder is modeled as a thick-walled cylinder, there is no elastic deformation of the braided sleeve, the interaction between the bladder and braid is neglected, and the bladder material is incompressible. The shape of the rubber bladder in its resting and pressurized states can be defined using cylindrical coordinates [133] as follows

$$\begin{aligned} r_0 <= A <= R_0 \\ 0 <= \Phi <= 2\pi \\ 0 <= Z <= L_0 \end{aligned} \tag{4.1}$$

where $(A\Phi Z)$ are cylindrical coordinates,

$$\begin{aligned} r <= a <= R \\ 0 <= \phi <= 2\pi \\ 0 <= z <= L \end{aligned} \tag{4.2}$$

and r is the inner radius of the bladder, R is the outer radius of the bladder, L is the length of the PAM, the subscript 0 indicates the initial values of these parameters, and $(a\Phi Z)$ are the deformed coordinates.

Assuming axisymmetric deformation, the following relations can be made using λ, the axial stretch ratio along the length of the PAM. For the extensile PAMs in this work $\lambda > 1$, and for contractile PAMs the model was developed using $\lambda < 1$.

$$\begin{aligned} \phi &= \Phi \\ z &= \lambda Z \\ L &= \lambda L_0 \end{aligned} \tag{4.3}$$

The deformation gradient, F_D, [134] given by

$$F_D = \begin{bmatrix} \frac{da}{dA} & 0 & 0 \\ 0 & \frac{a}{A} & 0 \\ 0 & 0 & \lambda \end{bmatrix} \tag{4.4}$$

with the following principal stretches

$$\begin{aligned} \lambda_a &= \frac{da}{dA} \\ \lambda_\phi &= \frac{a}{A} \\ \lambda_z &= \lambda \end{aligned} \tag{4.5}$$

and assuming incompressibility leads to a relationship between r and R, where D is a constant.

$$\frac{da}{dA}\frac{a}{A}\lambda = 1 \tag{4.6}$$

$$A^2 = \lambda\left(a^2 - C_r^2\right) \tag{4.7}$$

Also, using the incompressibility condition λ_r can be represented as

$$\lambda_a = \frac{A}{\lambda a} \tag{4.8}$$

The right Cauchy-Green Tensor, C, is given by [134]

$$C = F_D^T F_D = \begin{bmatrix} \left(\frac{A}{\lambda a}\right)^2 & 0 & 0 \\ 0 & \left(\frac{a}{A}\right)^2 & 0 \\ 0 & 0 & \lambda^2 \end{bmatrix} \tag{4.9}$$

The strain invariants, I, necessary for the Mooney-Rivlin [131, 132] strain density function, W, are

$$\begin{aligned} I_1 &= \mathrm{Tr}(C) = \left(\frac{A}{\lambda a}\right)^2 + \left(\frac{a}{A}\right)^2 + \lambda^2 \\ I_2 &= \frac{1}{2}\left[\mathrm{Tr}(C)^2 - \mathrm{Tr}(C^2)\right] = \frac{1}{\lambda} + \left(\frac{A}{a}\right)^2 + \left(\frac{\lambda a}{A}\right)^2 \\ I_3 &= \det(C) = 1 \end{aligned} \tag{4.10}$$

$$W = C_{10}\left(I_1 - 3\right)) + C_{01}\left(I_2 - 3\right)) \tag{4.11}$$

where C_{10} and C_{01} are experimentally determined material properties [133]. The

stresses resulting from the strain density function and strain invariants are [132]

$$\begin{aligned}\sigma_a &= 2\left(\lambda_a^2\frac{\partial W}{\partial I_1} - \frac{1}{\lambda_a^2}\frac{\partial W}{\partial I_2}\right) + p_s \\ &= 2\left(C_{10}\frac{A^2}{\lambda^2 a^2} - C_{01}\frac{\lambda^2 a^2}{A^2}\right) + p_s \qquad (4.12)\\ \sigma_\phi &= 2\left(\lambda_\phi^2\frac{\partial W}{\partial I_1} - \frac{1}{\lambda_\phi^2}\frac{\partial W}{\partial I_2}\right) + p_s \\ &= 2\left(C_{10}\frac{a^2}{A^2} - C_{01}\frac{A^2}{a^2}\right) + p_s \qquad (4.13)\\ \sigma_z &= 2\left(\lambda_z^2\frac{\partial W}{\partial I_1} - \frac{1}{\lambda_z^2}\frac{\partial W}{\partial I_2}\right) + p_s \\ &= 2\left(C_{10}\lambda^2 - C_{01}\frac{1}{\lambda^2}\right) + p_s \qquad (4.14)\end{aligned}$$

where p_s is the hydrostatic pressure determined from the boundary conditions. The equilibrium equation when neglecting the body force is [135]

$$\frac{d\sigma_a}{da} = \frac{\sigma_\phi - \sigma_a}{a} \qquad (4.15)$$

The approach given to solve this equations is to substitute the equilibrium equations Eqs. 4.12-4.14 into 4.15 and integrate from r to a. The resulting equation, after replacing A^2 with Eq. 4.7 and using the boundary condition $\sigma_a(r) = -P$, is

$$\begin{aligned}\sigma_a &= -P + \int_r^a \frac{\sigma_\phi - \sigma_a}{a} \qquad (4.16)\\ &= -P + E\left(\ln\frac{a^2 - C_r}{r^2 - C_r} - 2\ln\frac{a}{r} + C_r\left(\frac{1}{r^2} - \frac{1}{a^2}\right)\right) \qquad (4.17)\end{aligned}$$

where E is given as

$$E = \frac{C_{10}}{\lambda} + C_{01}\lambda \tag{4.18}$$

The remaining stresses can be determined as a function of σ_a by subtracting Eq. 4.12 from Eqs. 4.13 and 4.14

$$\sigma_\phi = \sigma_a + 2C_r E \frac{2a^2 - C_r}{a^2\left(a^2 - C_r\right)} \tag{4.19}$$

$$\sigma_z = \sigma_a + \left(2C_{10}\lambda^2 - 2C_{01}\frac{1}{\lambda^2}\right) - \frac{2C_{10}}{\lambda}\frac{a^2 - C_r}{a^2} + 2C_{01}\lambda\frac{a^2}{a^2 - C_r} \tag{4.20}$$

The resultant forces can be determined through integration from r to R

$$F_\phi = l\int_r^R \sigma_\phi da = l\left(II_1 + II_2\right) \tag{4.21}$$

$$\begin{aligned} II_1 = {} & (r-R)\left[P + E\left(\ln\left(r^2 - C_r\right) - 2\ln r - \frac{C_r}{r^2}\right)\right] \\ & + E\left[R\ln\left(R^2 - C_r\right) - r\ln\left(r^2 - C_r\right) - 2(R-r)\right. \\ & \left. + \sqrt{C_r}\left(R\ln\frac{R+\sqrt{C_r}}{R-\sqrt{C_r}} - \ln\frac{r+\sqrt{C_r}}{r-\sqrt{C_r}}\right)\right] \\ & - 2E\left[R\ln R - r\ln r - (R-r)\right] \\ & - EC_r\left[\frac{1}{r} - \frac{1}{R}\right] \end{aligned}$$

$$II_2 = 2C_r E\left[\frac{\tanh^{-1}\frac{r}{\sqrt{C_r}}}{\sqrt{C_r}} - \frac{\tanh^{-1}\frac{R}{\sqrt{C_r}}}{\sqrt{C_r}} + \frac{1}{r} - \frac{1}{R}\right]$$

$$F_z = \int_r^R 2\pi a \sigma_a da = II_3 + II_4 + II_5 + II_6 \tag{4.22}$$

$$\begin{aligned} II_3 = {} & \pi\left(R^2 - r^2\right)\left[-P - E\left(\ln\left(r^2 - C_r\right) - 2\ln r - \frac{C_r}{r^2}\right)\right] \\ & + \pi E\left[\left(R^2 - C_r\right)\ln\left(R^2 - C_r\right) - \left(r^2 - C_r\right)\ln\left(r^2 - C_r\right)\right. \\ & \left. -2R^2\ln R + 2r^2\ln r\right] \\ & - 2EC_r\pi\ln\frac{R}{r} \end{aligned}$$

$$II_4 = \pi\left(R^2 - r^2\right)\left(2C_{10}\lambda^2 - 2C_{01}\frac{1}{\lambda^2}\right)$$

$$II_5 = -\frac{4\pi C_{10}}{\lambda}\left[\frac{R^2 - r^2}{2} - C_r\ln\frac{R}{r}\right]$$

$$II_6 = 2\pi\lambda C_{01}\left[C_r\ln\frac{R^2 - C_r}{r^2 - C_r} + R^2 - r^2\right]$$

Applying force balance to the PAM free-body diagram in Fig. 4.1 and using the tension force, T, the relations for the actuation force F is found

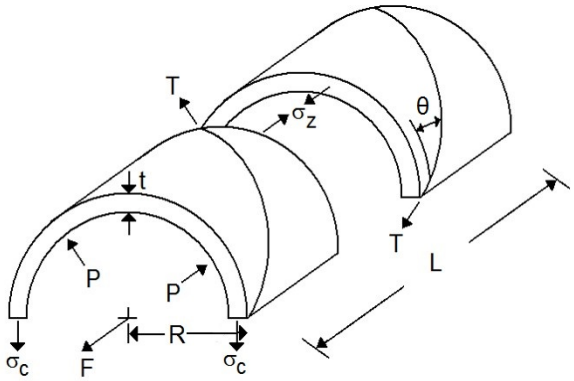

Figure 4.1: PAM free-body diagram

$$PrL = F_\phi + nT\cos\theta \tag{4.23}$$

$$F + P\pi r^2 = F_z + T\sin\theta \tag{4.24}$$

The PAM geometry to solve this system of equations is given by

$$L_0^2 + (2\pi n R_0)^2 = \lambda^2 L_0^2 + (2\pi n R)^2 \tag{4.25}$$

resulting in the PAM force

$$F = F_z - P\pi r^2 + \frac{PrL^2 - F_\phi L}{2\pi n^2 R} \tag{4.26}$$

The deformed bladder dimensions, r and R, can be found as

$$R = \frac{\sqrt{(1-\lambda^2)\,L_0^2 + (2\pi n R_0)^2}}{2\pi n}$$
$$r = \sqrt{R^2 - \frac{R_0^2 - r_0^2}{\lambda}}$$

where R is found using the length of the inextensible braid and n is the number of turns a single braid makes about the PAM, and r is found by relating the volume of the bladder before and after deformation.

4.3 Contractile PAMs

4.3.1 Experimental Testing

PAMs were fabricated in-house. The nominal length of the large PAM is 128.5 mm, the outer diameter of the bladder is 15.9 mm, and the bladder thickness is 1.59 mm. The braid angle with respect to radial direction is 72.86°. Experiments were conducted using an MTS machine to measure the axial actuation forces and displacement under different pressure levels. Figure 4.2 shows the experimental force-stroke results which are used to validate our predictions from the newly developed nonlinear quasi-static PAM force model.

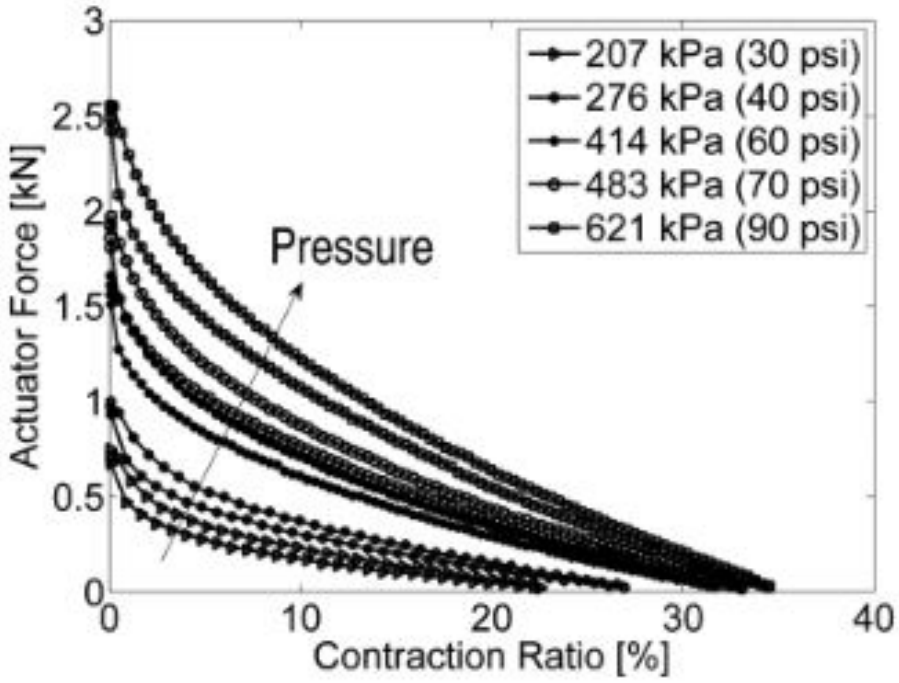

Figure 4.2: Large PAM: measured force-stroke plots as a function of inflation pressure

Miniature PAM experimental data were used to further validate our non-linear quasi-static model, as shown in Figure 4.3. The miniature PAM resting

length was 43.9 mm, the initial outer diameter was 4.6 mm, the braid angle is 73.5°. Commercially available silicone tubing material was used for the bladder. Again, due to the lack of silicone rubber material property data, the Mooney-Rivlin parameters listed were identified via an iterative parameter identification procedure.

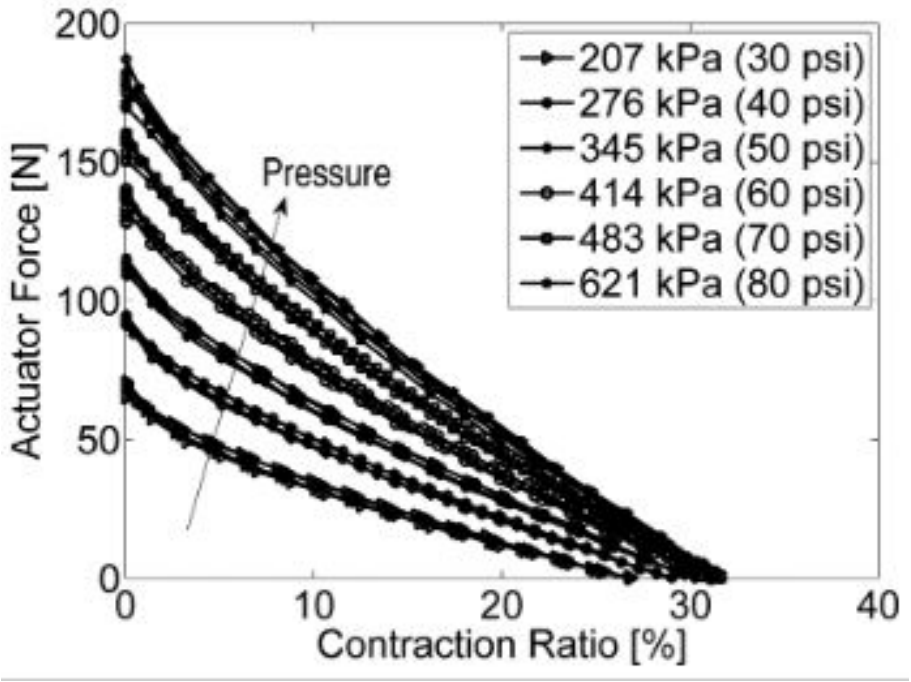

Figure 4.3: Miniaturized PAM: measured force-stroke plots as a function of inflation pressure.

4.3.2 Model Validation

The non-linear quasi-static model is first experimentally validated using data from the two contractile PAMs: a large PAM with a latex bladder and a miniature PAM with a V330 elastomeric material bladder. These bladder materials were chosen because neither material exhibited non-linear stiffening effects at their respective scales. Such non-linear stiffening has been observed in silicone elastomeric bladder materials at small scales [89]. All input parameters are determined from the PAM

geometry and material properties, except for the Mooney-Rivlin material coefficients. The Mooney-Rivlin coefficients were estimated starting from values found in the literature [86], and refined values were identified by manually updating the two coefficients to improve the fit with the respective large and miniature PAM test data. The Mooney-Rivlin coefficients could also be measured for specific bladder materials using standard material testing protocols. However, because these bladder tube materials were obtained commercially, it was not practical to perform these tests using flat plate specimens cut from the bladder tubes as residual stresses resulting from the forming processes would have corrupted estimates of the these coefficients. Therefore, parameter identification was used for the two Mooney-Rivlin coefficients.

Figure 4.4a shows the reconstructed force-stroke for a pressure of 207 kPa (30 psi). Clearly, the Gaylord model captures the block force (i.e. zero contraction case), but fails to capture the PAM behavior and free contraction (no load case). In contrast, the non-linear quasi-static model successfully captures both block force and free strain, as well as the force-stroke curve. It was observed that these PAM actuators clearly exhibit hysteretic behavior. In order to capture the hysteretic behavior, a non-linear dynamic model is needed. Figure 4.4b shows the bladder thickness variations under different contraction ratios. The bladder thickness is calculated based on the deformed inner and outer diameters discussed in Eq. 4.25 when the axial contraction ratio is specified. The bladder undergoes large deformation upon inflation justifying the use of finite strain theory to determine the stress components.

Figure 4.5 shows the force-stroke results for the different applied pressure levels. The modeled PAM forces correlate well with experimental data. Both block

force and free contraction ratio were accurately captured using the model. The actuation force is slightly over-predicted in the range of 5% to 25% contraction when the pressure is greater than 276 kPa (40 psi). Table 4.1 shows the average error of predicted and measured block force and free contraction results. The free contraction values are over-predicted for all pressure levels with a maximum single pressure error of 7.1%. The blocked force is over-predicted for both the 30 and 40 psi cases but under-predicted as pressure increases with a maximum error of less than 7%.

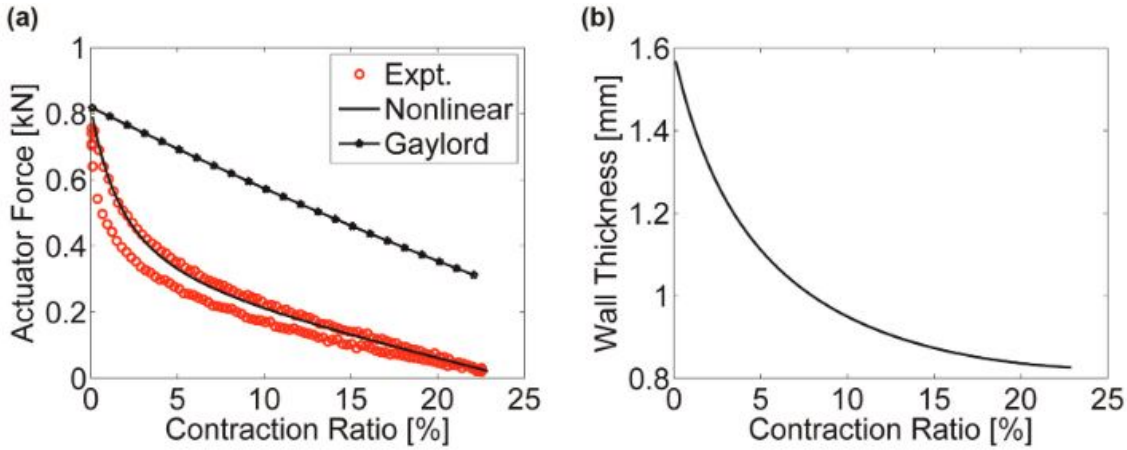

Figure 4.4: Large PAM: (a) comparison of predicted and measured force-stroke responses at 30 psi and (b) variation in bladder thickness for an inflation pressure of 30 psi.

Table 4.1: Contractile Modeling Results: Error and Bladder Properties

PAM	Contractile 4.6 mm	Contractile 15.9 mm
$BlockedForceError, \%$	3.6	0.2
$FreeContractionError, \%$	5.2	4.0
C_{10}, kPa	224	172
C_{01}, kPa	27.2	127

Figure 4.6 shows the comparison between the predicted and measured force-stroke results of the miniature PAM for actuation pressures ranging from 207 to 552 kPa (30-80 psi in 10 psi increments). The analytical predictions correlate well with

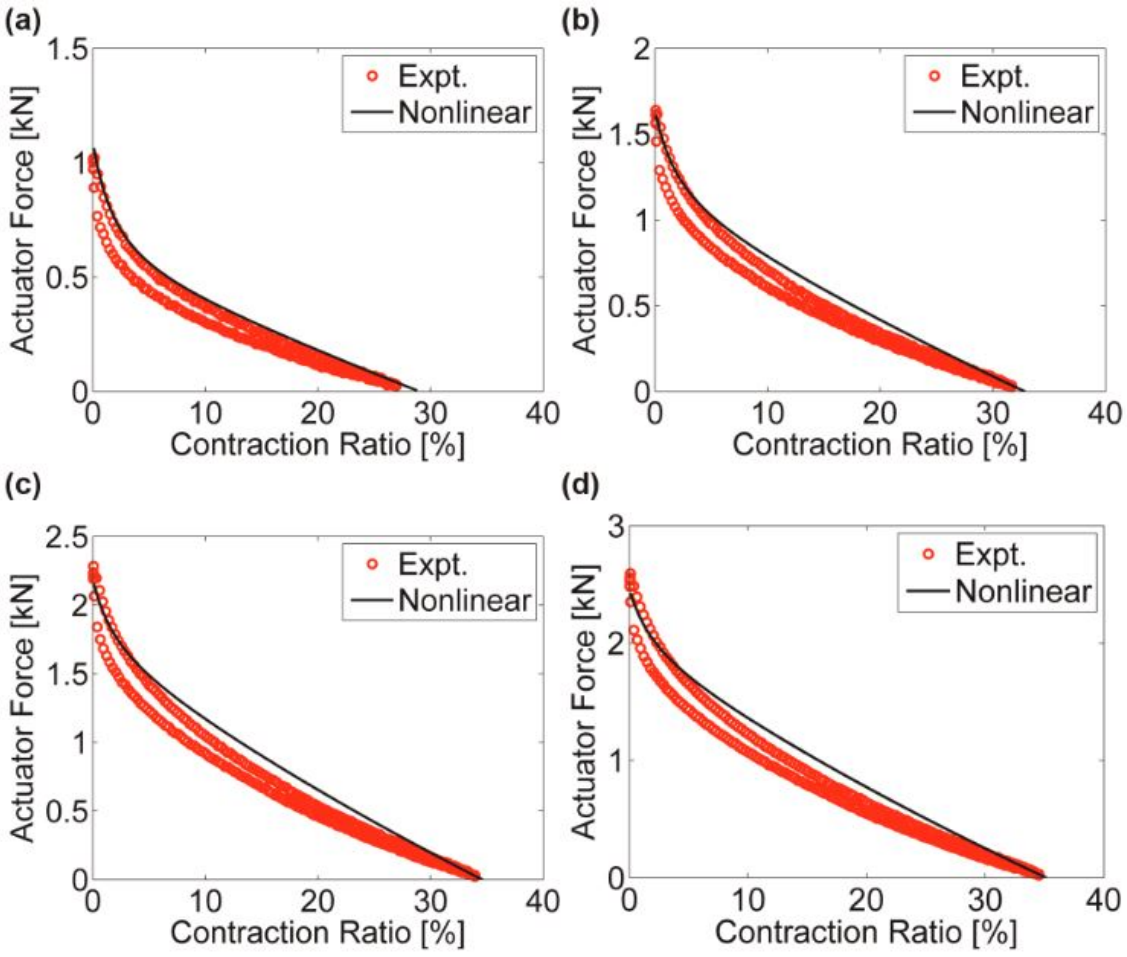

Figure 4.5: Large PAM: comparison of predicted and measured force-stroke responses under different pressure levels: (a) 276 kPa (40 psi), (b) 414 kPa (60 psi), (c) 552 kPa (80 psi), and (d) 621 kPa (90 psi).

experimental data except the cases of lowest and highest pressure actuations. Both pressure deadband (under low-pressure actuation) and non-cylindrical shape at the end fittings (under high-pressure actuation) may contribute to this discrepancy as discussed by Hocking and Wereley [89]. Table 4.1 shows the comparison of predicted and measured block force and free contraction results. The blocked forces are over-predicted for all pressure levels with a maximum error of 6%. The free contraction is under-predicted for 30 psi, but higher inflation pressure results are over-predicted with a maximum error of 8.4%.

4.4 Extensile PAMs

4.4.1 Experimental Testing

Two extensile PAMs were fabricated and quasi-statically tested to validate the non-linear material model for extending actuators. For contractile PAMs the constrained bladder radially expands generating an axial shortening and contracting force, while for extensile PAMs the constrained bladder radially contracts generating an axial elongation and extending force. Both extensile PAMs were built with latex bladders and polyethylene terephthalate (PET) braids. The large extensile PAM has a length of 200 mm (7.87 in), an outer diameter of 25 mm (1 in), a bladder thickness of 3.2 mm (0.125 in), and braid angle of 25.0°. The small extensile PAM has a length of 190 mm (7.5 in), an outer diameter of 8.5 mm (.33 in), a bladder diameter of 6.4 mm (.25 in), a bladder thickness of 1.6 mm (0.625 in), and a braid angle of 25.0°. To achieve the braid angle necessary for an extensile PAM excess braid was pushed on

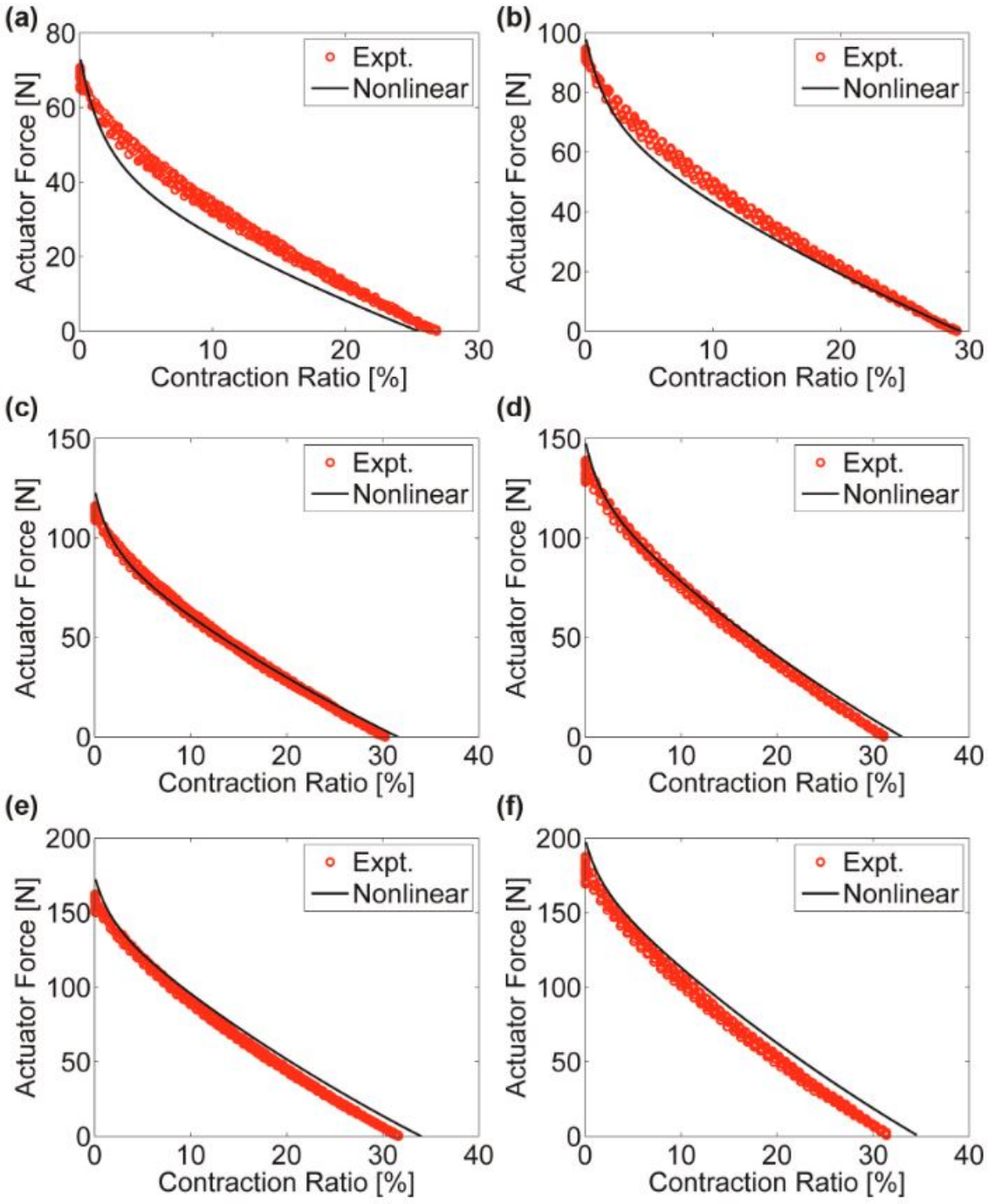

Figure 4.6: Miniaturized PAM: comparison of predicted and measured force-stroke responses under different pressure levels: (a) 207 kPa (30 psi), (b) 276 kPa (40 psi), (c) 345 kPa (50 psi), (d) 414 kPa (60 psi), (e) 483 kPa (70 psi), and (f) 552 kPa (80 psi).

during fabrication creating a gap between the bladder and braid at rest in the small extnesile PAM. Due to the limited PET braid and latex tubing availability, this PAM used a 0.64 cm (0.25 in) diameter bladder. For the model validation, the bladder thickness of this PAM input into the model is adjusted to account for the inflation of the bladder due to the initial difference between the bladder outer diameter and PAM outer diameter. The PAMs were each tested quasi-statically with three cycles between blocked force and free stroke. The two extensile muscles are pictured in Fig. 4.7 and the properties are listed in Table 4.2.

Figure 4.7: Pneumatic Artificial Muscles. Left to Right: Small Extensile, Large Extensile, Large Contractile, Small Contractile

Table 4.2: PAM Material Properties

PAM	Diameter	Bladder thickness	Braid angle	Length
Small Extensile	8.5 mm	1.6 mm (1.0 mm*)	25.0°	200 mm
Large Extensile	25 mm	3.2 mm	13.5°	190 mm

*thickness after initial bladder expansion

The PAM testing was conducted on a MTS machine between 552 kPa (80 psi) and 206 kPa (30 psi) in increments of 69 kPa (10 psi). Each test consisted of three cycles starting from the blocked force condition reaching free stroke then returning to the blocked force condition. Due to the tendency of extensile PAMs to

Figure 4.8: MTS Testing of Extensile PAM

buckle, the PAM was placed inside of a telescoping clear plastic tube to constrain the out of plane deflections during testing, Fig. 4.8. The force-stroke curves recorded during the quasi-static testing are presented in Fig. 4.9. The higher braid angle of the small extensile PAM (closer to the limit of no motion, 35.26°) results in length changes more similar to contractile PAMs.

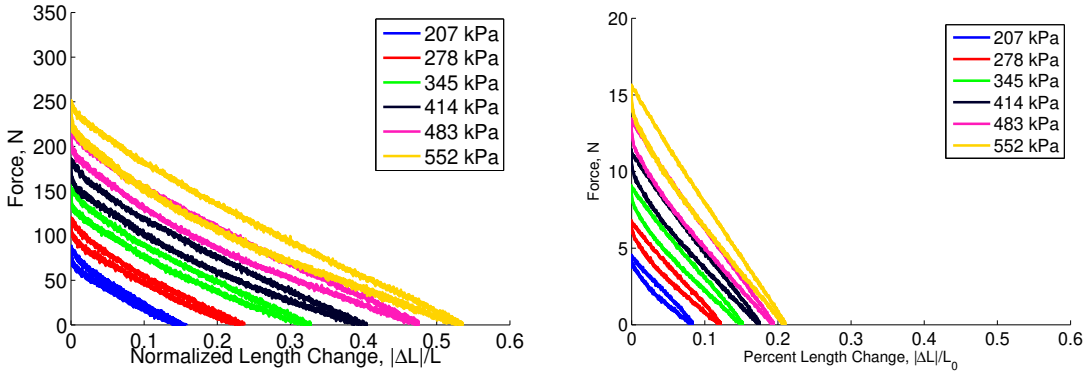

(a) Extensile PAM 2.5 cm

(b) Extensile PAM 0.85 cm

Figure 4.9: PAM MTS Testing Data

4.4.2 Model Validation

As with the contractile PAMs, all input parameters are determined from the PAM geometry except of the Mooney-Rivlin coefficients. Again a commercially available latex rubber was used, and to attempt to experimentally calculate the Mooney-Rivlin coefficients for this rubber tubing used for the bladders is not feasible due to the residual stresses in the material when cut and laid flat, so these numbers were chosen from the comparing the model to experimental data. As this latex tubing used here is not exactly the same latex in each PAM or the latex used for the large contractile PAM, there is no expectation that the Mooney-Rivlin coefficients are identical. The chosen Mooney-Rivlin coeficients were of the same order of magnitude indicating the material model is plausible given the large number of factors effecting material properties such as fabrication variability and light exposure.

Considering the model results comparing the model to the average force at each contraction of the PAM test, ignoring hysteresis, the blocked force is slightly under-predicted for both extensile PAMs. For the large extensile PAM, the free extension becomes over predicted as the pressure increases. For the small extensile PAM, the free extension is over-predicted at low pressure and under-predicted for high pressures. The average modeling error of the force contraction curve is small as seen in Fig. 4.10 and Table 4.3. The Mooney-Rivlin coefficients were again manually adjusted to reduce the error between the model and data. The resulting Mooney-Rivlin coefficients were chosen such that $C_{01} = 0$ reducing the material to a Neo-Hookean model for a simple material model, but more accurate Mooney-Rivlin

coefficients could improve the model fit.

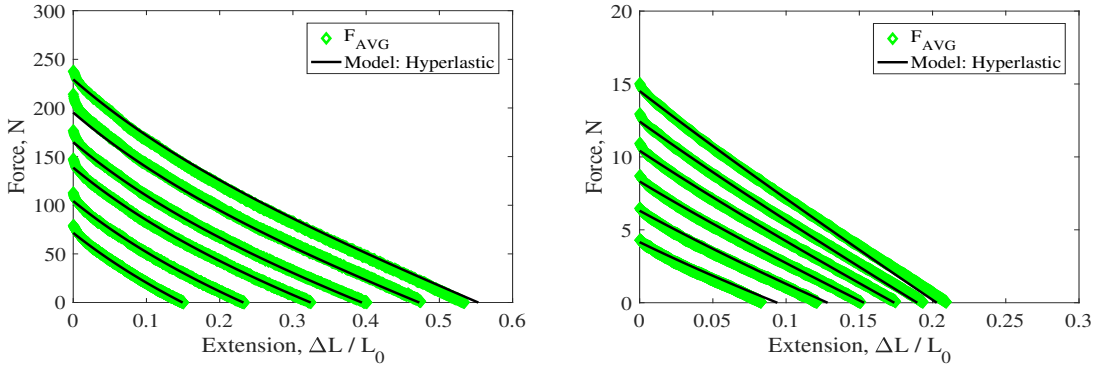

(a) Extensile PAM 2.5 cm (b) Extensile PAM 0.85 cm

Figure 4.10: PAM MTS Testing Data

Table 4.3: Extenisle Modeling Results: Error and Bladder Properties

PAM	Extensile 0.85 cm	Extensile 2.5 cm
$Error, \%$	2.42* (3.21)	1.41 (1.33*)
C_{10}, kPa	213	285
C_{01}, kPa	0	0

*excluding 207 kPa due to low force level in small PAM

4.5 Conclusions

Experimental force-stroke results from two different sizes and two different types of PAM actuators were used to validate our newly developed quasi-static non-linear model and good agreement was achieved. It is clearly demonstrated that the accurate prediction of non-linear stress components in the bladder material is the key for the PAM model development. The Mooney-Rivlin model was adopted to represent the rubber material constitutive equation in our model, in which two constants are assumed. In all simulations, we determined them via an iterative process due to the lack of rubber stress and deformation experimental data. We

expect that more accurate Mooney-Rivlin parameters could further improve our predictions. On the other hand, we may need to use other hyperelastic models to represent the rubber behaviors to meet a wide range of actuation conditions. In this case, we can simply update the hyperelastic model and derive corresponding solutions based on the existing finite strain framework. The developed physics-based non-linear quasi-static model was applied to contractile and extensile PAMs. It was shown for both contractile PAMs and extensile PAMs that this model can accurately model PAM behavior at multiple scales. The model developed can serve as a PAM design tool because PAM physical design variables (original length, bladder dimensions, and material properties), as well as actuation conditions, are input parameters in the model. One disadvantage is that the Mooney–Rivlin parameters, C_{10} and C_{01}, may not be known and may need to be identified from PAM test data or bladder material testing data.

Chapter 5: Single Section Bio-Inspired Pneumatic Artificial Muscle Continuum Robot Arm

5.1 Introduction

Continuum robots are a growing field of robotics which allow for a high degree of flexibility to mimic various biological structures. These robots can take the form of rigid hyper-redundant robotics, [54] to many examples in the field of soft robotics [43,47,75]. Soft actuators lend themselves to continuum robotics due to their ability also achieve high flexibility. In this work, a brittle star inspired continuum robotic manipulator was constructed with an plastic ossicle structure actuated by pneumatic artificial muscles (PAMs). PAMs are a highly compliant light-weight actuator controlled by pressurized fluid, typically air. This compliant nature makes them well suited for continuum robotics. PAMs have been applied in applications including trailing edge flap actuation [112], high-strength robotic arms [120], and soft robotic arms [29].

The majority of continuum PAM robotic manipulators have been constructed from extensile PAMs [29, 49, 51], PAMs which extend when pressurize, with a few examples of manipulators constructed from contractile PAMs [48], PAMs which

contract and radially expand when pressurize. The minimal radius decrease seen in extensile PAMs allows strategies such as distributed ties or strings to maintain the actuator alignment and reduce active PAM buckling during operation. The same strategies are difficult to employ in contractile PAM manipulators due to the large radius change the actuators experience and tend to lead to inactive PAM buckling.

An overview of PAM modeling can be found in the work of Tondu [91]. The force balance modeling used in this work is an extension of the work of Kothera et al. [87], with non-linear stress strain modeling [89], and a linear relationship with pressure as described in Chapter 2.

Continuum arm modeling involves a number of simplifying assumptions or continuum mechanics models that are computationally slow due to their complexity. The constant curvature assumption is used in many modeling techniques [12]. Variable curvature kinematics can be broken down into sections of constant curvature [69]. Dynamic models can include beam equations [55], continuum mechanics [58, 136], or simplifying assumptions such as constant curvature kinematics [65, 67].

In this work, a continuum arm section is constructed from three PAMs with an incorporated ossicle-inspired structure towards the goal of eliminating the inactive PAM buckling. The PAM was modeled using a force balance modeling approach, and the arm motion was modeled with a constant curvature kinematic model using the center of gravity to calculate the required force. The motion of the arm was recorded and compared to the expected model for an unloaded case as well as a set of loading conditions.

5.2 Bio-Inspired Manipulator Design

The manipulator section is constructed of 3 PAMs arranged radially between two end plates. The relative position and orientation of the end plates define the pose of the section. When a PAM is pressurized, the PAM contracts and produces bending in the section. The PAMs used in this work are fabricated with a latex rubber bladder, a PET (polyethylene terephthalate) braided sleeve and aluminum end fittings, Fig. 5.1. Due to the thin bladders used to constructed PAMs and the high force a contracting PAM can produce, the unpressurized PAMs are likely to buckle. To prevent this buckling, a ossicle structure inspired by those found in brittle stars was added to the section. The ossicles in the arms of brittle stars serve mainly as an exoskeleton to define the shape of deformed arm segment and constrain the maximum bending achievable in the segment. This lightweight minimally-constrained addition provides structure to support the compressive load from the active PAM and maintain the desired constant curvature in the section. The nominal properties of the PAMs used in the work are listed in Table 3.1.

Table 5.1: PAM Material Properties

Diameter	Bladder thickness	Braid angle	Length
1 cm	0.16 cm (0.081 cm*)	67°	27 cm

*thickness after initial bladder expansion

The ossicle-inspired structure employed is a stacked hub and spoke arrangement, as seen in Fig. 5.2. A thread is run through the center of the ossicles to ensure alignment during construction and operation. A second loose thread is run through one spoke to improve radial alignment throughout operation. Additionally

Figure 5.1: Type of miniature PAM used in this work.

the spokes have a flange to allow for some rotation of the ossicles. The segment is capable of around 45° of bending prior to the structure fully engaging with some additional motion possible. The PAMs used in the segment were chosen from a large set of PAMs to have similar resting lengths and free contraction values at low pressures. The assembled segment is shown in Fig. 5.4

5.3 Manipulator Modeling

Models of both the PAM behavior and the force required to move the arm are necessary to relate a desired angle and bending plane to the required PAM input pressures.

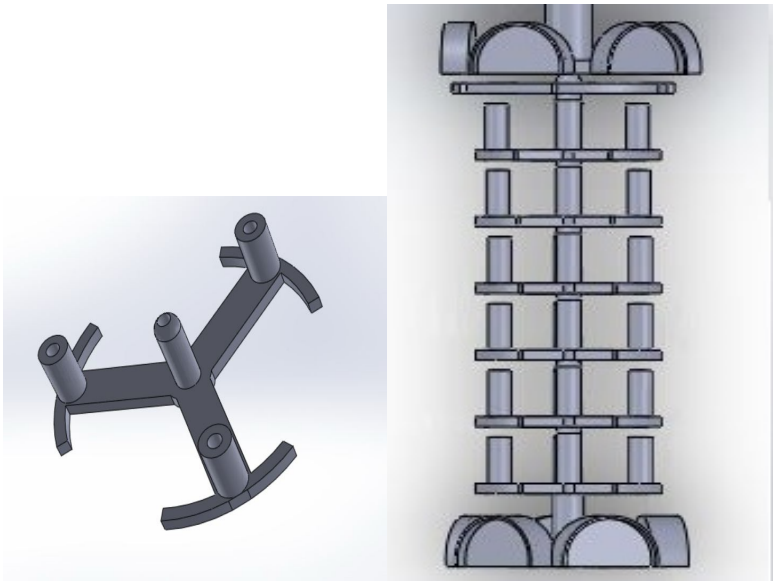

(a) Single Ossicle (b) Assembled Ossicle structure

Figure 5.2: Design of ossicle structure with PAMs removed

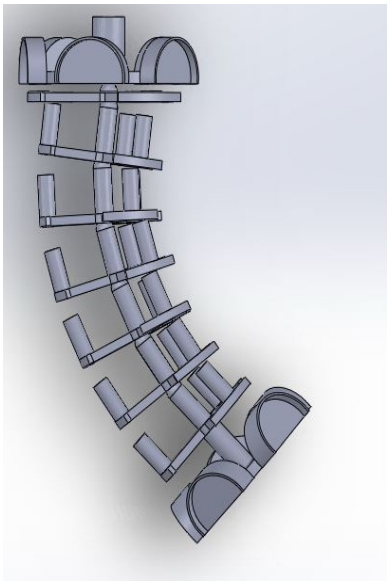

Figure 5.3: Bending of ossicle structure with PAMs removed

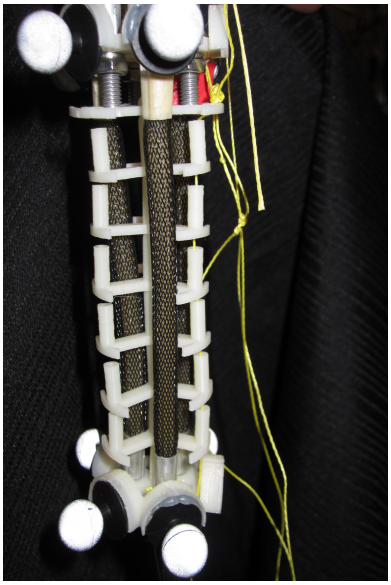

Figure 5.4: Assembled PAM section with ossicle structure

5.3.1 Pneumatic Artificial Muscle Modeling

The PAM force was modeled with using a force balance model with a nonlinear stress strain relationship for the bladder model. The PAM force is given by

$$F(L,P) = \frac{P'}{4\pi N^2}\left(3L^2 - B^2\right) + \sigma_z \frac{V_B}{L} - \sigma_c \frac{tL^2}{2\pi R N^2} \tag{5.1}$$

where P' is the gage pressure, P, minus the dead-band pressure, P_{DB}, L is the current length of the PAM, B is the length of the braid, N is the number of turns the braid around the PAM, σ is the stress, V_B is the volume of the bladder, t is the current thickness of the bladder, and R is the current radius of the bladder. The stress-strain relationship used is

$$\sigma = E_1(P)\epsilon \tag{5.2}$$

where E_1 is a linear function of pressure that relate strain, ϵ, to stress, σ. This relationship applies to both the circumferential, ϵ_c, and axial, ϵ_z, strains. For a PAM the resulting strains are

$$\epsilon_z = \frac{L}{L_0} - 1 \tag{5.3}$$

$$\epsilon_c = \frac{R - \frac{t}{2}}{R_0 - \frac{t_0}{2}} - 1 \tag{5.4}$$

Due to the low expected force compared to the blocked force of the actuator, the bladder relationship was modeled to reproduce the free contraction curve, and provide the best match in the low force regime. More extensive testing and higher order models can be chosen to improve the fit throughout the range of PAM operation. This free contraction vs. pressure data was used to determine the bladder model using the recorded data and a least squares fit for the $E_1(P)$ relationship. The comparison of free contraction data to the model are shown in Fig. 5.5.

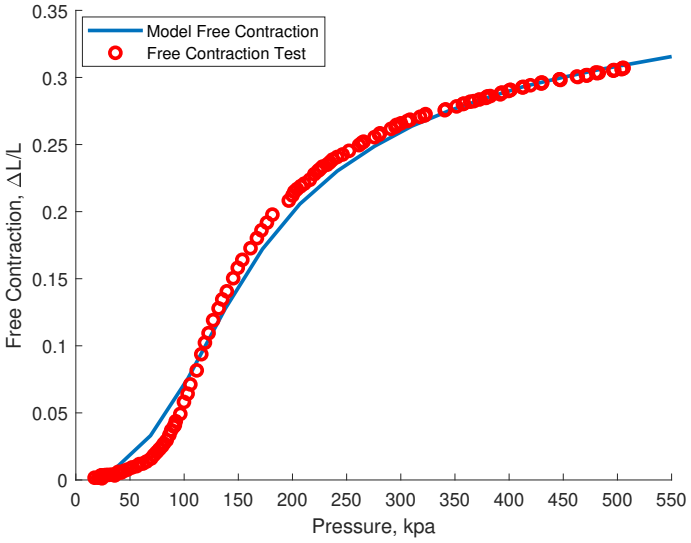

Figure 5.5: Comparison of free contraction experiment and model.

5.3.2 Manipulator Static Model

The manipulator modeling approach used in this work, starts from the constant curvature efficient dynamics for continuum arms developed by Godage *et al* [67]. In this approach the energy of the center of gravity of the bending segment is calculated and used to find the Lagrangian dynamics with respect to the actuator length. The current work considers the center of gravity of the bending section separately from the concentration of weight at the tip of the bending section. For the arm constructed in this work the concentration of mass at the tip of the arm accounts for nearly 80% of the weight of the arm as well as being located more distally. The bending section weighs approximately 5 g while the section divider weighs approximately 18 g. The position, p_{CC_i}, and orientation, R_{CC_i}, throughout the bending section are found in a number of forms in literature. For this work the length, h_i, bending angle, θ_i, and bending plane, ϕ_i are used to define the position and orientation. The variable h_i was chosen to help the reader distinguish between the length of the PAM used here and in other literature from the length of the bending section [67]. The variable s describes the position along the segment, with $s = 0$ at the base and $s = 1$ at the end. A 2D representation of the section orientation is shown in Fig. 6.2 with a point mass after $s = 1$ representing the concentration of mass of the section plate and any added mass during experimental testing in the following section. The choice of R_{CC_i} reorients the bending plane with the initial frame [12]. The form of $p_{CC_i}(s)$ and R_{CC_i} used here is shown below

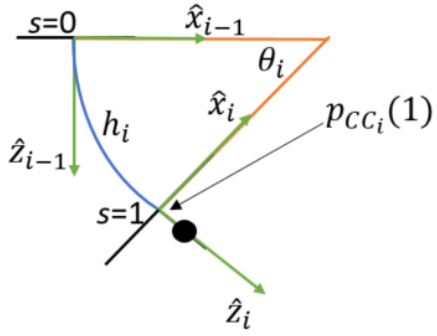

Figure 5.6: Single section orientation used in this work. Gravity acts in the positive $\hat{z_0}$ direction and ϕ_i is a rotation about $\hat{z_{i-1}}$.

$$p_{CC_i}(s) = \begin{bmatrix} h_i \cos\phi_i \frac{1-\cos\theta_i s}{\theta_i} \\ h_i \sin\phi_i \frac{1-\cos\theta_i s}{\theta_i} \\ h_i \frac{\sin\theta_i s}{\theta_i} \end{bmatrix} \tag{5.5}$$

$$R_{CC_i} = \begin{bmatrix} \cos^2\phi_i\,(cos\theta_i - 1) + 1 & \sin\phi_i \cos\phi_i\,(\cos\theta_i - 1) & \cos\phi_i \sin\theta_i \\ \sin\phi_i \cos\phi_i\,(\cos\theta_i - 1) & \sin^2\phi_i\,(\cos\theta_i - 1) + 1 & \sin\phi_i \sin\theta_i \\ -\cos\phi_i \sin\theta_i & -\sin\phi_i \sin\theta_i & \cos\theta_i \end{bmatrix} \tag{5.6}$$

The section parameters are related to the actuator values with the following equations. For the segment considered in this work the first actuator is located 60° from the initial bending plane. In these equations l_{i1}, l_{i2}, and l_{i3} represent the change in length of the first, second, and third actuators, respectively. L_{i0} is the initial length of the segment, and r_i is the average radius of the actuator from the

center of the end plates

$$h_i = h_{i0} + \frac{l_{i1} + l_{i2} + l_{i3}}{3} \tag{5.7}$$

$$\theta = \frac{\sqrt{l_{i1}^2 + l_{i2}^2 + l_{i3}^2 - l_{i1}l_{i2} - l_{i1}l_{i3} - l_{i2}l_{i3}}}{3r_i} \tag{5.8}$$

$$\phi_{i=1} = \tan^{-1}\left(\frac{\sqrt{3}\,(l_{i3} - l_{i1})}{(2l_{i2} - l_{i3} - l_{i1})}\right) = \tan^{-1}\left(\frac{y_i}{x_i}\right) \tag{5.9}$$

The above and following relationships can be substituted into the position and orientation equations to put these equations in a form where the need to divide by $\theta_i = 0$ can be avoided, where x_i and y_i are used to simplify the following expressions.

$$\sin\left(\tan^{-1}\phi_i\right) = \sin\left(\tan^{-1}\frac{y_i}{x_i}\right) = \frac{y_i}{\sqrt{x_i^2 + y_i^2}} \tag{5.10}$$

$$\cos\left(\tan^{-1}\phi_i\right) = \cos\left(\tan^{-1}\frac{y_i}{x_i}\right) = \frac{x_i}{\sqrt{x_i^2 + y_i^2}} \tag{5.11}$$

$$\sqrt{x_i^2 + y_i^2} = 2\sqrt{l_{i1}^2 + l_{i2}^2 + l_{i3}^2 - l_{i1}l_{i2} - l_{i1}l_{i3} - l_{i2}l_{i3}} = 3r_i\theta \tag{5.12}$$

Substituting in the above relationships yields,

$$p_{CC_i}(s) = \begin{bmatrix} \frac{h_i x_i}{9r_i}\frac{1-\cos\theta_i s}{\theta_i^2} \\ \frac{h_i y_i}{9r_i}\frac{1-\cos\theta_i s}{\theta_i^2} \\ h_i\frac{\sin\theta_i s}{3\theta_i} \end{bmatrix} \tag{5.13}$$

$$R_{CC_i} = \begin{bmatrix} 1 + \frac{x_i^2}{9r_i^2}\frac{\cos\theta_i - 1}{\theta_i^2} & \frac{x_i y_i}{9r_i^2}\frac{\cos\theta_i - 1}{\theta_i^2} & \frac{x_i}{3r_i}\frac{\sin\theta_i}{\theta_i} \\ \frac{x_i y_i}{9r_i^2}\frac{\cos\theta_i - 1}{\theta_i^2} & 1 + \frac{y_i^2}{9r_i^2}\frac{\cos\theta_i - 1}{\theta_i^2} & \frac{y_i}{3r_i}\frac{\sin\theta_i}{\theta_i} \\ -\frac{x_i}{3r_i}\frac{\sin\theta_i}{\theta_i} & -\frac{y_i}{3r_i}\frac{\sin\theta_i}{\theta_i} & \cos\theta_i \end{bmatrix} \tag{5.14}$$

where the expression $\frac{1-\cos\theta_i s}{\theta_i^2}$ and $\frac{\sin\theta_i s}{\theta_i}$ can be replaced with their Taylor expansions of sufficient order

$$\frac{1-\cos\theta_i s}{\theta_i^2} = -\frac{s^2}{2} + \frac{\theta_i^2 s^4}{24} - \frac{\theta_i^4 s^6}{720} + O(\theta_i^6 s^8) \tag{5.15}$$

$$\frac{\sin\theta_i s}{\theta_i} = s - \frac{\theta_i^2 s^3}{6} + \frac{\theta_i^4 s^5}{120} + O(\theta_i^6 s^7) \tag{5.16}$$

Similarly, $\cos\theta_i$ can be expanded, and all these expansions result in expressions with only integer powers of l_{i1}, l_{i2}, and l_{i3}. The center of gravity of the bending segment can be found by integrating the pose of the segments from $s = [0, 1]$

$$\beta_i = \int_0^1 p_{CC_i} ds \tag{5.17}$$

The global position of the center of the first segment, p_{β_1}, and the center of the tip mass, p_{M_1} can be calculated

$$p_{\beta_1} = \beta_1 \tag{5.18}$$

$$p_{M_1} = p_{CC_1}(1) + \frac{1}{2} R_{CC_1} p_{M_{lcl_1}} \tag{5.19}$$

where $p_{M_l cl_1}$ is the center of mass at the tip of the section From these positions and the mass of the bending section, m_1, and the mass of the tip, M_1 the potential energy

can be calculated

$$V_E = (p_{\beta_1} m_1 + p_{M_1} M_1)^T \begin{bmatrix} 0 \\ 0 \\ g \end{bmatrix} \tag{5.20}$$

Using the Lagrangian dynamics expression with the kinetic energy equal to zero, the force required due to gravity can be found using

$$G = \frac{\partial V_E}{\partial l} \tag{5.21}$$

where l is a vector of the change in PAM lengths, $l = [l_{11,12}, l_{13}]^T$ and this required force vector can than be related to the PAM force found in the previous section,

$$G(l) = F(L_0 - l, P) \tag{5.22}$$

5.4 Section Bending Experimental Results

Due to the radial symmetry of the manipulator, the manipulator was tested by pressurizing a single muscle and recording the pressure and pose throughout the test. To verify the model an experiment was conducted to compare a desired angle to the applied pressure required to achieve that angle. The length of the actuators are required both to calculate angle and to determine the pressure to produce a desired force. Given the designed maximum section angle from Section 5.2 and assuming the length of the inactive PAMs is unchanged, the length of the active PAM can be calculated from Eq. 5.8. With this length, the force equations in Eq.

2.4 can be rearranged to solve for active PAM pressure. There is a length where this relationship is not invertible, but it occurs outside of the operating range of a PAM. After testing the manipulator without load, the test was repeated for a set of loads, realized using weights hung from the center of gravity of the tip.

The ossicles were also removed from the arm and the test was repeated for the same loads without the ossicle structure. The pressure angle relationship for the two methods is shown with the saturation behavior of the ossicle free case, Fig. 5.7. The ossicles have little effect on the pressure to achieve desired angles at low loads, but as the load and angle increases the ossicle structure outperforms the ossicle free structure, Fig. 5.8.

To compare the theoretical values calculated as described above to the experimental values, the position and orientation of each end of the section was recorded with Vicon Tracker using the MX-F40 cameras and recording the data in Matlab. Using the pose and accounting for the placement of the markers on the rigid end plates, the length can be calculated, Eq. 5.23 [12].

$$l_{ij} = h_i + r_i\theta\cos(\phi_{ij} - \phi_i) \tag{5.23}$$

where l_{ij} is the length of PAM j in section i, and ϕ_{ij} is the orientation of that PAM on the plate. The pressure is recorded with pressure sensors and relayed to Matlab through a serial communication with an Arduino Mega board. Both the model of PAM length and PAM pressure are sensitive to any initial compression of the PAMs and lengthening of the inactive PAMs, but the experimental length is also sensitive

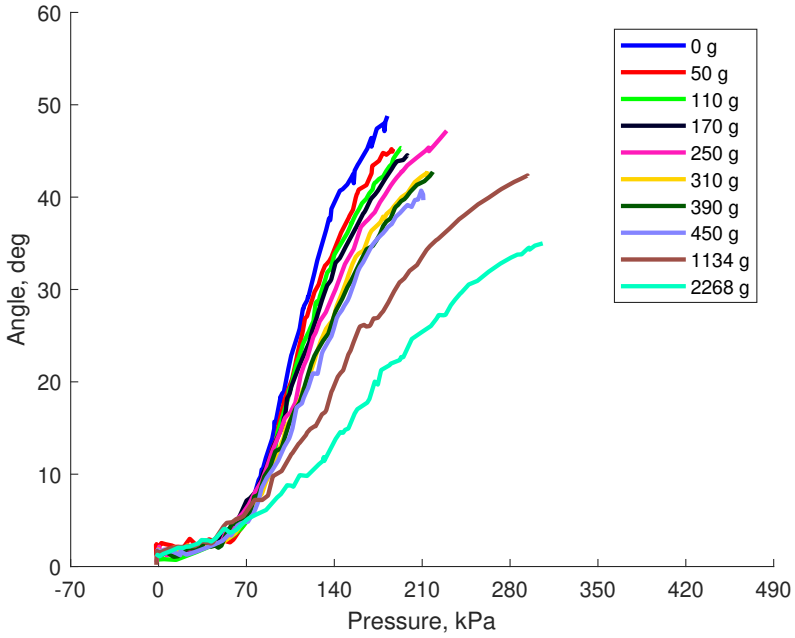

(a) Ossicle Structure Included

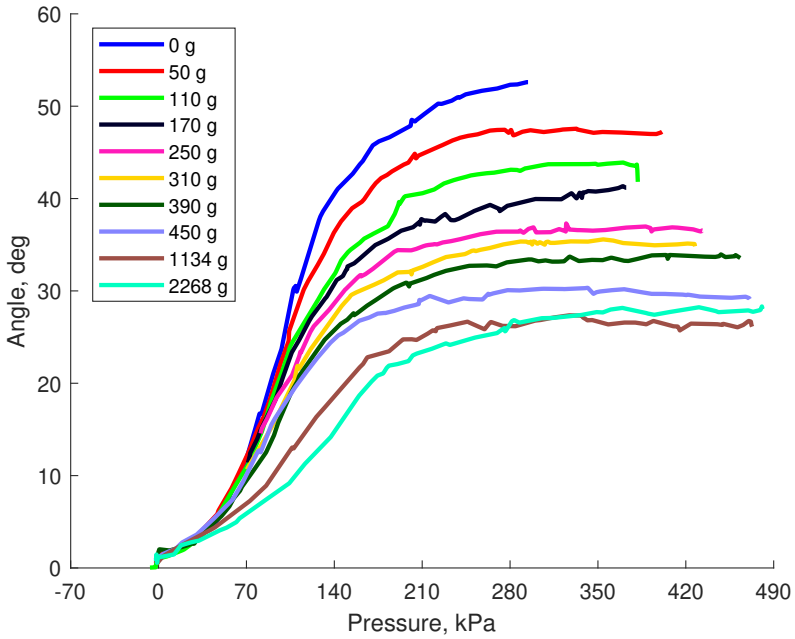

(b) Ossicle Structure Removed

Figure 5.7: Angle vs. Pressure with and without ossicle structure

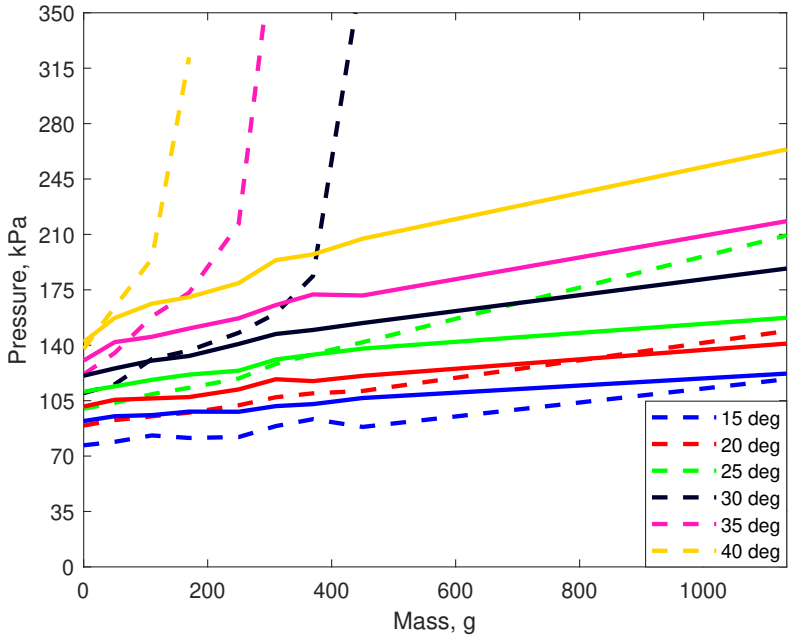

Figure 5.8: Pressures required to achieve a given angle for a known load. Dashed lines represents the ossicle free arm, and solid represents the arm with ossicles.

to the to the exact material properties of the constructed arm. The length-angle relationship, Figs. 5.9-5.10, does not match indicating there is some change in length in inactive PAMs as the section actuates. When treating only the active PAM as changing in length, the pressure-angle relationships, Figs. 5.11-5.12, can capture some of the low weight and angle behavior, but fail to model the full relationship as expected due to the sensitivity of PAM length on pressure. When using the length data obtained from the experimental analysis, the pressure-behavior is more fully captured, Figs. 5.13-5.14. Due to the hysteresis inherent in PAMs which is here unmodeled, the average pressure-angle relationship is calculated to determine the model accuracy. For the experimental test pressure was the input and the angle of the section was measured, but the pressure from the model was solved given the PAM length changes, determined from the experimental poses, so the error is calculated

as both the difference in pressure for a given angle, Fig. 5.15 and the difference in angle for a given pressure, Fig. 5.16. Both of these metrics are then normalized and compared, with similar levels of normalized error for both cases excluding 5 lb load case where the metrics begin to deviate, Fig. 5.17. The error normalized by the mean of the pressure input in each test is approximately 4% for the tests up to 2.5 lbs of added weight, while the modeling error of the free contraction absolute value of the difference normalized by the mean of the free contraction values is approximately 2% for the PAM model used in the work.

5.5 Conclusions

A pneumatic artificial muscle actuated continuum arm section was modified to introduce a bio-inspired ossicle structure. This arm section was modeled using constant curvature kinematic assumption to determine the position of the center of gravity of the bending section and its end plate with respect to the PAM length. The model captures the pressure versus angle trends with future consideration for initial PAM properties and improved PAM modeling at low pressures. This modeling will be applied to a multi-section arm with improvements to handle initial compression of the PAMs due to the ossicle structure and lengthening of the PAMs during loading and actuation. Introducing ossicles increased the load capacity of the arm allowing the arm achieve a bending angle of over 40° with 1134 g when without ossicles the arm doesn't achieve 30°.

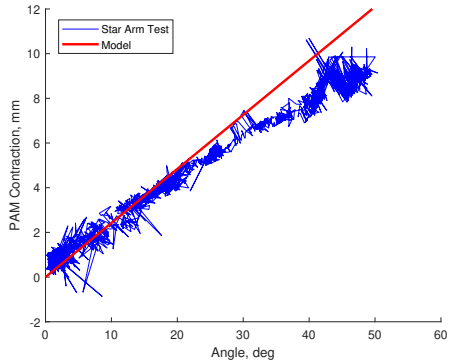

(a) No added weight

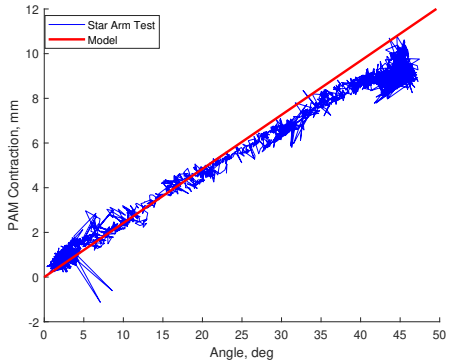

(b) 50 g added weight

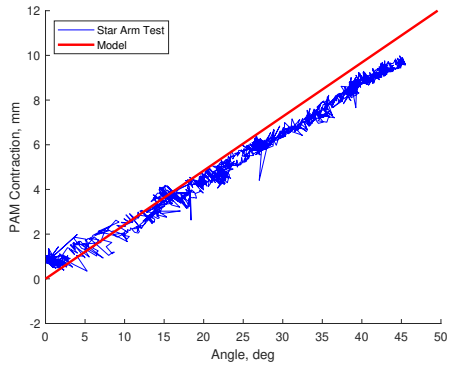

(c) 110 g added weight

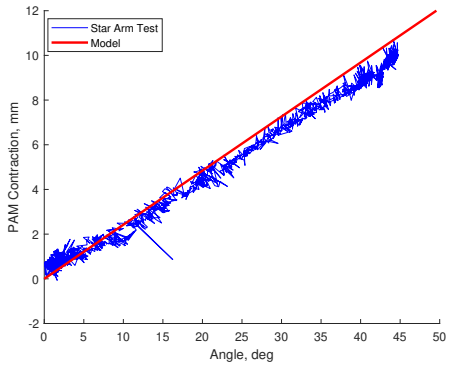

(d) 170 g added weight

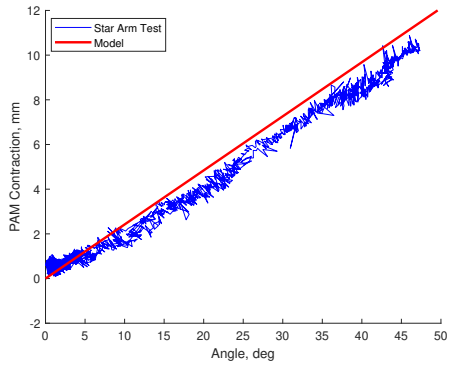

(e) 250 g added weight

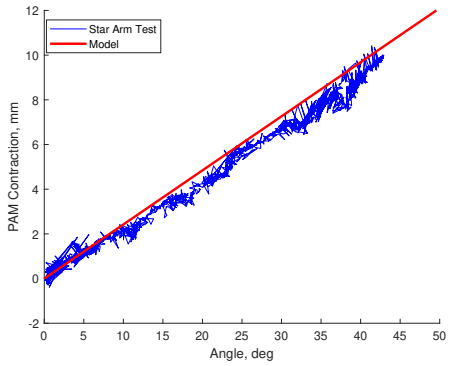

(f) 310 g added weight

Figure 5.9: Angle vs. Length Tests

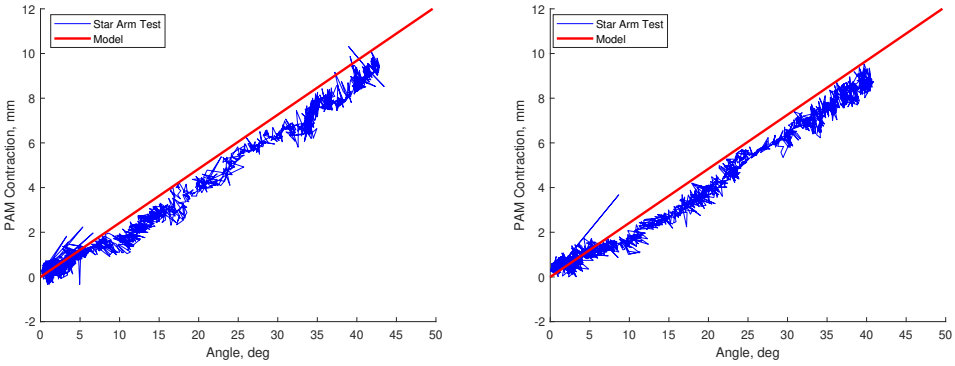

(a) 390 g added weight

(b) 450 g added weight

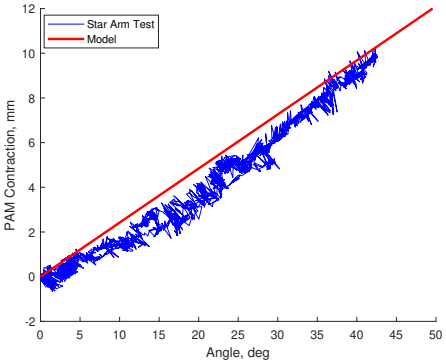

(c) 1134 g added weight

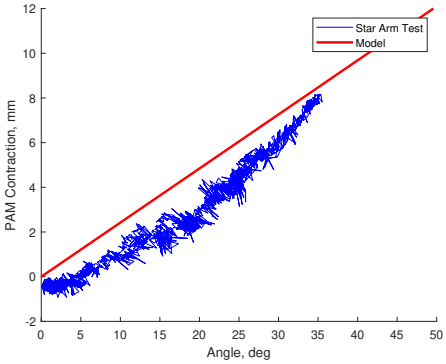

(d) 2268 g added weight

Figure 5.10: Angle vs. Length Tests

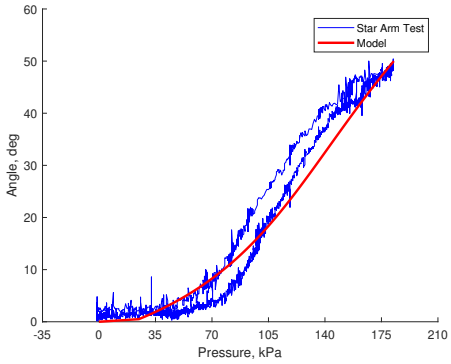

(a) No added weight

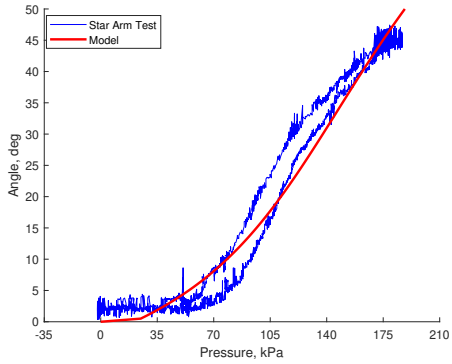

(b) 50 g added weight

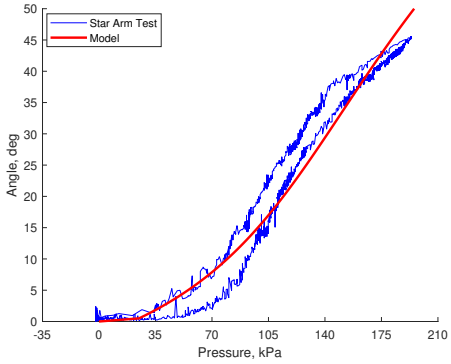

(c) 110 g added weight

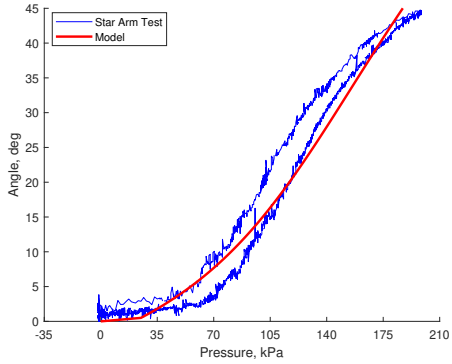

(d) 170 g added weight

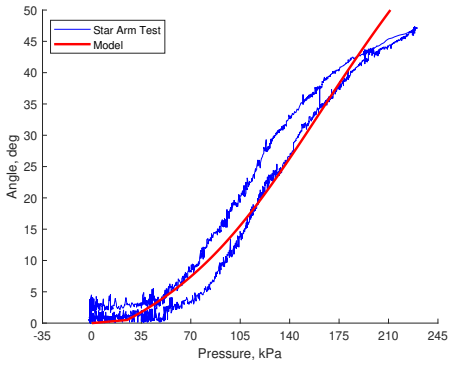

(e) 250 g added weight

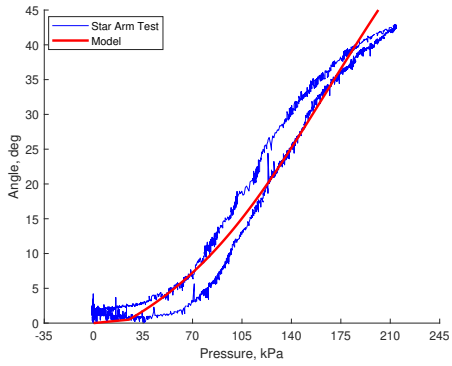

(f) 310 g added weight

Figure 5.11: Pressure vs. Angle Comparisons

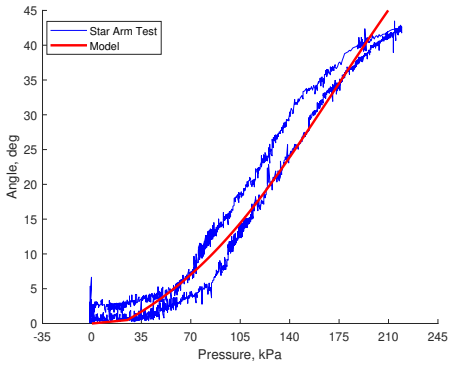

(a) 390 g added weight

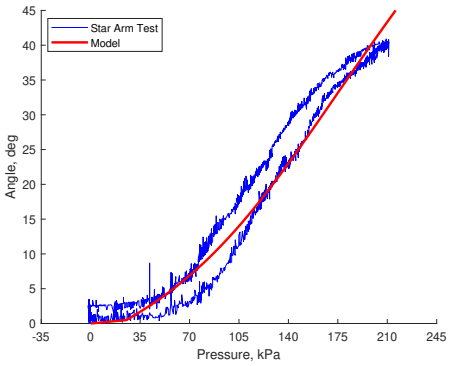

(b) 450 g added weight

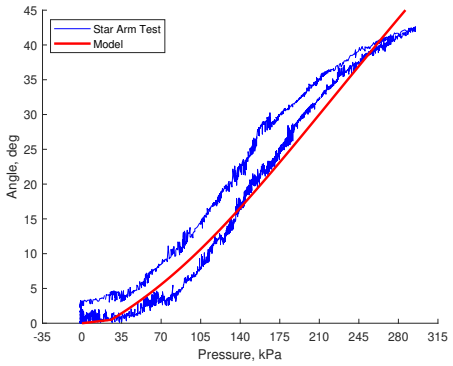

(c) 1134 g added weight

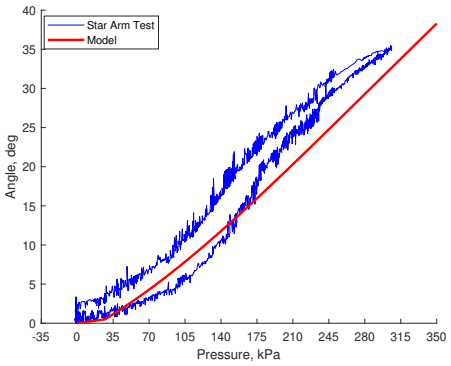

(d) 2268 g added weight

Figure 5.12: Pressure vs. Angle Comparisons

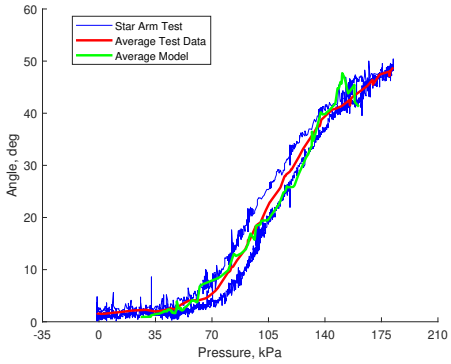

(a) No added weight

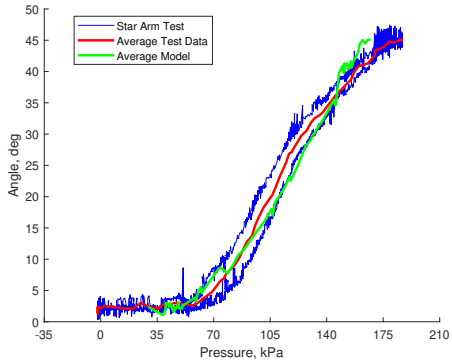

(b) 50 g added weight

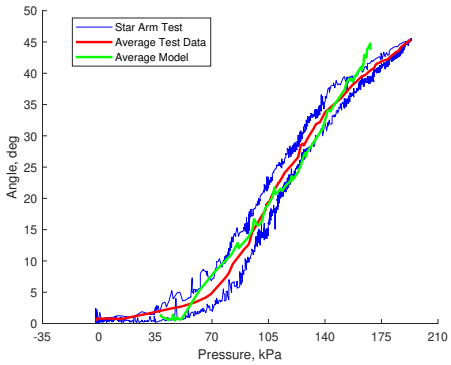

(c) 110 g added weight

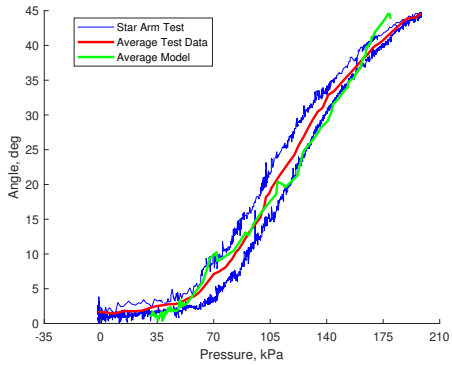

(d) 170 g added weight

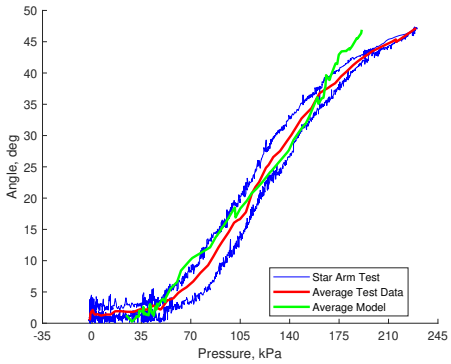

(e) 250 g added weight

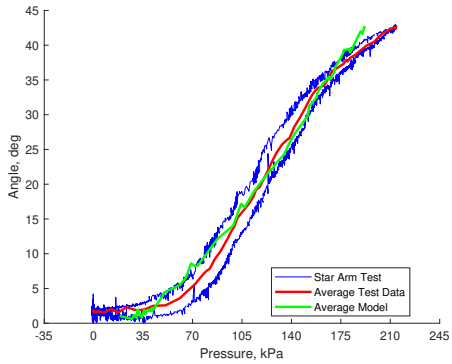

(f) 310 g added weight

Figure 5.13: Pressure vs. Angle Comparisons

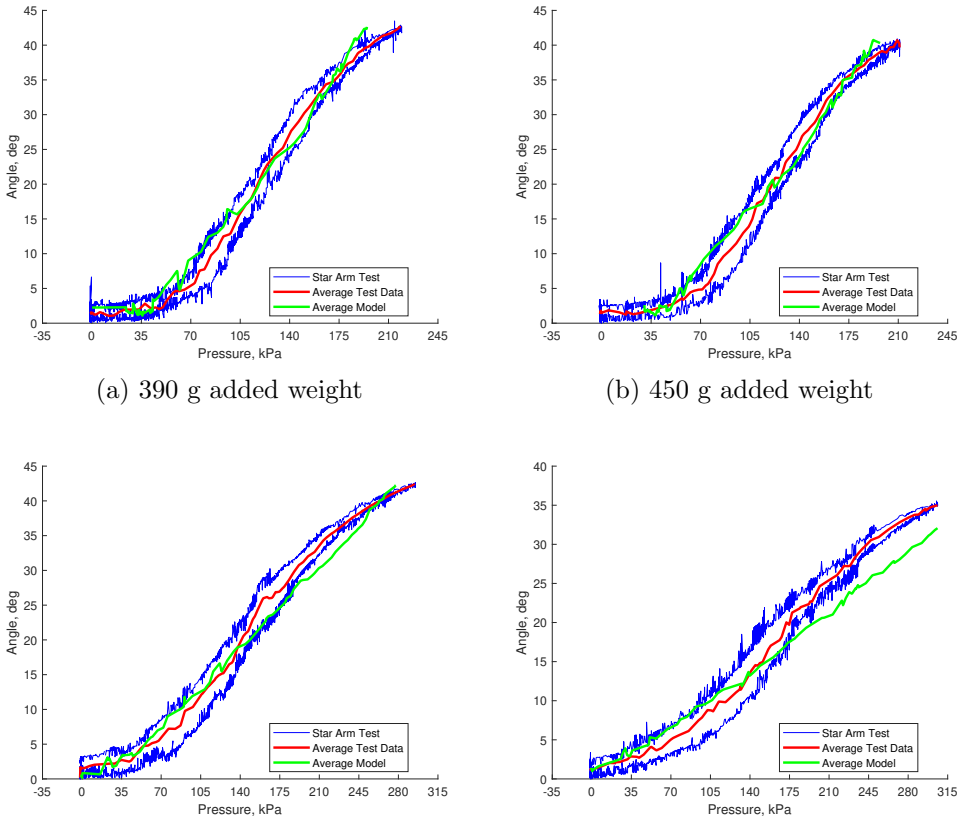

(a) 390 g added weight

(b) 450 g added weight

(c) 1134 g added weight

(d) 2268 g added weight

Figure 5.14: Pressure vs. Angle Comparisons

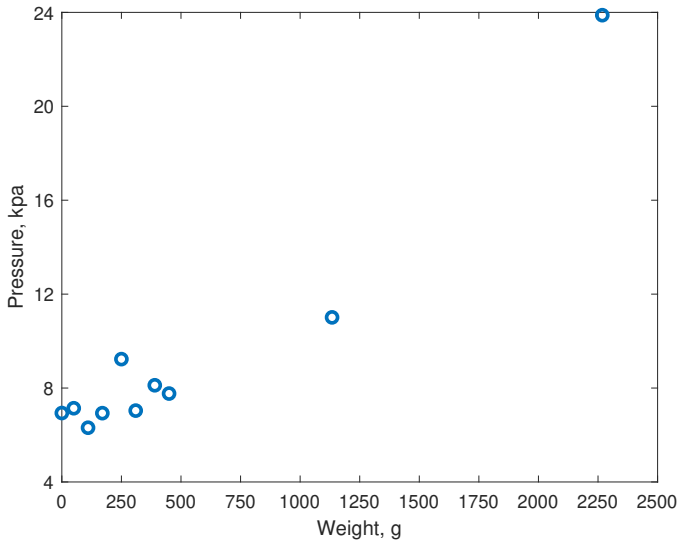

Figure 5.15: Average pressure error across the range of bending angles at each weight.

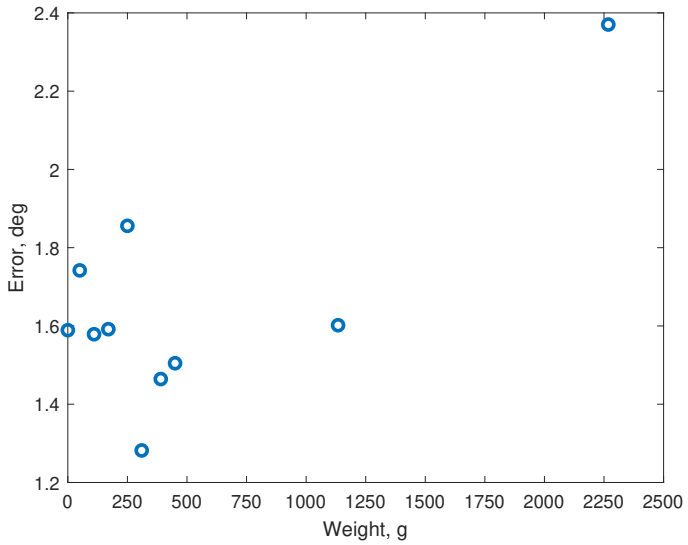

Figure 5.16: Average pressure error across the range of bending angles at each weight.

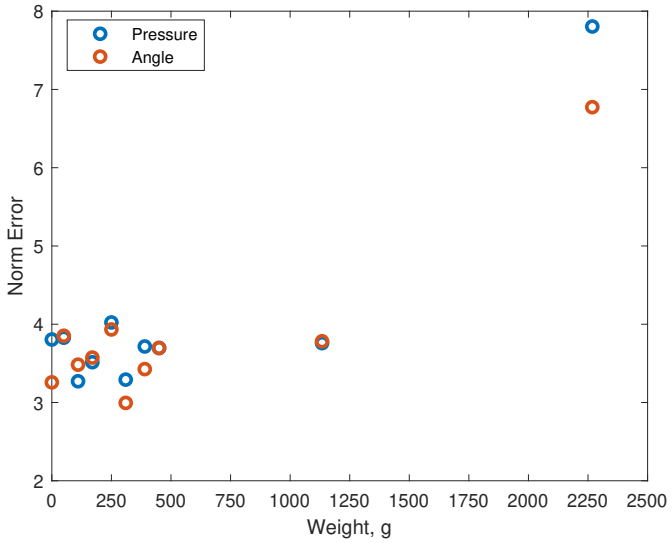

Figure 5.17: Average pressure error across the range of bending angles at each weight.

Chapter 6: Static Model of Multi-section Continuum Arm with Ossicles

6.1 Introduction

Soft robots are an emerging field of robotics which lack the rigid structure of traditional manipulators. Like hyper-redundant manipulators, soft robots are used for their flexibility and ability to conform to unexpected shapes. Soft robots have been used for crawling with smart material actuators [30] and grasping with pneumatic actuation such as the PneuNets [43] and pneumatic artificial muscles (PAMs) [47]. PAMs have been used in numerous rigid robot arms [102], legs [125], and non-robotic applications like trailing edge flaps [108].

Pneumatic artificial muscles are soft actuators composed of a braided sleeve surrounded by an elastomeric bladder, which either extends or contracts when pressurized [87]. The soft nature of PAMs makes them a natural choice for a soft robotic manipulator, having been used in soft robotic manipulators constructed of both extensile [29] and contractile [48] PAMs. Contractile PAMs were chosen in this work due to the higher force and work output they achieve [137]. A tendency of PAM actuated soft robotics arms is to deform in less desirable ways as a result of the

compliant nature of the inactive actuators. For example, the extensile PAM arm has points along the muscle groups connected to prevent this undesired motion [29]. To achieve a similar goal, structures similar in function to the ossicles found on brittle stars are added to the contractile PAM manipulator and evaluated.

In soft robotics there is interest in taking existing actuators and externally augmenting their structure to provide a new desired behavior. Galloway et al. added an exterior sleeve to the bending fiber-reinforced actuators to control and limit the bending to a subset of shapes, which can approach joint-like structures with certain sleeve designs. These actuators were incorporated into a gripper that could more securely grasp desired shapes such as boxes [41]. Deimel and Brock present a tapered pneumatic fiber-reinforced actuator, PneuFlex, used on a soft hand which can complete a variety of different grasps with five finger and two palm actuators [42]. Additionally, Galloway et al. developed two soft grippers comprised of fiber-reinforced hydraulic actuators for deep sea sampling [43]. The first is an actuator that couples bending and twisting by incorporating a single fiber reinforcement to wrap around an object, and the second takes the PneuNet bellows actuators and incorporates fiber reinforcements to increase the pressure capability.

Soft robot modeling is based on the hyper-redundant robot modeling approximation as a continuum [54]. This can be applied as a geometrically exact continuous model [58] or there can be simplifying assumptions, such as constant curvature [12]. Tatlicioglu et al. calculated the planar dynamic model using the constant curvature assumption for a three-section PAM manipulator. The model developed includes gravitational energy as well as the energy to extend and bend a

segment. The energies were integrated over each section of the arm to find the total energy and calculate the Lagrangian dynamics [65].

Constant curvature methods are calculated in terms of state variables of section curvature, bending plane, and length, but for a three actuator intrinsic manipulator, there is not direct control of these values. To develop models in terms of the control lengths and forces of the muscles, Godage et al. introduced shape functions based on the polynomial relationships between the length of the actuators for a PAM actuated continuum robot [66]. The expansions used in that work allow the mathematically singularity associated with a straight arm configuration to be avoided. This work was extended by considering the center of gravity of the section assumming uniform weight distribution. The formulation compared the total energy to both the integral and discretized formulations for a single section, applying a mass correction factor of 1/.57 [67].

This work investigates a three-section PAM manipulator and studies the effect of adding an ossicle-inspired backbone to the arm. For a single section the addition of ossicles has been shown to improve the load capabilities of a PAM actuated structure. The manipulator is tested through five different muscle combinations with five load conditions at each. The manipulator is also tested and modeled both with, and without, ossicles to evaluate the effect of adding this structure.

6.2 Constant Curvature Modeling

The manipulator modeled in this work has three bending sections connected at rigid plates, Fig 6.1. Each section has three PAMs which are offset by 120°. The section break between each section and at the end of the arm is defined by the rigid PAM end fittings and the rigid plate to which the PAM are secured. These rigid section dividers also serve as a point of measurement for the poses at the beginning and end of a section. The modeling done in this work used the constant curvature assumption in each bending section, and then calculates the center of masses for the section as well as the rigid section breaks. The energies at these center of masses are calculated to find the Lagrangian dynamics with respect to the PAM lengths. This work assumed the weight of each section is evenly distributed throughout that section. The ossicle weight is assumed to be part of the bending section, but no additional influence of the ossicles is modeled.

Figure 6.1: Three section arm with ossicles installed.

Constant curvature kinematics appear in the review by Webster [12]. The

constant curvature modeling equations are expressed for the position and orientation of section i, where section $i = 1$ is the proximal section. The rotation of the section is oriented so that the x-axis is in the same plane at the beginning and end of each section.

$$p_{CC_i}(s) = \begin{bmatrix} h_i \cos\phi_i \frac{1-\cos\theta_i s}{\theta_i} \\ h_i \sin\phi_i \frac{1-\cos\theta_i s}{\theta_i} \\ h_i \frac{\sin\theta_i s}{\theta_i} \end{bmatrix} \tag{6.1}$$

$$R_{CC_i} = \begin{bmatrix} \cos^2\phi_i \left(cos\theta_i - 1\right) + 1 & \sin\phi_i \cos\phi_i \left(\cos\theta_i - 1\right) & \cos\phi_i \sin\theta_i \\ \sin\phi_i \cos\phi_i \left(\cos\theta_i - 1\right) & \sin^2\phi_i \left(\cos\theta_i - 1\right) + 1 & \sin\phi_i \sin\theta_i \\ -\cos\phi_i \sin\theta_i & -\sin\phi_i \sin\theta_i & \cos\theta_i \end{bmatrix} \tag{6.2}$$

Expressions for the section length,l, bending angle θ, and plane of bending ϕ. A 2D representation of the proximal section orientation is shown in Fig. 6.2 with a point mass after $s = 1$ representing the concentration of mass of the section plate. For the distal section this mass would also include any added mass during experimental testing.

The bending plane expression changes based on the orientation of the PAMs relative to the section definition. The derivation method of ϕ for different PAM orientations can be found in the Constant Curvature Review [12]. The first and third section have PAM $i1$ on the positive x-axis, and the second section has PAM

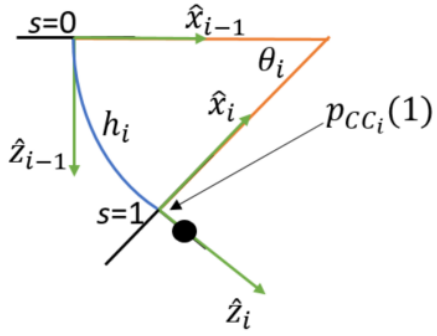

Figure 6.2: Single section orientation used in this work. Gravity acts in the positive $\hat{z_0}$ direction and ϕ_i is a rotation about $\hat{z_{i-1}}$.

$i2$ on the negative x-axis.

$$h_i = h_{i0} + \frac{l_{i1} + l_{i2} + l_{i3}}{3} \tag{6.3}$$

$$\theta_i = \frac{2\sqrt{l_{i1}^2 + l_{i2}^2 + l_{i3}^2 - l_{i1}l_{i2} - l_{i1}l_{i3} - l_{i2}l_{i3}}}{3r_i} \tag{6.4}$$

$$\phi_{i=1,3} = \tan^{-1}\left(\frac{\sqrt{3}\,(l_{i2} - l_{i3})}{(l_{i2} + l_{i3} - 2l_{i1})}\right) \tag{6.5}$$

$$\phi_{i=2} = \tan^{-1}\left(\frac{\sqrt{3}\,(l_{i3} - l_{i1})}{(2l_{i2} - l_{i3} - l_{i1})}\right) \tag{6.6}$$

Identities for $sin(tan^{-1})$ and $cos(tan^{-1})$ can be used to rewrite the expressions in terms of PAM lengths and remove a number of the trigonometric functions from the expressions for position and orientation.

$$\sin(\phi_i) = \sin\left(\tan^{-1}\frac{y_i}{x_i}\right) = \frac{y_i}{\sqrt{x_i^2 + y_i^2}} \tag{6.7}$$

$$\cos(\phi_i) = \cos\left(\tan^{-1}\frac{y_i}{x_i}\right) = \frac{x_i}{\sqrt{x_i^2 + y_i^2}} \tag{6.8}$$

$$\sqrt{x_i^2 + y_i^2} = 2\sqrt{l_{i1}^2 + l_{i2}^2 + l_{i3}^2 - l_{i1}l_{i2} - l_{i1}l_{i3} - l_{i2}l_{i3}} = 3r_i\theta \tag{6.9}$$

$$p_{CC_i}(s) = \begin{bmatrix} \frac{h_i x_i}{3r_i}\frac{1-\cos\theta_i s}{\theta_i^2} \\ \frac{h_i y_i}{3r_i}\frac{1-\cos\theta_i s}{\theta_i^2} \\ h_i\frac{\sin\theta_i s}{\theta_i} \end{bmatrix} \tag{6.10}$$

$$R_{CC_i} = \begin{bmatrix} 1 + \frac{x_i^2}{9r_i^2}\frac{\cos\theta_i - 1}{\theta_i^2} & \frac{x_i y_i}{9r_i^2}\frac{\cos\theta_i - 1}{\theta_i^2} & \frac{x_i}{3r_i}\frac{\sin\theta_i}{\theta_i} \\ \frac{x_i y_i}{9r_i^2}\frac{\cos\theta_i - 1}{\theta_i^2} & 1 + \frac{y_i^2}{9r_i^2}\frac{\cos\theta_i - 1}{\theta_i^2} & \frac{y_i}{3r_i}\frac{\sin\theta_i}{\theta_i} \\ -\frac{x_i}{3r_i}\frac{\sin\theta_i}{\theta_i} & -\frac{y_i}{3r_i}\frac{\sin\theta_i}{\theta_i} & \cos\theta_i \end{bmatrix} \tag{6.11}$$

A Taylor expansion can be performed on the resulting functions of θ leaving the pose of the section in terms of only the PAM lengths. These expressions are differentiable and can be used to find the velocities of the center of gravities of the soft section as well as the rigid end plates.

The center of mass of a section can be found by integrating the position through the section, the integrals of these Taylor expandable functions can be used to find the position with a polynomial function of PAM lengths. The center of mass formulation is inspired by the work of Godage et al. [67], but this work separates the effect of the break between sections where a large amount of the mass is located from the

continuously bending lightweight PAM section.

$$\beta_i = \int_0^1 p_{CC_i} ds = \begin{bmatrix} \frac{h_i x_i}{3r_i} \int_0^1 \frac{1-\cos\theta_i s}{\theta_i^2} \\ \frac{h_i y_i}{3r_i} \int_0^1 \frac{1-\cos\theta_i s}{\theta_i^2} \\ h_i \int_0^1 \frac{\sin\theta_i s}{\theta_i} \end{bmatrix} \tag{6.12}$$

$$\frac{1-\cos\theta_i s}{\theta_i^2} = -\frac{s^2}{2} + \frac{\theta_i^2 s^4}{24} - \frac{\theta_i^4 s^6}{720} + O(\theta_i^6 s^8) \tag{6.13}$$

$$\frac{\sin\theta_i s}{\theta_i} = s - \frac{\theta_i^2 s^3}{6} + \frac{\theta_i^4 s^5}{120} + O(\theta_i^6 s^7) \tag{6.14}$$

The positions of the center of masses of the bending sections, p_{β_i}, and non-bending section breaks, p_{M_i} can be found with the following equations, where p_i is the end of the i^{th} bending section and section divider, and $p_{M_{lcl_i}}$ is the position of the end of the section divider with respect to the end of the previous section.

$$p_i = p_{CC_i}(1) + R_{CC_i} p_{M_{lcl_i}} \tag{6.15}$$

$$p_{\beta_1} = \beta_1 \tag{6.16}$$

$$p_{\beta_2} = p_1 + R_{CC_1}\beta_2 \tag{6.17}$$

$$p_{\beta_3} = p_1 + R_{CC_1} p_2 + R_{CC_1} R_{CC_2}\beta_3 \tag{6.18}$$

$$p_{M_1} = p_{CC_1}(1) + \frac{1}{2} R_{CC_1} p_{M_{lcl_1}} \tag{6.19}$$

$$p_{M_2} = p_1 + R_{CC_1} p_{CC_2}(1) + \frac{1}{2} R_{CC_1} R_{CC_2} p_{M_{lcl_2}} \tag{6.20}$$

$$p_{M_3} = p_1 + R_{CC_1} p_2 + R_{CC_1} R_{CC_2} p_{CC_3}(1) + \frac{1}{2} R_{CC_1} R_{CC_2} R_{CC_3} p_{M_{lcl_3}} \tag{6.21}$$

From these equations the velocities can be determined. From the position and velocity expressions the kinetic energy, T and potential energy, V can be calculated to solve for the Lagrangian dynamics.

$$T_E = \frac{1}{2}\sum_{i=1}^{3} \dot{p}_{\beta_i}^T m_i \dot{p}_{\beta_i} + \frac{1}{2}\sum_{i=1}^{3} \dot{p}_{M_i}^T M_i \dot{p}_{M_i} \tag{6.22}$$

$$V_E = \left(p_{\beta_1} m_1 + p_{\beta_2} m_2 + p_{\beta_3} m_3 + p_{M_1} M_1 + p_{M_2} M_2 + p_{M_3} M_3\right)^T \begin{bmatrix} 0 \\ 0 \\ g \end{bmatrix} \tag{6.23}$$

The governing equation of motion is thus

$$[M(l)]\ddot{l} + [C_D(l,\dot{l})]\dot{l} + G(l) = F(L_0 l, P) \tag{6.24}$$

where $[M(l)]$ is the mass matrix, $[C_D(l,\dot{l})]$, is the damping matrix, $G(l)$ is the vector of forces from potential energy specifically gravity, $F(l,P)$ is the vector of forces output from the PAMs, and l is the vector of the change of length of the PAMs starting with the proximal section. The PAM force is modeled using the force balance model with non-linear bladder stiffness detailed in Chapter 2.

The kinetic energy can be rearranged using the Jacobian relates the PAM velocities to the center of masses velocities of the respective sections. Equation 6.22 can be rearranged to be written in terms of the PAM velocity vector, $\dot{l}$, and the

Jacobians which relate $\dot{l}$ to $\dot{p}_{\beta_i}$ and $\dot{p}_{M_i}$

$$T_E = \frac{1}{2} \dot{l}^T \left(\sum_{i=1}^{3} J_{\beta_i}^T m_i J_{\beta_i} + \sum_{i=1}^{3} J_{M_i}^T M_i J_{M_i} \right) \dot{l} \tag{6.25}$$

From the partial derivative of Lagrangian with respect to the vecolicty, the mass matrix, M, can be determined,

$$[M(l)] = \sum_{i=1}^{3} J_{\beta_i}^T m_i J_{\beta_i} + \sum_{i=1}^{3} J_{M_i}^T M_i J_{M_i} \tag{6.26}$$

the damping matrix, C, can be determined from the partial derivate of the kinetic energy with respect to the length. Each entry in this matrix can be calculated with the Christoffel symbols, Γ_{ijk},

$$C_D(l, \dot{l})_{ij} = \sum_{k=1}^{n} \Gamma_{ijk} \dot{l}_k = \frac{1}{2} \sum_{k=1}^{n} \left(\frac{\partial M_{ij}}{\partial l_k} + \frac{\partial M_{ik}}{\partial l_j} - \frac{\partial M_{kj}}{\partial l_i} \right) \dot{l}_k \tag{6.27}$$

the partial derivative of the mass matrix can applied to each section independently. For example using the center of mass of the first section

$$[M_{m_1}(l)] = m_1 J_{\beta_1}^T J_{\beta_1} \tag{6.28}$$

$$\frac{\partial M_{m_1}}{\partial l_j} = m_1 \left(H_{\beta_{1_j}}^T J_{\beta_1} + J_{\beta_1}^T H_{\beta_{1_j}} \right) \tag{6.29}$$

$$H_{\beta_{1_j}} = \frac{\partial J_{\beta_1}}{\partial l_j} \tag{6.30}$$

Finally, the gravity vector, G, can be determined from the partial derivative of the

potential energy with respect to the PAM length,

$$G = \frac{\partial V_E}{\partial l} = (J_{\beta_1} m_1 + J_{\beta_2} m_2 + J_{\beta_3} m_3 + J_{M_1} M_1 + J_{M_2} M_2 + J_{M_3} M_3)^T \begin{bmatrix} 0 \\ 0 \\ g \end{bmatrix} \quad (6.31)$$

Additional sources of potential energy not captured by the PAM force model such as the bending energy to bend pressurized PAMs could be further investigated to improve the model fit if necessary.

Dynamic validation will be required in the future, but as a initial step quasi-static validation of this model will be conducted using the arm with ossicles. The arm with ossicles will also be compared ossicle-free arm.

6.3 Testing of Ossicle Arm

The three section arm with three PAMs per section was experimentally evaluated with and without an ossicle-inspired structure running the length of each section. The arm was tested in five configurations that sweep out all the single muscle per section motions. For evaluating the performance, any additional single muscle combinations are mirrored by the ones tested in this study. The PAMs were manually pressurized beginning with the most distal section, then the medial section and finally the proximal section. The depressurization was done in the reverse order, proximal, medial, then distal. The order was chosen to minimize effects of

unactuated PAMs in the more distal sections. The series of test were conducted with and without ossicles. The distal sections of the appendage have been previously compared by considering the angle achieved at the end of the section under load, but this comparison is complicated for multi-section appendages due to differences in the behavior of distal sections effecting the proximal sections. To compare the two cases the area traced by the tip will be compared at each load case. This captures the cumulative effect of the ossicles throughout the arm.

6.3.1 Model Validation

To validate the modeling techniques the average pressure versus angle was compared to the average modeled pressure for that angle. The average error was calculated separately for each section and load case and averaged over the five tests. The model output was calculated using the positions and PAM length determined from the experimental data. The model performs best for low loads and more distal sections, Fig. 6.3. Figure 6.4 shows the modeling results for the distal section with no weight and the medial section with the max test load of 250 g.

For the proximal section, there seems to be two different situations causing the increased errors. During the tests where the medial section acts in a different plane than the proximal section, the proximal section appears to deviate from the model around a moment of 0.825 in-lb. This moment is determined from the planar distance of the load to the base of the section. The increase in pressure with the bending angle can be related to the difference of the final plane of bending and the

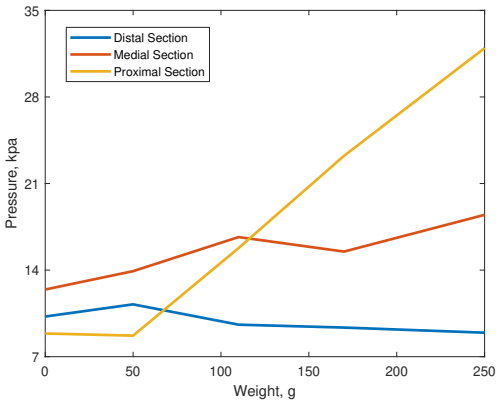

(a) Average error in pressure during testing.

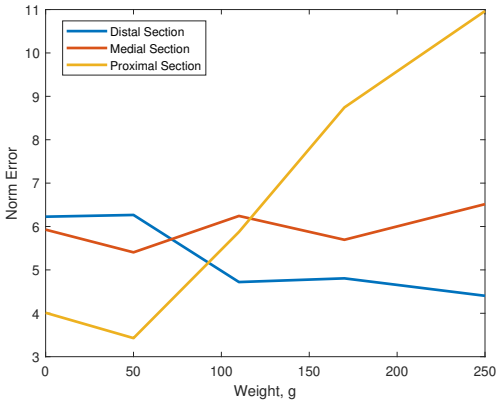

(b) Average normalized pressure error during testing.

Figure 6.3: Modeling errors for all five test cases across all five loading conditions.

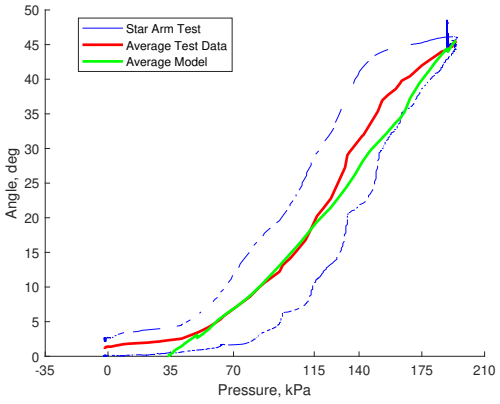

(a) Angle pressure relationship for the distal section with no load.

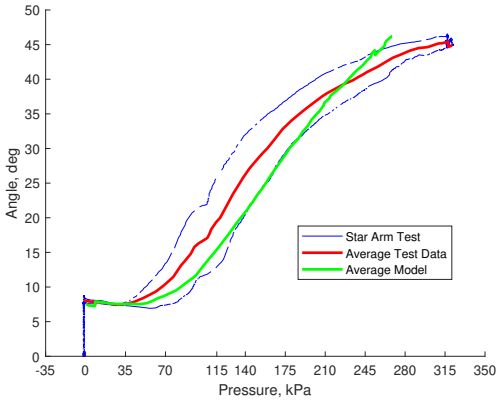

(b) Angle pressure relationship for the medial section with 250 g of weight.

Figure 6.4: Example of modeling results for two test cases.

plane of the actuated PAM, Figure 6.5. After adding this linear pressure increase model the resulting errors are reduced, Fig. 6.6, and and example of the application of the model to one of the test cases is shown, Fig. 6.7.

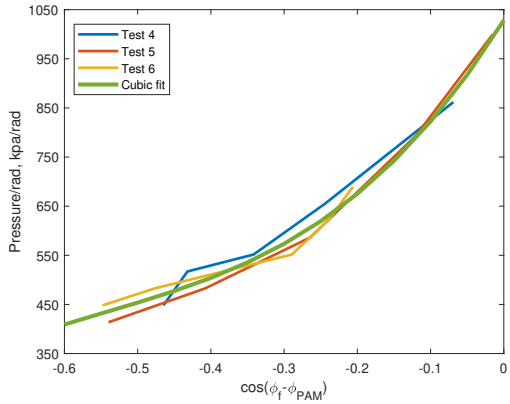

Figure 6.5: Increase of pressure with chosen moment has been reached.

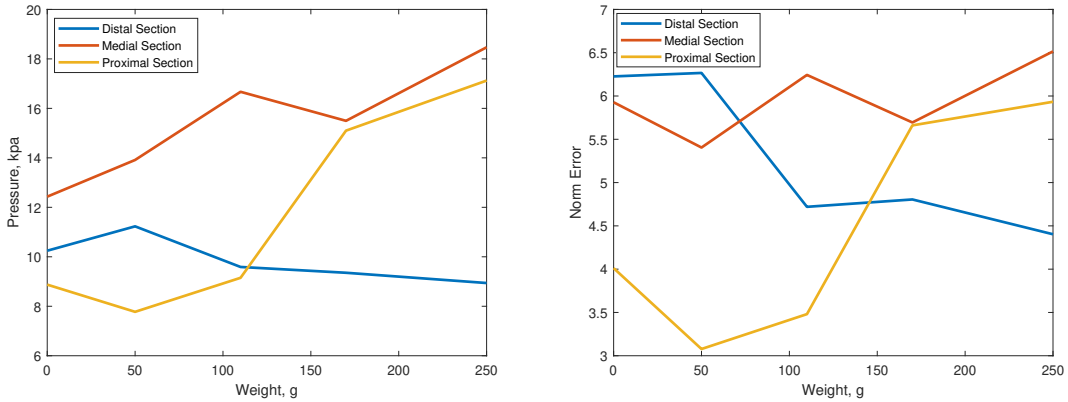

(a) Average error in pressure during testing. (b) Average normalized pressure error during testing.

Figure 6.6: Modeling errors for all five test cases across all five loading conditions with linear pressure increase in the third section.

The ossicle structure was designed to interact and limit bending at approximately 45°, a similar model could be incorporated at angles above the design value to improve the model at high angles for the medial and distal sections. To improve modeling and reduce the effects of non-active PAMs, the ossicle structure could be

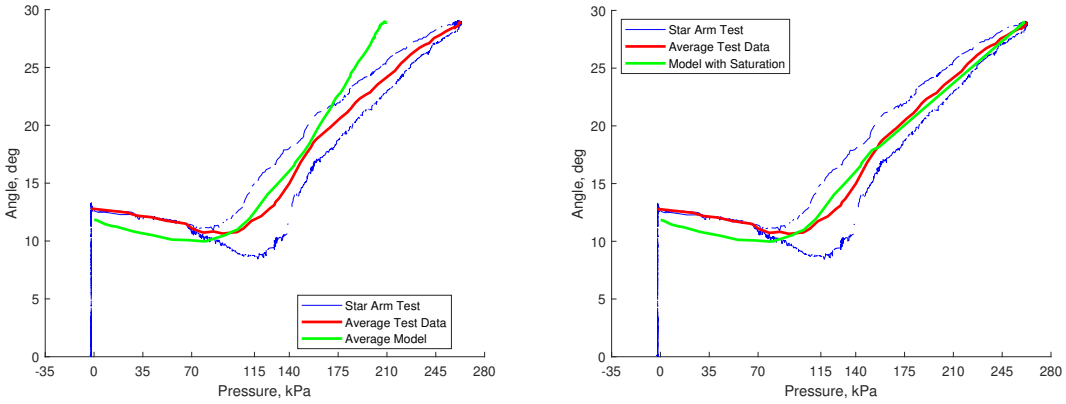

(a) Angle pressure relationship for the proximal section with 110 g of weight at the tip.

(b) Angle pressure relationship for the proximal section with 110 g of weight at the tip and linear pressure model included .

Figure 6.7: Comparison of modified model in the proximal section model on the 110 g loading case of Test 6.

sized such that the PAMs are contracted and pressurized when in a straight arm position, allowing the initial stiffness of the system to be tailored to the desired application. Additionally operation in environments which reduce gravitational impact, space or water, would be beneficial. One way to improve model fitting is improving PAM modeling in the low force and pressure regime. Solutions include a low and high pressure model, higher order PAM modeling or additional considerations of effects on PAM behavior, such as bending.

6.3.2 Effect of Ossicles

To study the effect of adding ossicles to the arm, the five motions which were tested can be rotated by 120° and 240° to represent the same combination of muscles for the other two proximal section PAMs. Four of the motions are non-planar and can be reflected about the plane of the proximal PAM, and then rotated for

the remaining twelve motions. This procedure generates all 27 combinations of one active PAM per section. The procedure to track the tip position of the arm for a single motion is shown in a top down view in Fig. 6.8.

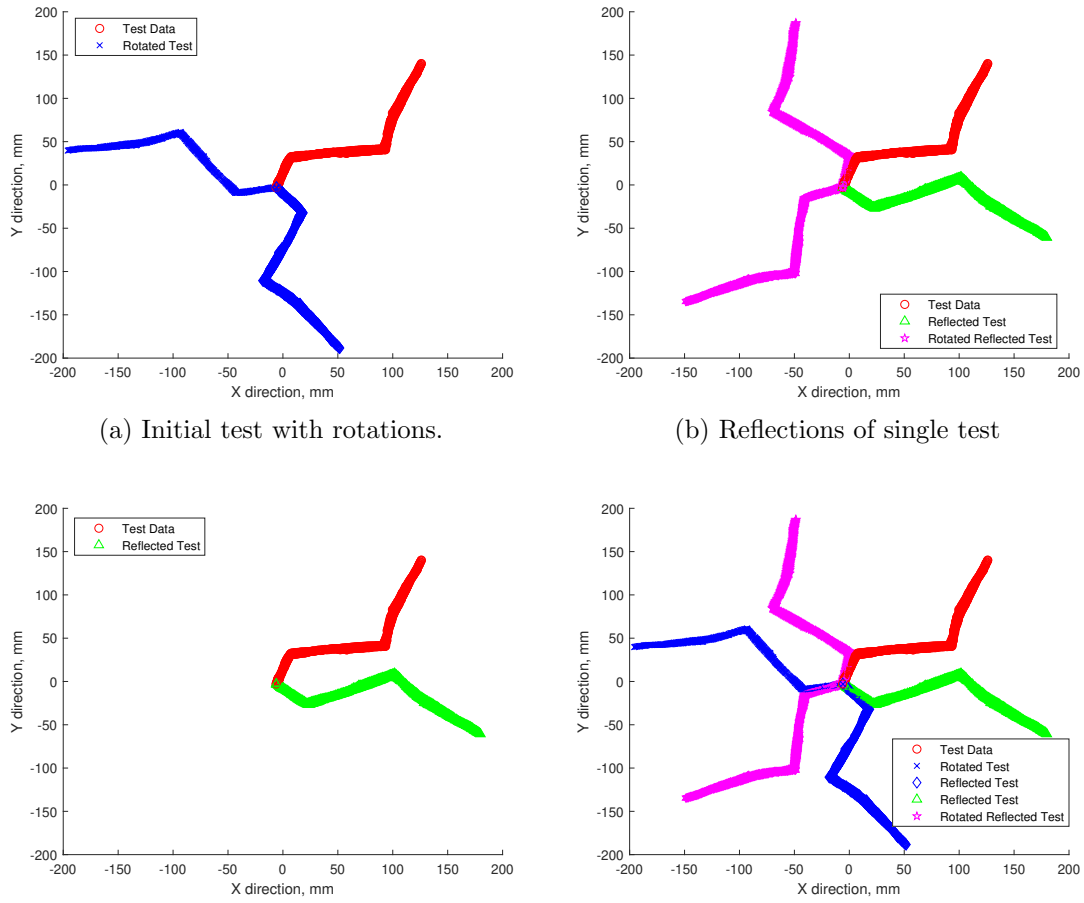

(a) Initial test with rotations.

(b) Reflections of single test

(c) Reflections of single test

(d) Six resulting curves for a single test

Figure 6.8: Procedure to construct other tip traces for untested muscle combinations.

This procedure was applied to both the ossicle and non-ossicle tests for each of the five loading conditions resulting in a cone-like shape for each case as seen in Fig. 6.9. The test were conducted with the arm hanging as in Fig. 6.1, but this is displaced with the arm tip up in the following images for increased clarity of the overall shape.

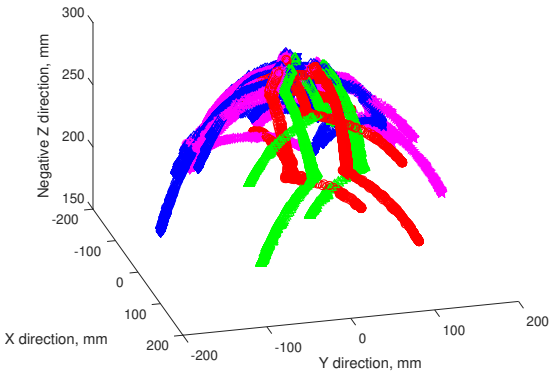

(a) Zero Load Test without ossicles.

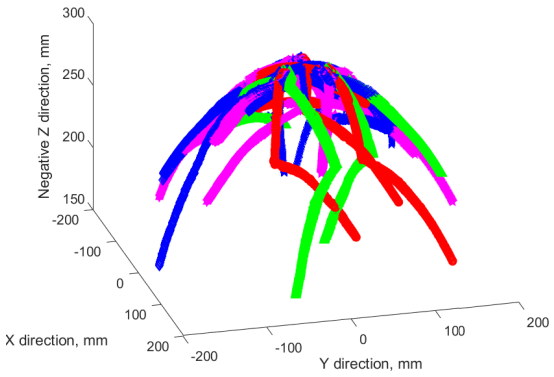

(b) Zero Load Test with ossicles

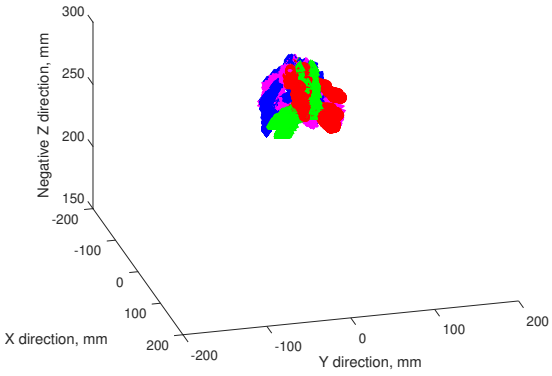

(c) 250 g Load Test without ossicles.

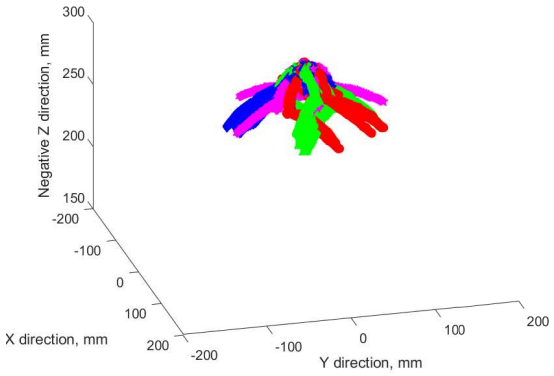

(d) 250 g Load Test with ossicles

Figure 6.9: Three dimensional view of test results for no load and highest load 250 g. Colors are consistent with Fig. 6.8, red is original data, blue is the original data rotated , green is the original data reflected, and magenta is the original reflected and rotated data.

Ossicles have been shown to improve the load capacity of a single section PAM soft robot. To compare the cumulative effect of ossicles in each section, we consider the X-Y planar projection of Fig. 6.9. This projection will be used to bound the area reached by the arm to compare the effect of adding ossicles. The boundary enclosing these curves were found using a shrink factor of $s = .091$. This shrink factor was chosen by performing a sweep of shrink factors from $s = 0$ to $s = 1$, where $s = 0$ represents a convex hull of the set of points. The chosen shrink factor provided the minimum area ratio for the unloaded test case. The planar projections for the zero load and 250 g load cases are show in Fig. 6.10, The ratio of the areas comparing the effect of adding ossicles to the soft structure is shown for all five load cases in Fig. 6.11. The average area ratio in the no load case of the sweep conducted was 1.15.

6.4 Conclusions

In this work a three section, nine PAM soft robotic manipulator constructed, modeled, and tested. This manipulator was tested with five different muscles combinations and five load cases to study the static model and effect of adding a bio-inspired ossicle structure. The constant curvature center of mass model developed was shown to work best at low loads and for the more distal sections. The model was substantially improved when including a linear increase in pressure above a chosen moment level the proximal section. Improvements to PAM modeling and ossicle design should help improve the static modeling especially for the proximal section.

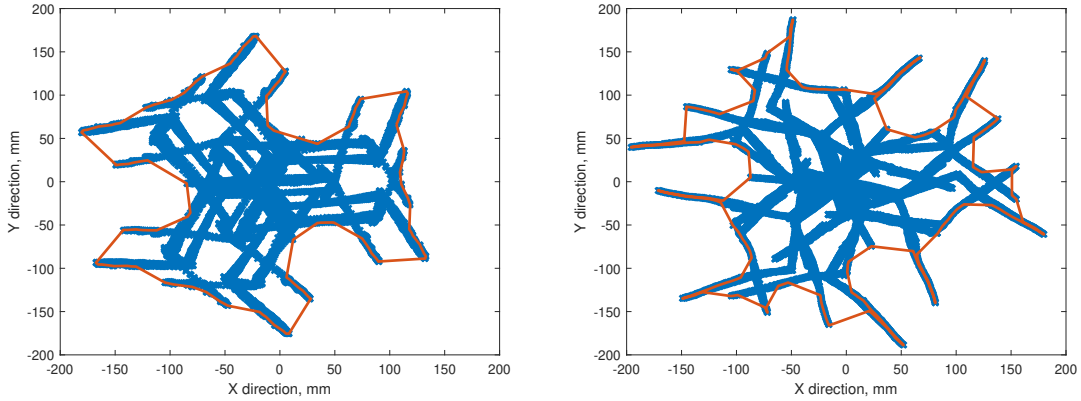

(a) Zero Load Test without ossicles.

(b) Zero Load test with ossicles

(c) 250 g Load Test without ossicles.

(d) 250 g Load test with ossicles

Figure 6.10: Planar view of test results for no load and highest load 250 g. Colors are consistent with Fig. 6.8, red is the boundary for the given shrink factor, blue is the processed data.

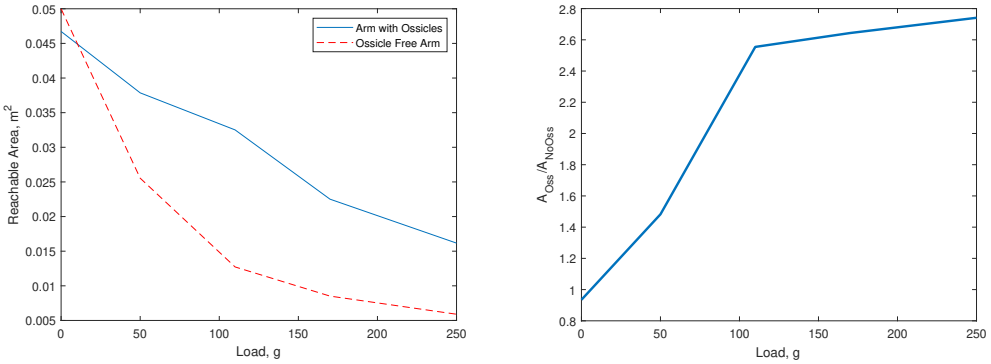

(a) Bounded area for each load case with and without ossicles.

(b) Ratio of bounded area of the ossicle test case compared to the no ossicle test case.

Figure 6.11: Effect of load on ossicle structure.

Overall the addition of ossicles improved the ability of the manipulator to handle loads placed at the tip. When 250 g were hung from the end of the arm the arm with ossicles was able to reach an area 2.6 times greater than the ossicle-free arm.

Chapter 7: Conclusion

7.1 Summary of Research and Key Conclusions

This research investigated the behavior of PAMs and their application to soft robotics. Silicone rubber PAM bladders were fabricated to study the effect of bladder material and thickness on actuator performance. Thinner bladders provide better performance until using a thinner bladder would lead to premature rupture between the fibers of the braid. PAM modeling can be improved by including pressure dependence in the stress-strain relationship of the bladder for empirical models, or using Mooney-Rivlin material models can lead to predictive PAM models provided the materials testing for cylindrical rubber tubing can be performed. Contractile and extensile PAMs were studied experimentally and parametrically modeled to understand when to use each type of muscle. Contractile muscles are better with blocked force nearly an order of magnitude greater for the same diameter produce 50% higher work densities, while extensile muscles are best when the load is low and large motions relative to the length of the actuator, greater than 30% are required. Contractile PAMs were chosen to construct a soft robotic arm. This arm was modeled assuming constant curvature through the bending sections, soft PAM bladder, along with the inactive section dividers where the PAMs attach. The model considered the

mass of these two section types separately. This modeling technique was effective for PAM sections provided the applied moment did not become too large. These soft robotic sections also included bio-inspired ossicles to improve the load performance and reduce the effects of unpressurized PAMs.

7.1.1 Pneumatic Artificial Muscle Bladder Wall Thickness Effects

The first section of this research studied different materials and bladder wall thicknesses for miniature PAMs. Commercial bladders were tested and found to produce force or contraction less than that expected resulting from scaling down larger PAMs in a model. A soft thin bladder was fabricated to show that material and not scale was the cause of this decreased performance. With this insight a set of bladders were fabricated with constant outer diameter and varying wall thickness. These bladders were used to study the effect of bladder thickness on PAM performance. This study showed that increased bladder thickness led to increased dead-band pressure and decreased blocked force and free contraction.

7.1.2 Pneumatic Artificial Muscle Modeling

Using the experimental data from the set of miniature PAMs studied for bladder thickness effects two PAM models were developed. The fully empirical model expanded on previous models which included a polynomial stress-strain relationship unique to each pressure by introducing a linear variation of the parameters with pressure. This change allows for better model performance at untested or unmodeled

pressures. The second model was developed using a solid mechanics approach and a Mooney-Rivlin model for the bladder material modeling. This model was validated for two scales of PAMs, and should allow for future predictive PAM model application once a test is developed to capture the Mooney-Rivlin behavior of cylinders. Both of these models were developed for contractile PAMs then later extended to extensile PAMs.

7.1.3 Comparison of Extensile and Contractile Pneumatic Artificial Muscles

Fabricated large extensile and contractile PAMs then used that sizing to determine scale for a smaller contractile and extensile PAMs. After experimentally testing and modeling the PAM behavior a parametric study was done to investigate the effects of varying diameter and braid angle of both types of PAMs. The models were varied for both scales to ensure the material effect of the two scales were minimized. Varying diameter was shown to have no effect of work density or efficiency for each type of PAM, assuming the material properties were unchanged with scale. Choosing a braid angle for either type of PAMs closer to the extremes, 0° for extensile and 90° for contractile, increased work, stroke and efficiency. As the braid angle moves towards the extremes, contractile PAMs produce higher work density and efficiency, while extensile PAMs have greater strokes and reduced volumes. These finding were used to inform the choice of contractile PAMs for use in the soft robotic arm.

7.1.4 Soft PAM Arm Modeling

A three-section PAM arm was fabricated and modeled using the assumption of constant curvature in the bending sections. Both a single section and the entire arm were modeled and compared to experimental values. The constant curvature model used a change a variables to write the positions in terms of PAM lengths and used the center of gravity to model the energy in the bending sections. This formulations allows the required forces to be modeled directly as the PAM force or pressure, and introduce a Taylor expansion to avoid the mathematical singularity when the arm is straight. The model was validated for the distal and medial sections, but required an additional term when at high moment, high relative load, cases in the proximal section of the arm. All the model validation was done for the arm structure after the introduction of bio-inspired ossicle structures, assuming distributed weight, but no additional interaction with the system.

7.1.5 Introduction of Ossicles

Drawing inspiration from brittle stars, an ossicle-like, or backbone like structure, was incorporated into each bending section of the PAM arm. The ossicles were designed to interact at a chosen angle at which point additional bending would require greater force, but stiffness would be increased. The effects of the ossicles were shown for both a single section as well as the three section arm. For a single section, the introduction of ossicles decreased required pressure and increased the angle which could be achieved as the section was loaded. To study the cumulative effect

of ossicles, the reach of the arm with every single muscle per section combination was considered. The planar area enclosed by the tip with and without ossicles was compared to study how ossicles effect the load capability of the whole arm. For no loading, the ossicle have little effect to a small negative impact, but that impact is offset but the increased capacity of the arm as it is loaded.

7.2 Contributions to Literature

This dissertation makes a number contributions to the pneumatic artificial muscles and soft robotics literature. In the area of PAM experimentation and modeling two improved PAM force modeling techniques were developed, extensile PAMs were experimentally characterized across the full force extension range, and the existing PAM models were shown to be applicable to extensile PAMs. The polynomial stress-strain bladder model developed included a linear pressure dependence to improve the interpolation to intermediate (untested) pressures creating a more generalizable model after a PAM has been experimentally characterized. This model achieved errors of less than 5% with only 4 fit parameters compared to the 4 fit parameters per pressure for previous accurate models. The Mooney-Rivilin bladder model applied solid mechanics to PAM modeling achieving errors of less than 5% with two parameters which could be determined experimentally for a predictive model. Additionally, extensile PAMs were experimentally characterized to capture not only the blocked force and free extension, but the complete force-extension relationship at multiple pressures. These were the first force-extension curves shown

in literature, and the methodology used to obtain this data can be used by future researchers to analyze these actuators to improve their use in soft robotics and other applications. The previous developed models were shown to also model extensile PAMs, demonstrating that additional contractile PAM models should be applicable to extensile PAMs and predictive models like the one developed could reduce the need for more complicated extensile PAM testing.

The second research area focused on in this work was the application of PAMs to soft robotic structures. Metrics such as cycle work density were shown to capture the differences between extensile and contractile PAMs to help determine which actuator to apply to a system in development. The comparison of cycle work density was shown to capture the same trends as considering the work or stroke achieved for a chosen load. Using this framework, a soft robotic arm was constructed with contractile PAMs which was then modeled. This model applied conventional constant curvature in the bending section, but included an additional consideration for the rigid non-bending section dividers. This model was shown to be effective in low load situation for the one section and the full, three section arm, similar to low gravity environments where these soft manipulators will see the most use. This work showed the first use of an ossicle-inspired structure in contractile PAM soft robotics and demonstrated the advantage of using them. For a single section, introducing ossicles increased the load capacity from 500 g to 2258 g while bending 30°. For the three section arm, these ossicle-inspired structures allowed the soft arm to reach 2.6 times more area with 250 g of load while still reaching 95% of the unloaded area.

7.3 Future Work

The next steps in this research involve further investigations into PAM behavior and improved modeling and design of soft robotics. The Mooney-Rivlin bladder model was shown to be effective when choosing Mooney-Rivilin coefficients to match experimental data, but a method to study the Mooney-Rivilin coefficients of cylindrical rubber tubes needs to be developed to validate the predictive application of this PAM force modeling. Additional considerations which would be of interest to their use in soft robotics such as the effects on PAM force when undergoing bending. Preliminary studies of unpressurized PAMs showed minimal effects, but if multiple PAMs are pressurized to control soft robotic manipulator stiffness this behavior may become more important. Any improved PAM modeling will be beneficial to further develop the contractile/extensile PAM framework directly to the design of soft robotic manipulators. One open question which could be answered is does constructing an arm from a single muscle type (contractile or extensile) or mixed muscle types (contractile and extensile) improve performance of the arm. Additionally, for soft robotic manipulator design the ways to incorporate ossicles to achieve the desired behavior should be investigated. Possibilities include fewer or shorter ossicles such that the PAMs are contracted in the straight arm configuration allowing increasing control over the section compliance. Another way to achieve this goal could be to introduce a fourth muscle leading to a redundant actuator. The ossicle structure could also be modified to produce new motion and need not necessarily be radially symmetric. There are numerous modeling improvements that could be investigated

including relaxing the assumptions of constant curvature or more fully incorporating the ossicles into the model, and the addition of other load cases such as those arising from whole arm manipulation or grasping. For closed loop control, the method to sense the length and pressure on-board the arm or robot will be required.

Appendix A: Modeling Errors from Pneumatic Artificial Muscle Bladder Thickness Modeling

On the following pages the modeling errors for both bladder models E_1,E_3 and E_1,E_4 at every pressure are shown.

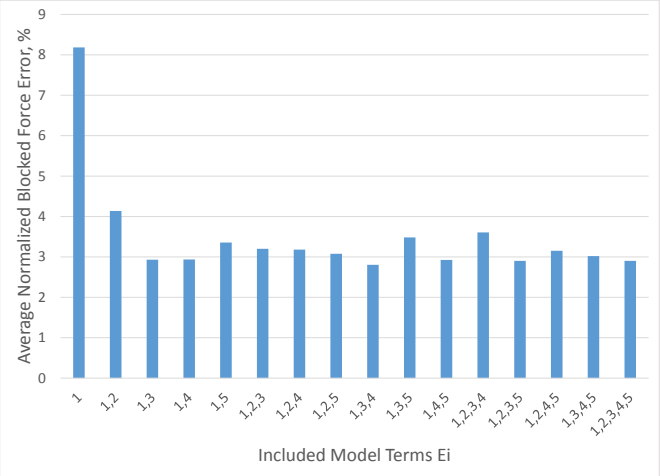

Figure A.1: Average Normalized Blocked Force Error

Table A.1: Blocked Force Percent Error

V_B/V	0.75		0.695		0.64		0.58		0.438	
Model:E_1 & E_i	i=3	i=4	i=3	i=4	i=3	i=4	i=3	i=4	i=3	i=4
69 kPa	12.16	10.33	17.43	17.19	19.48	20.84	0.60	1.62	6.61	5.87
138 kPa	5.40	3.35	7.24	5.82	4.98	6.29	0.81	0.32	2.00	1.15
206 kPa	4.87	2.79	5.10	3.47	3.70	5.04	3.91	2.78	0.08	0.99
276 kPa	2.76	0.63	3.33	1.57	0.71	2.03	3.87	2.72	2.29	1.38
345 kPa	1.79	0.36	2.92	1.12	0.10	1.43	0.66	1.87	0.09	0.86
414 kPa	1.55	0.61	1.73	0.13	1.84	0.53	0.45	0.75	1.71	2.69
483 kPa	0.09	2.29	1.37	0.51	0.65	0.67	2.42	1.23	0.14	1.11
552 kPa	0.33	1.86	0.06	1.99	0.13	1.21	0.22	1.00	0.07	1.04
621 kPa	1.91	4.16	1.44	3.40	0.63	0.70	1.61	2.85	0.68	1.66
Average	3.43	2.93	4.51	3.91	3.58	4.31	1.62	1.68	1.52	1.86

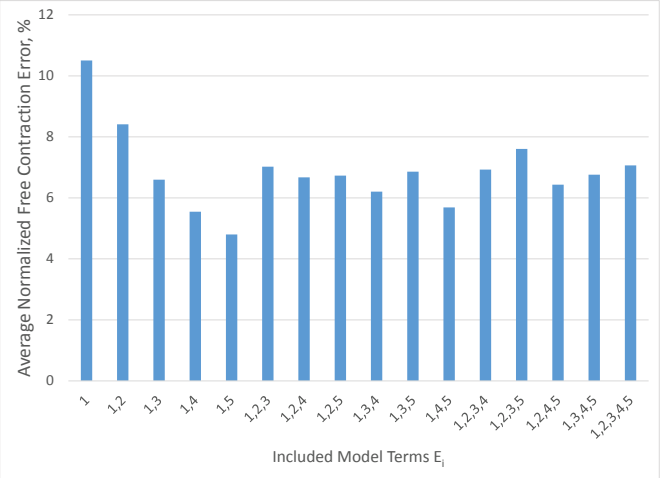

Figure A.2: Average Normalized Free Contraction Error

Table A.2: Free Contraction Percent Error

V_B/V	0.75		0.695		0.64		0.58		0.438	
Model:E_1 & E_i	i=3	i=4	i=3	i=4	i=3	i=4	i=3	i=4	i=3	i=4
69 kPa	47.66	41.87	86.90	71.95	11.86	13.50	27.56	29.46	1.87	4.73
138 kPa	9.76	12.29	6.39	8.14	2.88	2.88	6.52	5.57	2.63	5.26
206 kPa	4.81	2.34	6.23	4.97	3.68	2.21	3.78	2.08	1.05	2.36
276 kPa	4.74	1.80	3.43	0.90	2.34	0.84	2.49	0.98	3.41	2.85
345 kPa	3.72	1.09	3.04	0.71	1.80	0.61	1.98	0.59	2.51	2.16
414 kPa	3.36	1.13	2.92	0.94	1.03	0.09	1.33	0.39	1.66	1.49
483 kPa	3.59	1.65	3.37	1.47	0.69	0.04	0.23	0.50	1.98	1.98
552 kPa	4.49	2.81	3.71	2.28	0.25	0.29	0.86	0.50	0.59	0.76
621 kPa	5.90	4.65	4.59	3.37	0.05	0.30	2.39	2.03	0.88	0.72
Average	9.78	7.73	13.40	10.53	2.73	2.31	5.24	4.68	1.84	2.48

Table A.3: Force Percent Error at 25% Free Contraction

V_B/V	0.75		0.695		0.64		0.58		0.438	
Model: E_1&E_i	i=3	i=4	i=3	i=4	i=3	i=4	i=3	i=4	i=3	i=4
69 kPa	2.91	3.34	6.62	8.80	25.78	22.97	34.39	32.26	4.01	6.46
138 kPa	2.04	0.05	1.60	0.92	0.83	2.14	1.57	2.44	2.03	0.52
206 kPa	1.75	2.63	0.16	1.45	1.22	1.97	3.86	4.30	2.27	1.52
276 kPa	1.19	1.88	1.21	1.97	1.00	1.56	4.50	4.81	2.88	3.36
345 kPa	0.19	0.77	0.87	1.52	0.48	0.97	1.29	1.00	4.02	4.43
414 kPa	0.08	0.47	0.28	0.87	2.50	2.96	0.26	0.00	1.39	1.79
483 kPa	0.32	0.20	0.11	0.45	0.23	0.22	3.00	3.24	0.39	0.79
552 kPa	1.07	0.52	0.96	0.40	0.57	0.12	0.06	0.31	0.36	0.04
621 kPa	4.09	3.49	1.60	1.03	1.08	0.64	0.49	0.21	4.28	3.86
Average	1.52	1.49	1.49	1.93	3.74	3.73	5.49	5.40	2.40	2.53

Table A.4: Force Percent Error at 50% Free Contraction

V_B/V	0.75		0.695		0.64		0.58		0.438	
Model: E_1&E_i	i=3	i=4	i=3	i=4	i=3	i=4	i=3	i=4	i=3	i=4
69 kPa	24.34	19.99	19.82	12.88	19.93	15.23	51.50	46.80	5.56	8.59
138 kPa	0.47	0.54	0.05	1.00	4.24	3.19	3.01	1.88	14.54	14.91
206 kPa	2.46	0.18	0.65	1.39	1.42	0.32	3.91	2.83	10.91	11.87
276 kPa	1.73	0.26	2.09	0.22	0.35	0.66	4.33	3.41	0.25	0.49
345 kPa	1.41	0.41	1.78	0.12	0.48	1.42	2.41	3.29	4.40	4.03
414 kPa	1.31	0.45	1.07	0.45	1.88	0.98	1.20	2.05	0.02	0.14
483 kPa	1.21	0.55	0.79	0.67	1.37	2.32	2.40	1.57	1.91	1.94
552 kPa	0.57	1.20	0.40	1.82	1.81	2.78	1.01	1.87	2.37	2.25
621 kPa	3.63	5.45	1.30	2.70	2.33	3.33	2.19	3.05	7.35	7.13
Average	4.12	3.23	3.11	2.36	3.76	3.36	8.00	7.42	5.26	5.70

Table A.5: Force Percent Error at 75% Free Contraction

V_B/V	0.75		0.695		0.64		0.58		0.438	
Model:E_1&E_i	i=3	i=4	i=3	i=4	i=3	i=4	i=3	i=4	i=3	i=4
69 kPa	77.92	66.09	74.13	56.82	17.32	13.70	87.45	81.66	2.29	2.91
138 kPa	1.42	9.66	2.45	11.19	4.18	0.06	0.73	4.03	51.11	60.37
206 kPa	1.45	1.88	2.07	6.85	0.47	1.87	1.87	1.09	22.06	27.28
276 kPa	1.54	0.08	3.31	1.73	0.33	0.90	4.64	4.55	1.38	1.71
345 kPa	2.61	1.94	3.52	2.66	0.33	0.24	2.14	2.29	9.15	7.58
414 kPa	4.13	3.28	3.79	3.06	4.06	3.32	0.78	0.34	4.04	3.11
483 kPa	5.07	3.77	3.31	2.36	1.00	0.05	6.05	5.37	0.13	0.45
552 kPa	4.10	2.28	2.40	1.05	1.12	0.20	2.26	1.17	0.39	0.58
621 kPa	3.85	6.35	0.41	1.25	0.47	1.16	0.24	1.67	8.63	8.60
Average	11.34	10.59	10.60	9.66	3.25	2.39	11.80	11.35	11.02	12.51

Bibliography

[1] G.S. Chirikjian and J.W. Burdick. The kinematics of hyper-redundant robot locomotion. *IEEE Transactions on Robotics and Automation*, 11(6):781–793, 1995.

[2] Victor C. Anderson. *Tensor arm manipulator design*. ASME, New York, N.Y., 1967.

[3] Michael E. Moran. Evolution of robotic arms. *Journal of Robotic Surgery*, 1(2):103–111, jun 2007.

[4] Ove Larson and Charles Davidson. Flexible arm, particularly a robot arm, jul 1983.

[5] A. Morecki, K. Jaworek, W. Pogorzelski, T. Zielinska, J. Fraczek, and G. Malczyk. Robotics System-Elephant Trunk Type Elastic Manipulator Combined with a Quadruped Walking Machine. In *Robotics and Factories of the Future '87*, pages 649–656. Springer Berlin Heidelberg, Berlin, Heidelberg, 1988.

[6] S. Hirose and S. Ma. Coupled tendon-driven multijoint manipulator. In *Proceedings. 1991 IEEE International Conference on Robotics and Automation*, pages 1268–1275. IEEE Comput. Soc. Press, 1991.

[7] P. Dario, M.C. Carrozza, M. Marcacci, S. D'Attanasio, B. Magnami, O. Tonet, and G. Megali. A novel mechatronic tool for computer-assisted arthroscopy. *IEEE Transactions on Information Technology in Biomedicine*, 4(1):15–29, mar 2000.

[8] J. F. Wilson, D. Li, Z. Chen, and R. T. George. Flexible Robot Manipulators and Grippers: Relatives of Elephant Trunks and Squid Tentacles. In *Robots and Biological Systems: Towards a New Bionics?*, pages 475–494. Springer Berlin Heidelberg, Berlin, Heidelberg, 1993.

[9] G. Robinson and J.B.C. Davies. Continuum robots - a state of the art. In *Proceedings 1999 IEEE International Conference on Robotics and Automation (Cat. No.99CH36288C)*, volume 4, pages 2849–2854. IEEE, 1999.

[10] K. Suzumori, S. Iikura, and H. Tanaka. Applying a flexible microactuator to robotic mechanisms. *IEEE Control Systems*, 12(1):21–27, feb 1992.

[11] G. Immega and K. Antonelli. The KSI tentacle manipulator. In *Proceedings of 1995 IEEE International Conference on Robotics and Automation*, volume 3, pages 3149–3154. IEEE, 1995.

[12] R. J. Webster and B. A. Jones. Design and Kinematic Modeling of Constant Curvature Continuum Robots: A Review. *The International Journal of Robotics Research*, 29(13):1661–1683, nov 2010.

[13] Ian D. Walker. Continuous Backbone "Continuum" Robot Manipulators. *ISRN Robotics*, 2013:1–19, jul 2013.

[14] K. Ikuta, M. Tsukamoto, and S. Hirose. Shape memory alloy servo actuator system with electric resistance feedback and application for active endoscope. In *Proceedings. 1988 IEEE International Conference on Robotics and Automation*, pages 427–430. IEEE Comput. Soc. Press, 1988.

[15] Y. Nakamura, A. Matsui, T. Saito, and K. Yoshimoto. Shape-memory-alloy active forceps for laparoscopic surgery. In *Proceedings of 1995 IEEE International Conference on Robotics and Automation*, volume 3, pages 2320–2327. IEEE, 1995.

[16] S.J. Phee, W.S. Ng, I.M. Chen, F. Seow-Choen, and B.L. Davies. Locomotion and steering aspects in automation of colonoscopy. I. A literature review. *IEEE Engineering in Medicine and Biology Magazine*, 16(6):85–96, 1997.

[17] J. Peirs, D. Reynaerts, H. Van Brussel, G. De Gersem, and Hsiao-Wei Tang. Design of an advanced tool guiding system for robotic surgery. In *2003 IEEE International Conference on Robotics and Automation (Cat. No.03CH37422)*, pages 2651–2656. IEEE, 2003.

[18] A. Degani, H. Choset, A. Wolf, T. Ota, and M.A. Zenati. Percutaneous Intrapericardial Interventions Using a Highly Articulated Robotic Probe. In *The First IEEE/RAS-EMBS International Conference on Biomedical Robotics and Biomechatronics, 2006. BioRob 2006.*, pages 7–12. IEEE, 2006.

[19] Takeyoshi Ota, Amir Degani, David Schwartzman, Brett Zubiate, Jeremy McGarvey, Howie Choset, and Marco A Zenati. A Highly Articulated Robotic Surgical System for Minimally Invasive Surgery. *The Annals of Thoracic Surgery*, 87(4):1253–1256, apr 2009.

[20] Kanako Harada, Zhang Bo, Shin Enosawa, Toshio Chiba, and Masakatsu G. Fujie. Bending Laser Manipulator for Intrauterine Surgery and Viscoelastic Model of Fetal Rat Tissue. In *Proceedings 2007 IEEE International Conference on Robotics and Automation*, pages 611–616. IEEE, apr 2007.

[21] R. Ohta. Results of R&D on catheter-type micromachine. In *MHS2001. Proceedings of 2001 International Symposium on Micromechatronics and Human Science (Cat. No.01TH8583)*, pages 5–12. IEEE, 2001.

[22] D.B. Camarillo, C.F. Milne, C.R. Carlson, M.R. Zinn, and J.K. Salisbury. Mechanics Modeling of Tendon-Driven Continuum Manipulators. *IEEE Transactions on Robotics*, 24(6):1262–1273, dec 2008.

[23] Carmel Majidi. Soft Robotics: A Perspective—Current Trends and Prospects for the Future. *Soft Robotics*, 1(1):5–11, mar 2014.

[24] Michael T. Tolley, Robert F. Shepherd, Michael Karpelson, Nicholas W. Bartlett, Kevin C. Galloway, Michael Wehner, Rui Nunes, George M. Whitesides, and Robert J. Wood. An untethered jumping soft robot. In *2014 IEEE/RSJ International Conference on Intelligent Robots and Systems*, pages 561–566. IEEE, sep 2014.

[25] Nicholas W. Bartlett, Michael T. Tolley, Johannes T. .B Overvelde, James C. Weaver, Bobak Mosadegh, Katia Bertoldi, George M. Whitesides, and Robert J. Wood. SOFT ROBOTICS. A 3D-printed, functionally graded soft robot powered by combustion. *Science (New York, N.Y.)*, 349(6244):161–5, jul 2015.

[26] Adam A. Stokes, Robert F. Shepherd, Stephen A. Morin, Filip Ilievski, and George M. Whitesides. A Hybrid Combining Hard and Soft Robots. *Soft Robotics*, 1(1):70–74, mar 2014.

[27] Koichi Suzumori, Akira Wada, and Shuichi Wakimoto. New mobile pressure control system for pneumatic actuators, using reversible chemical reactions of water. *Sensors and Actuators A: Physical*, 201:148–153, oct 2013.

[28] Michael Wehner, Michael T. Tolley, Yiğit Mengüç, Yong-Lae Park, Annan Mozeika, Ye Ding, Cagdas Onal, Robert F. Shepherd, George M. Whitesides, and Robert J. Wood. Pneumatic Energy Sources for Autonomous and Wearable Soft Robotics. *Soft Robotics*, oct 2014.

[29] W. McMahan, V. Chitrakaran, M. Csencsits, D. Dawson, I.D. Walker, B.A. Jones, M. Pritts, D. Dienno, M. Grissom, and C.D. Rahn. Field trials and testing of the OctArm continuum manipulator. In *Proceedings 2006 IEEE International Conference on Robotics and Automation, 2006. ICRA 2006.*, pages 2336–2341. IEEE, 2006.

[30] Shixin Mao, Erbao Dong, Hu Jin, Min Xu, Shiwu Zhang, Jie Yang, and Kin Huat Low. Gait Study and Pattern Generation of a Starfish-Like Soft Robot with Flexible Rays Actuated by SMAs. *Journal of Bionic Engineering*, 11(3):400–411, jul 2014.

[31] F. Renda, M. Cianchetti, M. Giorelli, A. Arienti, and C. Laschi. A 3D steady-state model of a tendon-driven continuum soft manipulator inspired by the octopus arm. *Bioinspiration & biomimetics*, 7(2):025006, jun 2012.

[32] Deepak Trivedi, Christopher D. Rahn, William M. Kier, and Ian D. Walker. Soft robotics: Biological inspiration, state of the art, and future research. *Applied Bionics and Biomechanics*, 5(3):99–117, dec 2008.

[33] S. Wakimoto, K. Ogura, K. Suzumori, and Y. Nishioka. Miniature soft hand with curling rubber pneumatic actuators. In *2009 IEEE International Conference on Robotics and Automation*, pages 556–561. IEEE, may 2009.

[34] C. Laschi, B. Mazzolai, V. Mattoli, M. Cianchetti, and P. Dario. Design of a biomimetic robotic octopus arm. *Bioinspiration & Biomimetics*, 4(1):015006, mar 2009.

[35] Farahnaz Maghooa, Agostino Stilli, Yohan Noh, Kaspar Althoefer, and Helge A Wurdemann. Tendon and pressure actuation for a bio-inspired manipulator based on an antagonistic principle. In *2015 IEEE International Conference on Robotics and Automation (ICRA)*, pages 2556–2561. IEEE, may 2015.

[36] B.A. Jones and I.D. Walker. Kinematics for multisection continuum robots. *IEEE Transactions on Robotics*, 22(1):43–55, feb 2006.

[37] P. Arena, C. Bonomo, L. Fortuna, M. Frasca, and S. Graziani. Design and Control of an IPMC Wormlike Robot. *IEEE Transactions on Systems, Man and Cybernetics, Part B (Cybernetics)*, 36(5):1044–1052, oct 2006.

[38] Sangok Seok, Cagdas Denizel Onal, Kyu-Jin Cho, Robert J Wood, Daniela Rus, and Sangbae Kim. Meshworm: A Peristaltic Soft Robot With Antagonistic Nickel Titanium Coil Actuators. *IEEE/ASME Transaction on Mechatronics*, 18(5):1485–1497, 2013.

[39] Hyunwoo Yuk, Daeyeon Kim, Honggu Lee, Sungho Jo, and Jennifer H Shin. Shape memory alloy-based small crawling robots inspired by *C. elegans*. *Bioinspiration & Biomimetics*, 6(4):046002, dec 2011.

[40] T. Umedachi, V. Vikas, and B. A. Trimmer. Softworms : the design and control of non-pneumatic, 3D-printed, deformable robots. *Bioinspiration & Biomimetics*, 11(2):025001, mar 2016.

[41] Kevin C. Galloway, Panagiotis Polygerinos, Conor J. Walsh, and Robert J. Wood. Mechanically programmable bend radius for fiber-reinforced soft actuators. In *2013 16th International Conference on Advanced Robotics, ICAR 2013*, 2013.

[42] Raphael Deimel and Oliver Brock. A Novel Type of Compliant , Underactuated Robotic Hand for Dexterous Grasping. *Proceedings of Robotics: Science and Systems*, 2014.

[43] Kevin C Galloway, Kaitlyn P Becker, Brennan Phillips, Jordan Kirby, Stephen Licht, Dan Tchernov, Robert J Wood, and David F Gruber. Soft Robotic

Grippers for Biological Sampling on Deep Reefs. *Soft robotics*, 3(1):23–33, mar 2016.

[44] Bobak Mosadegh, Panagiotis Polygerinos, Christoph Keplinger, Sophia Wennstedt, Robert F. Shepherd, Unmukt Gupta, Jongmin Shim, Katia Bertoldi, Conor J. Walsh, and George M. Whitesides. Pneumatic Networks for Soft Robotics that Actuate Rapidly. *Advanced Functional Materials*, 24(15):2163–2170, apr 2014.

[45] Ian D. Walker, Darren M. Dawson, Tamar Flash, Frank W. Grasso, Roger T. Hanlon, Binyamin Hochner, William M. Kier, Christopher C. Pagano, Christopher D. Rahn, and Qiming M. Zhang. Continuum robot arms inspired by cephalopods. In Grant R. Gerhart, Charles M. Shoemaker, and Douglas W. Gage, editors, *Proceedings Volume 5804, Unmanned Ground Vehicle Technology VII*, volume 5804, page 303. International Society for Optics and Photonics, may 2005.

[46] Deepak Trivedi, Dustin Dienno, and Christopher D. Rahn. Optimal, Model-Based Design of Soft Robotic Manipulators. *Journal of Mechanical Design*, 130(9):091402, sep 2008.

[47] N. Giri and I. Walker. Continuum robots and underactuated grasping. *Mechanical Sciences*, 2(1):51–58, feb 2011.

[48] Alan Bartow, Apoorva Kapadia, and Ian D. Walker. A novel continuum trunk robot based on contractor muscles. In Agoujil Said, Collin Howe Hing Tang, and Sorinel Oprisan, editors, *Recent advances in circuits, communication& signal processing*, pages 181–186. WSEAS World Scientific Engineering Academy and Society, Cambridge, 2013.

[49] Rongjie Kang, David T Branson, Tianjiang Zheng, Emanuele Guglielmino, and Darwin G Caldwell. Design, modeling and control of a pneumatically actuated manipulator inspired by biological continuum structures. *Bioinspiration & biomimetics*, 8(3):036008, sep 2013.

[50] Bong-Soo Kang and Edward J. Park. Modeling and control of an intrinsic continuum robot actuated by pneumatic artificial muscles. In *2016 IEEE International Conference on Advanced Intelligent Mechatronics (AIM)*, pages 1157–1162. IEEE, jul 2016.

[51] Ryeong-Hyeon Kim, Chang-Hyeon Kang, Ji-Hwan Bae, and Bong-Soo Kang. Development of a continuum robot using pneumatic artificial muscles. In *2014 14th International Conference on Control, Automation and Systems (ICCAS 2014)*, pages 1401–1403. IEEE, oct 2014.

[52] Daniela Rus and Michael T. Tolley. Design, fabrication and control of soft robots. *Nature*, 521(7553):467–475, may 2015.

[53] Liyu Wang and Fumiya Iida. Deformation in Soft-Matter Robotics: A Categorization and Quantitative Characterization. *IEEE Robotics and Automation Magazine*, 22(3), 2015.

[54] Gregory S. Chirikjian. Hyper-redundant manipulator dynamics: a continuum approximation. *Advanced Robotics*, 9(3):217–243, jan 1994.

[55] I.A. Gravagne, C.D. Rahn, and I.D. Walker. Large deflection dynamics and control for planar continuum robots. *IEEE/ASME Transactions on Mechatronics*, 8(2):299–307, jun 2003.

[56] D. Trivedi, A. Lotfi, and C.D. Rahn. Geometrically Exact Models for Soft Robotic Manipulators. *IEEE Transactions on Robotics*, 24(4):773–780, aug 2008.

[57] Deepak Trivedi and Christopher D. Rahn. Soft Robotic Manipulators: Design, Analysis, and Control. In Norman M. Wereley and J.M. Sater, editors, *Plants and Mechanical Motion: A Synthetic Approach to Nastic Materials and Structures*, chapter Soft Robot, pages 141–165. DEStech Publications, Inc., Lancaster, PA, 2012.

[58] Federico Renda, Michele Giorelli, Marcello Calisti, Matteo Cianchetti, and Cecilia Laschi. Dynamic Model of a Multibending Soft Robot Arm Driven by Cables. *IEEE Transactions on Robotics*, 30(5):1109–1122, oct 2014.

[59] Mohsen Mahvash and Pierre E Dupont. Stiffness Control of Surgical Continuum Manipulators. *IEEE transactions on robotics : a publication of the IEEE Robotics and Automation Society*, 27(2):334–345, apr 2011.

[60] Mohammad Dehghani and S. Ali A. Moosavian. Modeling and control of a planar continuum robot. In *2011 IEEE/ASME International Conference on Advanced Intelligent Mechatronics (AIM)*, pages 966–971. IEEE, jul 2011.

[61] M. Giorelli, F. Renda, M. Calisti, A. Arienti, G. Ferri, and C. Laschi. Learning the inverse kinetics of an octopus-like manipulator in three-dimensional space. *Bioinspiration & biomimetics*, 10(3):035006, jun 2015.

[62] Kristin M. de Payrebrune and Oliver M. O'Reilly. On constitutive relations for a rod-based model of a pneu-net bending actuator. *Extreme Mechanics Letters*, 8:38–46, sep 2016.

[63] Robert J. Webster, Jin Seob Kim, Noah J. Cowan, Gregory S. Chirikjian, and Allison M. Okamura. Nonholonomic Modeling of Needle Steering. *The International Journal of Robotics Research*, 25(5-6):509–525, may 2006.

[64] Bryan A. Jones and Ian D. Walker. Practical Kinematics for Real-Time Implementation of Continuum Robots. *IEEE Transactions on Robotics*, 22(6):1087–1099, dec 2006.

[65] Enver Tatlicioglu, Ian D. Walker, and Darren M. Dawson. New dynamic models for planar extensible continuum robot manipulators. In *IEEE International Conference on Intelligent Robots and Systems*, 2007.

[66] Isuru S. Godage, David T. Branson, Emanuele Guglielmino, and Darwin G. Caldwell. Pneumatic muscle actuated continuum arms: Modelling and experimental assessment. In *2012 IEEE International Conference on Robotics and Automation*, pages 4980–4985. IEEE, may 2012.

[67] Isuru S. Godage, Raul Wirz, Ian D. Walker, and Robert J. Webster. Accurate and Efficient Dynamics for Variable-Length Continuum Arms: A Center of Gravity Approach. *Soft Robotics*, 2(3):96–106, sep 2015.

[68] Matthias Rolf and Jochen J. Steil. Constant curvature continuum kinematics as fast approximate model for the Bionic Handling Assistant. In *2012 IEEE/RSJ International Conference on Intelligent Robots and Systems*, pages 3440–3446. IEEE, oct 2012.

[69] Tobias Mahl, Alexander Hildebrandt, and Oliver Sawodny. A Variable Curvature Continuum Kinematics for Kinematic Control of the Bionic Handling Assistant. *IEEE Transactions on Robotics*, 30(4):935–949, aug 2014.

[70] Bin He, Zhipeng Wang, Qiang Li, Hong Xie, and Runjie Shen. An Analytic Method for the Kinematics and Dynamics of a Multiple-Backbone Continuum Robot Regular Paper. *International Journal of Advanced Robotic Systems*, 2012.

[71] Manas M. Tonapi, Isuru S. Godage, and Ian D. Walker. Design, modeling and performance evaluation of a long and slim continuum robotic cable. In *2014 IEEE/RSJ International Conference on Intelligent Robots and Systems*, pages 2852–2859. IEEE, sep 2014.

[72] William S. Rone and Pinhas Ben-Tzvi. Continuum Robot Dynamics Utilizing the Principle of Virtual Power. *IEEE Transactions on Robotics*, 30(1):275–287, feb 2014.

[73] William S. Rone and Pinhas Ben-Tzvi. Multi-segment continuum robot shape estimation using passive cable displacement. In *2013 IEEE International Symposium on Robotic and Sensors Environments (ROSE)*, pages 37–42. IEEE, oct 2013.

[74] Andrew D. Marchese, Konrad Komorowski, Cagdas D. Onal, and Daniela Rus. Design and control of a soft and continuously deformable 2D robotic manipulation system. In *Proceedings - IEEE International Conference on Robotics and Automation*, 2014.

[75] Yoram Yekutieli, Roni Sagiv-Zohar, Ranit Aharonov, Yaakov Engel, Binyamin Hochner, and Tamar Flash. Dynamic model of the octopus arm. I. Biomechanics

of the octopus reaching movement. *Journal of neurophysiology*, 94(2):1443–58, aug 2005.

[76] Achille Melingui, Othman Lakhal, Boubaker Daachi, Jean Bosco Mbede, and Rochdi Merzouki. Adaptive Neural Network Control of a Compact Bionic Handling Arm. *IEEE/ASME Transactions on Mechatronics*, PP(99):1–14, 2015.

[77] J. F. Queisser, K. Neumann, M. Rolf, R. F. Reinhart, and J. J. Steil. An active compliant control mode for interaction with a pneumatic soft robot. In *2014 IEEE/RSJ International Conference on Intelligent Robots and Systems*, pages 573–579. IEEE, sep 2014.

[78] Vishesh Vikas, Piyush Grover, and Barry Trimmer. Model-free control framework for multi-limb soft robots. In *IEEE International Conference on Intelligent Robots and Systems*, volume 2015-Decem, pages 1111–1116. Institute of Electrical and Electronics Engineers Inc., 2015.

[79] Ying Zhang, Chaoqun Xiang, Hui Yang, Yongqiang Li, and Lina Hao. Static analysis of novel continuum robot driven by PAMs. In *2016 13th International Conference on Ubiquitous Robots and Ambient Intelligence (URAI)*, pages 96–100. IEEE, aug 2016.

[80] Richard Gaylord. Fluid actuated motor system and stroking device, jan 1958.

[81] Joshua Bishop-Moer, Charles Kim, Girish Krishnan, and Sridhar Kota. Kinematic Synthesis of Fiber Reinforced Soft Actuators in Parallel Combinations.pdf. In *International Design Engineering Technical Conferences & Computes and Infromation in Engeering Conference*, Chicago, IL, 2012.

[82] B K S Woods, Michael F Gentry, Curt S Kothera, and Norman M Wereley. Fatigue life testing of swaged pneumatic artificial muscles for aerospace morphing applications. *Journal of Intelligent Material Systems and Structures*, 23(3):327–343, 2012.

[83] M. A. Meller, M. Bryant, and E. Garcia. Reconsidering the McKibben muscle: Energetics, operating fluid, and bladder material. *Journal of Intelligent Material Systems and Structures*, 25(18):2276–2293, sep 2014.

[84] Hal Schulte. The application of external power in prosthetics and orthotics. Technical report, National Academy of Sciences, Washington, D.C., 1961.

[85] C. Chou and B. Hannaford. Measurement and modeling of McKibben pneumatic artificial muscles. *IEEE Transactions on Robotics and Automation*, 12(1):90–102, 1996.

[86] Glenn K. Klute and Blake Hannaford. Accounting for Elastic Energy Storage in McKibben Artificial Muscle Actuators. *Journal of Dynamic Systems, Measurement, and Control*, 122(2):386, jun 2000.

[87] Curt S. Kothera, Mamta Jangid, Jayant Sirohi, and Norman M. Wereley. Experimental characterization and static modeling of McKibben actuators. *Journal of Mechanical Design*, 131(9):091010, sep 2009.

[88] Carlo Ferraresi, Walter Franco, and Andrea Manuello Bertetto. Flexible pneumatic actuators: A comparison between the McKibben and the straight fibres muscles. *Journal of Robotics and Mechatronics*, 13(1):56–63, 2001.

[89] Erica G. Hocking and Norman M. Wereley. Analysis of nonlinear elastic behavior in miniature pneumatic artificial muscles. *Smart Materials and Structures*, 22(1):014016, jan 2013.

[90] R. M. Robinson, C. S. Kothera, and N. M. Wereley. Quasi-static nonlinear response of pneumatic artificial muscles for both agonistic and antagonistic actuation modes. *Journal of Intelligent Material Systems and Structures*, 26(7):796–809, may 2014.

[91] B. Tondu. Modelling of the McKibben artificial muscle: A review. *Journal of Intelligent Material Systems and Structures*, 23(3):225–253, mar 2012.

[92] Marc D. Doumit and Scott Pardoel. Dynamic contraction behaviour of pneumatic artificial muscle. *Mechanical Systems and Signal Processing*, 91:93–110, jul 2017.

[93] W. Liu and C. R. Rahn. Fiber-Reinforced Membrane Models of McKibben Actuators. *Journal of Applied Mechanics*, 70(6):853, nov 2003.

[94] M. De Volder, A.J.M. Moers, and D. Reynaerts. Fabrication and control of miniature McKibben actuators. *Sensors and Actuators A: Physical*, 166(1):111–116, mar 2011.

[95] B. Solano and C. Rotinat-Libersa. Compact and lightweight hydraulic actuation system for high performance millimeter scale robotic applications: Modeling and experiments. *Journal of Intelligent Material Systems and Structures*, 22(13):1479–1487, sep 2011.

[96] Shanthanu Chakravarthy, K. Aditya, and Ashitava Ghosal. Experimental Characterization and Control of Miniaturized Pneumatic Artificial Muscle. *Journal of Medical Devices*, 8(4):041011, oct 2014.

[97] Aniruddh Vashisth, Bin Zhu, Benjamin M Wimmer, Charles E Bakis, and Christopher D Rahn. Evaluation of millimeter-size fluidic flexible matrix composite tubes. In *ASME 2013 Conference on Smart Materials, Adaptive Structures and Intelligent Systems*, volume 2, pages 1–9, Snowbird, UT, 2013.

[98] L. Mullins. Softening of Rubber by Deformation. *Rubber Chemistry and Technology*, 42(1):339–362, mar 1969.

[99] B. Hannaford, J. M. Winters, C. P. Chou, and P. H. Marbot. The anthroform biorobotic arm: a system for the study of spinal circuits. *Annals of Biomedical Engineering*, 23(4):399–408, 1995.

[100] I. Boblan, R. Bannasch, H. Schwenk, F. Prietzel, L. Miertsch, and A. Schulz. A human-like robot hand and arm with fluidic muscles: Biologically inspired construction and functionality. In *Embodied Artificial Intelligence*, pages 160–179. Springer, 2003.

[101] B. Tondu, S. Ippolito, J. Guiochet, and A. Daidie. A seven-degrees-of-freedom robot-arm driven by pneumatic artificial muscles for humanoid robots. *The International Journal of Robotics Research*, 24(4):257–274, 2005.

[102] Ryan M. Robinson, Curt S. Kothera, Robert M. Sanner, and Norman M. Wereley. Nonlinear Control of Robotic Manipulators Driven by Pneumatic Artificial Muscles. *IEEE/ASME Transactions on Mechatronics*, 21(1):55–68, feb 2016.

[103] J. Vermeulen. Trajectory planning for the walking biped 'Lucy'. *The International Journal of Robotics Research*, 25(9):867–887, 2006.

[104] R.W. Colbrunn, G.M. Nelson, and R.D. Quinn. Design and control of a robotic leg with braided pneumatic actuators. In *Proceedings 2001 IEEE/RSJ International Conference on Intelligent Robots and Systems. Expanding the Societal Role of Robotics in the the Next Millennium (Cat. No.01CH37180)*, volume 2, pages 992–998. IEEE, 2001.

[105] Y.K. Lee and I. Shimoyama. A skeletal framework artificial hand actuated by pneumatic artificial muscles. In *Proceedings 1999 IEEE International Conference on Robotics and Automation (Cat. No.99CH36288C)*, volume 2, pages 926–931. IEEE, 1999.

[106] F. Rothling, R. Haschke, J. J. Steil, and H. Ritter. Platform portable anthropomorphic grasping with the Bielefeld 20-DOF Shadow and 9-DOF TUM hand. In *2007 IEEE/RSJ International Conference on Intelligent Robots and Systems*, pages 2951–2956. IEEE, 2007.

[107] Benjamin K. S. Woods, Shane M. Boyer, Erica G. Hocking, Norman M. Wereley, and Curt S. Kothera. Contractile Pneumatic Artificial Muscle Configured to Generate Extension. *Journal of Dynamic Systems, Measurement, and Control*, 136(3):034501, jan 2014.

[108] R. D. Vocke, C. S. Kothera, A. Chaudhuri, B. K. S. Woods, and N. M. Wereley. Design and testing of a high-specific work actuator using miniature pneumatic artificial muscles. *Journal of Intelligent Material Systems and Structures*, 23(3):365–378, jan 2012.

[109] Yong-Lae Park, Bor-rong Chen, Néstor O Pérez-Arancibia, Diana Young, Leia Stirling, Robert J Wood, Eugene C Goldfield, and Radhika Nagpal. Design and control of a bio-inspired soft wearable robotic device for ankle-foot rehabilitation. *Bioinspiration & biomimetics*, 9(1):016007, mar 2014.

[110] Kotaro Tadano, Masao Akai, Kazuo Kadota, and Kenji Kawashima. Development of grip amplified glove using bi-articular mechanism with pneumatic artificial rubber muscle. In *2010 IEEE International Conference on Robotics and Automation*, pages 2363–2368. IEEE, may 2010.

[111] B. K. S. Woods, C. S. Kothera, and N. M. Wereley. Wind tunnel testing of a helicopter rotor trailing edge flap actuated via pneumatic artificial muscles. *Journal of Intelligent Material Systems and Structures*, 22(13):1513–1528, 2011.

[112] Daewon Kim, Ryan Capps, and Michael K. Philen. Morphing Trailing Edge Control Using Flexible Matrix Composite Actuators (AIAA). In *53rd AIAA/ASME/ASCE/AHS/ASC Structures, Structural Dynamics and Materials Conference*, Honolulu, 2012.

[113] E. B. Doepke, Michael K. Philen, and Robert L. West. Design and optimization of a morphing aileron control surface using FMC actuators. In *SPIE Smart Structures and Materials + Nondestructive Evaluation and Health Monitoring*, page 90613H. International Society for Optics and Photonics, apr 2014.

[114] Yijin Chen, Weilong Yin, Yanju Liu, and Jinsong Leng. Structural design and analysis of morphing skin embedded with pneumatic muscle fibers. *Smart Materials and Structures*, 20(8):085033, aug 2011.

[115] B. Zhu, C. D. Rahn, and C. E. Bakis. Actuation of fluidic flexible matrix composites in structural media. *Journal of Intelligent Material Systems and Structures*, 23(3):269–278, nov 2011.

[116] R. M. Robinson, C. S. Kothera, B. K. S. Woods, R. D. Vocke III, and N. M. Wereley. High specific power actuators for robotic manipulators. *Journal of Intelligent Material Systems and Structures*, 22(13):1501–1511, 2011.

[117] Emanuel Azizi and Thomas J Roberts. Variable gearing in a biologically inspired pneumatic actuator array. *Bioinspiration & Biomimetics*, 8(2):026002, June 2013.

[118] G. Wang, N. M. Wereley, and T. Pillsbury. Non-linear quasi-static model of pneumatic artificial muscle actuators. *Journal of Intelligent Material Systems and Structures*, 26(5):541–553, May 2014.

[119] D.G. Caldwell, G.a. Medrano-Cerda, and M. Goodwin. Control of pneumatic muscle actuators. *IEEE Control Systems Magazine*, 15(1):40–48, 1995.

[120] Ryan M. Robinson, Curt S. Kothera, and Norman M. Wereley. Control of a heavy-lift robotic manipulator with pneumatic artificial muscles. *Actuators*, 3(2):41–65, 2014.

[121] M.C. Birch, R.D. Quinn, G. Hahm, S.M. Phillips, B. Drennan, R.D. Beer, S.L. Garverick, S. Laksanacharoen, A.J. Pollack, and R.E. Ritzmann. A miniature hybrid robot propelled by legs. In *Proc. 2001 IEEE/RSJ Int. Conf. Intell. Robot. Syst. Expand. Soc. Role Robot. Next Millenn. (Cat. No.01CH37180)*, volume 2, pages 845–851. IEEE, 2001.

[122] R. Tiwari, M. A. Meller, K. B. Wajcs, C. Moses, I. Reveles, and E. Garcia. Hydraulic artificial muscles. *Journal of Intelligent Material Systems and Structures*, 23(3):301–312, mar 2012.

[123] Erick Ball, Yong Lin, and Ephrahim Garcia. Characterization and modeling of geometric variations in McKibben pneumatic artificial muscles. In *SPIE Smart Structures and Materials + Nondestructive Evaluation and Health Monitoring*, page 868605. International Society for Optics and Photonics, apr 2013.

[124] Freeman Manufacturing and Supply Company. Bluestar® Silicone Rubber Specifications.

[125] R. W. Colbrunn. *Design and control of a robotic leg with braided pneumatic actuators*. PhD thesis, Case Western Reserve University, 2000.

[126] M.K. Philen, Y. Shan, P. Prakash, K.W. Wang, C.D. Rahn, A.L. Zydney, and C.E. Bakis. Fibrillar Network Adaptive Structure with Ion-transport Actuation. *Journal of Intelligent Material Systems and Structures*, 18(4):323–334, dec 2006.

[127] Thomas E. Pillsbury, Curt S. Kothera, and Norman M. Wereley. Effect of bladder wall thickness on miniature pneumatic artificial muscle performance. *Bioinspiration and Biomimetics*, 10(5):055006, 2015.

[128] Carlo Ferraresi, Walter Franco, and Andrea Manuello Bertetto. Flexible pneumatic actuators: a comparison between the McKibben and the straight fibres muscles. *Journal of Robotics and Mechatronics*, 13(1), 2001.

[129] Frank Daerden and Dirk Lefeber. Pneumatic artificial muscles: actuators for robotics and automation. *European journal of Mechanical and Environmental Engineering*, 47:10–21, 2000.

[130] N. Tsagarakis and D. G. Caldwell. Improved modelling and assessment of pneumatic muscle actuators. In *Proceedings 2000 ICRA. Millennium Conference. IEEE International Conference on Robotics and Automation. Symposia Proceedings (Cat. No.00CH37065)*, volume 4, pages 3641–3646 vol.4, April 2000.

[131] M. Mooney. A Theory of Large Elastic Deformation. *Journal of Applied Physics*, 11(9):582–592, sep 1940.

[132] Ronald S. Rivlin and D.W. Saunders. Large elastic deformations of isotropic materials VII. Experiments on the deformation of rubber. *Philosophical Transactions of the Royal Society of London A: Mathematical, Physical and Engineering Sciences*, 243(865):251–288, 1951.

[133] R. W. Ogden. Large Deformation Isotropic Elasticity - On the Correlation of Theory and Experiment for Incompressible Rubberlike Solids. *Proceedings of the Royal Society of London A: Mathematical, Physical and Engineering Sciences*, 326(1567), 1972.

[134] Raymond W. Ogden. *Non-linear elastic deformations*. New York: Dover Publications, 1997.

[135] D.M. Haughton and R.W. Ogden. Bifurcation of inflated circular cylinders of elastic material under axial loading—II. Exact theory for thick-walled tubes. *Journal of the Mechanics and Physics of Solids*, 27(5-6):489–512, dec 1979.

[136] D. Trivedi, A. Lotfi, and C.D. Rahn. Geometrically Exact Models for Soft Robotic Manipulators. *IEEE Transactions on Robotics*, 24(4):773–780, August 2008.

[137] Thomas E Pillsbury, Norman M Wereley, and Qinghua Guan. Comparison of contractile and extensile pneumatic artificial muscles. *Smart Materials and Structures*, 26(9):095034, sep 2017.